Université de Montréal

Low cost synthesis of cathode and anode materials for lithium-ion batteries

par

Lifeng Cheng

Département de chimie

Faculté des arts et des sciences

Mémoire présenté à la Faculté des études supérieures et postdoctorales

en vue de l'obtention du grade de

Maitrise (M.Sc.)

en chimie

April, 2013

Résumé

Dans cette thèse, nous démontrons des travaux sur la synthèse à faible coût des matériaux de cathode et l'anode pour les piles lithium-ion.

Pour les cathodes, nous avons utilisé des précurseurs à faible coût pour préparer $LiFePO_4$ et $LiFe_{0.3}Mn_{0.7}PO_4$ en utilisant une méthode hydrothermale. Tout d'abord, des matériaux composites ($LiFePO_4/C$) ont été synthétisés à partir d'un précurseur de Fe_2O_3 par une procédé hydrothermique pour faire $LiFePO_4(OH)$ dans une première étape suivie d'une calcination rapide pour le revêtement de carbone. Deuxièmement, $LiFePO_4$ avec une bonne cristallinité et une grande pureté a été synthétisé en une seule étape, avec Fe_2O_3 par voie hydrothermale. Troisièmement, $LiFe_{0.3}Mn_{0.7}PO_4$ a été préparé en utilisant Fe_2O_3 et MnO comme des précurseurs de bas coûts au sein d'une méthode hydrothermale synthétique.

Pour les matériaux d'anode, nous avons nos efforts concentré sur un matériau d'anode à faible coût α-Fe_2O_3 avec deux types de synthèse hydrothermales, une a base de micro-ondes (MAH) l’autre plus conventionnelles (CH).

La nouveauté de cette thèse est que pour la première fois le $LiFePO_4$ a été préparé par une méthode hydrothermale en utilisant un précurseur Fe^{3+} (Fe_2O_3). Le Fe_2O_3 est un précurseur à faible coût et en combinant ses coûts avec les conditions de synthèse à basse température nous avons réalisé une réduction considérable des coûts de production pour le $LiFePO_4$, menant ainsi à une meilleure commercialisation du $LiFePO_4$ comme matériaux de cathode dans les piles lithium-ion. Par cette méthode de préparation, le $LiFePO_4/C$ procure une capacité de décharge et une stabilité de cycle accrue par rapport une synthétisation par la méthode à l'état solide pour les mêmes précurseurs Les résultats sont résumés dans deux articles qui ont été récemment soumis dans des revues scientifiques.

Mots-clés: Lithium-ion, cathode, anode, phosphate de fer lithié, oxyde ferrique, faible coût, hydrothermale.

Abstract

In this thesis, low cost syntheses of cathode and anode materials for lithium ion batteries will be presented.

For cathode materials, low cost precursors were used to prepare $LiFePO_4$ and $LiFe_{0.3}Mn_{0.7}PO_4$ using low temperature hydrothermal method. **Initially**, a $LiFePO_4/C$ composite material was synthesized from a Fe_2O_3 precursor using a hydrothermal method to prepare $LiFePO_4(OH)$ in a first step followed by a fast calcination and carbon coating. **Secondly**, $LiFePO_4$ with good crystallinity and high purity was synthesized, in one step, with nanometric sized Fe_2O_3 by a hydrothermal method. **Thirdly**, $LiFe_{0.3}Mn_{0.7}PO_4$ was prepared using low cost Fe_2O_3 and MnO as precursors within a hydrothermal synthetic method.

For anode materials, a low cost anode material α-Fe_2O_3 was prepared using two hydrothermal synthetic methods, microwave assisted (MAH) and conventional hydrothermal (CH).

The novelty of the thesis is for the first time $LiFePO_4$ has been prepared using a low cost Fe^{3+} precursor (Fe_2O_3) by a hydrothermal method. Low cost precursors and low temperature synthesis conditions will greatly reduce the synthetic cost of $LiFePO_4$, leading to greater commercialization of $LiFePO_4$ as a cathode materials for lithium-ion batteries. The as-prepared $LiFePO_4/C$ product provided enhanced discharge capacity and cycling stability compared to that synthesized using a solid state method with the same precursors. The results were summarized within two articles that were recently submitted to peer reviewed scientific journals.

Keywords: Lithium-ion batteries, cathode, anode, lithium iron phosphate, ferric oxide, low cost, hydrothermal methods.

Table of Contents

List of Tables

List of Figures

List of Abbreviations

a,b,c - Crystallographic lattice parameters

Ah - Ampere hour

BE - The binding energy of the atomic orbital from which the electron originates

CH - Conventional hydrothermal methods

CTR - A carbothermal reduction method

d - Spacing between atom layers

DEC - Diethyl carbonate

e - Electron charge

EC - Ethylene carbonate

ESCA - Electron Spectroscopy for Chemical Analysis

E_{cell} - Cell voltage

EV - Electric vehicles

F - Faraday constant

Fe_2O_3 - Ferric oxide

FESEM - Field Emission Scanning Electron Microscopy

FWHM - Full width at half maximum

ΔG - Gibbs free energy

hv - The energy of the photon

Hematite - α-Fe_2O_3

HEV - Hybrid electric vehicles

I - current

K - The shape factor

LIBs - Lithium ion batteries

Li-ion - lithium-ion

MAH - Microwave assisted methods

n - An integer

NMP - N-methylpyrroldinone

1D - one dimensional

P - The power

PVDF - Polyvinylidene difluoride

Q_T - Theoretical capacity

Q_m - The measured capacity

SEM - Scanning electron microscopy

SEI- Solid Electrolyte Interphase

Tavorite- $LiFePO_4(OH)$

V - Volt

Wh - Watt hour

wt% - Weight percent

XRD - X-ray diffraction

XPS - X-ray photoelectron spectroscopy

β - The line broadening at half the maximum intensity (FWHM) in radians

θ - The angle of incidence of the X-ray

λ - The wavelength

ϕ_s - The spectrometer work function

Acknowledgments

First and foremost, I would like to thank my supervisor, Dr. Dean MacNeil, who helped me with each step of this thesis. I feel so lucky to work with him, and learned a lot from him more than lithium ion batteries. I also would like to express my deep appriciation to Dr. Guoxian Liang, the reseach director from Clarian Inc. He gave me a lot of suggestions and ideas, helping me accomplish the experiments in this thesis.

I would also like to thank every member of Dr.MacNeil's laboratory. In particular, to Isadora Reis Rodrigues, Karen Galoustov and Benjamin Deheron,who helped me make through the hard time at the beginning of the projects. And I cannot forget the good time with Soumia El Khakani, who is such a good friend in both life and work.

I would also like to express my enormous gratitude to everybody from the administration And chemistry department of the University of Montreal. Thanks André L Beauchamp, who gave me a lot of help for my master programme, thanks my juries Dr. Dominic Rochefort and Dr. Radu Ion Iftimie who helped me improve my thesis. And thanks Thierry Maris and Laurent Mouden who helped me test my samples.

Finally, I would like to thank my family and my friends (Bin Chen, Zhongkuai Cui, Ya Deng, Na Xue, etc.). They are always my rocks in my life, and always give me love and strength. I love all of you forever.

Lifeng

Chapter 1 Introduction

1.1 General introduction

The demand for sustainable and clean energy is becoming more and more critical owing to the emergence of such applications as electric vehicles and many new types of portable electronic devices. Without energy storage, renewable electricity generation (wind, wave, solar) will be much less viable due to its intermittent nature. Therefore, the search for the next generation of energy-storage materials and devices is extremely important [1-4].

Rechargeable lithium-ion batteries (LIBs) have been considered as one of the most promising energy storage system for a wide variety of applications. They have many advantages such as long cycle life, low self-discharge, high and wide operating temperature window, and no "memory effect". LIBs have revolutionized portable electronic devices including cell phones, laptops, and digital cameras with a market valued at ~ ten billion dollars [5-10]. They are also important power sources for electric vehicles (EV), hybrid electric vehicles (HEV), and emerging smart grids [11-21].

1.2 Basics of lithium ion batteries

A battery is an electrochemical cell that converts stored chemical energy into electricity via a chemical reaction. Although the term "battery" was initially coined to refer to a stack of cells in series, it is now also used to name a single electrochemical cell. It consists of a positive and a negative electrode (both sources of chemical reactions) separated by an electrolyte solution containing dissociated salts, which enable ions transfer between the two electrodes. Once these electrodes are connected externally, the chemical reactions proceed in tandem at electrodes, thereby liberating electrons and enabling the current to be tapped by the users [17]. As the chemical reactions finish, the electron flow (current) stops. If the process can be reversed by applying an external current, batteries can be recharged. Rechargeable batteries are also termed "secondary batteries", while non-rechargeable batteries are called "primary batteries" [22].

The performance of a battery can be evaluated by numerous properties, such as its electrochemical capacity (mAh g^{-1}), cell voltage (V), energy density (Wh g^{-1}) and power density (W g^{-1}). The capacity of a battery system is the amount of electrons exchanged during the redox reactions per gram of active materials. The theoretical capacity (Q_T) of a cell can be calculated as:

$$Q_T = x(nF) \tag{1.1}$$

where x is the theoretical number of moles associated with the complete electrochemical reaction within the cell, n is the number of electrons involved in the redox reaction and F is Faraday's constant (96490 C mol^{-1}). In reality, the measured capacity (Q_m) of a cell is always lower than Q_T.

The cell voltage is the potential difference between the redox reactions. For example, the batteries studied in this thesis, using $LiFePO_4$ as cathode and metallic Li as anode, the cell voltage is the difference in the chemical potential of the lithium atoms within the two host electrode materials ($LiFePO_4$ and Li).. Ideally, the chemical potential between the two electrodes should be maximized to increase the voltage of the battery. The storage of energy is referred to how much energy can be stored in one unit of mass, specific energy (Wh kg^{-1}) or one unit of volume, energy density (Wh L^{-1}). Specific energy is the product of capacity (mAh g^{-1}) and cell voltage (V). The theoretical energy of the overall process can be expressed by:

$$\Delta G = -nFE_{cell} \tag{1.2}$$

where n is the number of electrons transferred per mole of reactants, F is the Faraday constant (96490 C mol^{-1}) and E_{cell} is the voltage associated with the specific battery chemistry.

Another key property of an electrochemical cell is power. The power (P) delivered by a battery during the electrochemical reaction is given by the product of the current delivered by the battery and its cell voltage:

$$P = iE_{cell} \tag{1.3}$$

Where i is current flowing through the system.

Power is the rate of energy conversion. High power devices are able to provide significant amount of energy in a short period of time. Specific power or power density is the amount of power per unit of mass (W kg^{-1}) [10,23].

Among various existing technologies, Li-based batteries because of their high energy density (Figure 1.1) and design flexibility currently outperform other systems, accounting for 63% of worldwide sales values in portable batteries [17]. This explains why they receive most attention at both fundamental and applied levels.

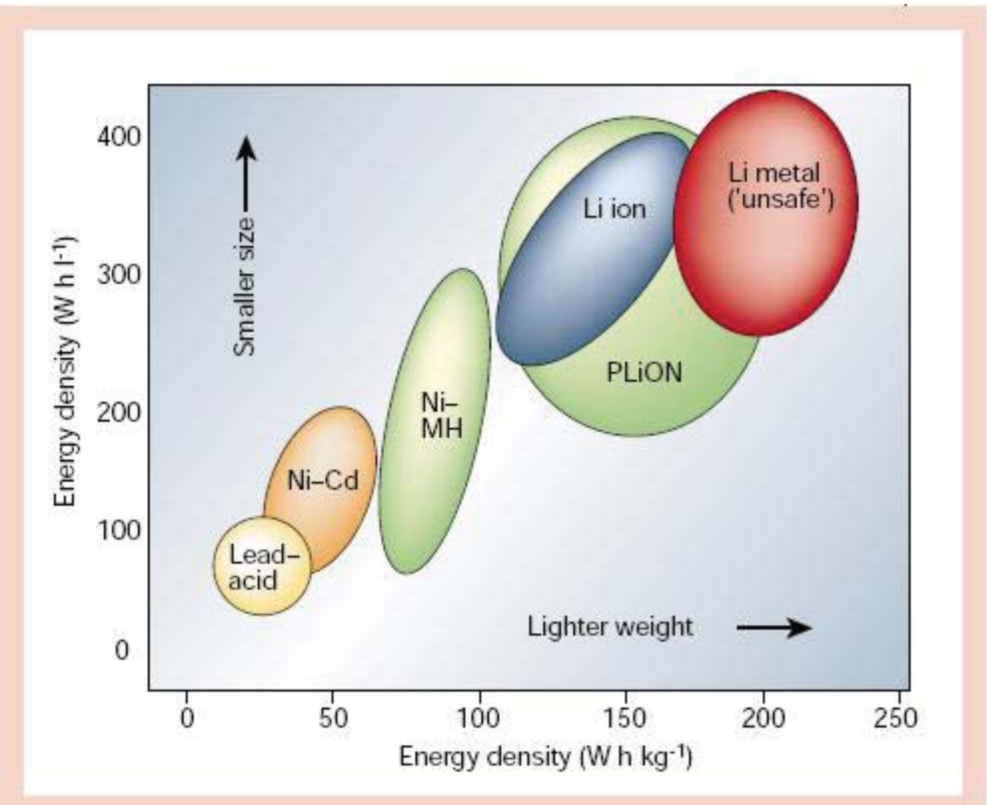

Figure 1.1: *Comparison of the different battery technologies in terms of volumetric and gravimetric energy [17].*

LIBs are based on the rocking-chair concept [5]. A typical LIB consists of a cathode (e.g., $LiCoO_2$) and an anode (e.g., graphite), together with an electrolyte-filled polymeric separator that allows lithium (Li) ion transfer but prevents electrodes from direct contact (Figure 1.2). When the battery is charging, Li deintercalates from the cathode and intercalates into the anode. Conversely, Li intercalates into the cathode via the electrolyte during discharging. During charge/discharge, Li ions flow between the anode and the cathode, enabling the conversion of chemical energy into electrical energy and the storage of electrochemical energy within the battery [24,25].

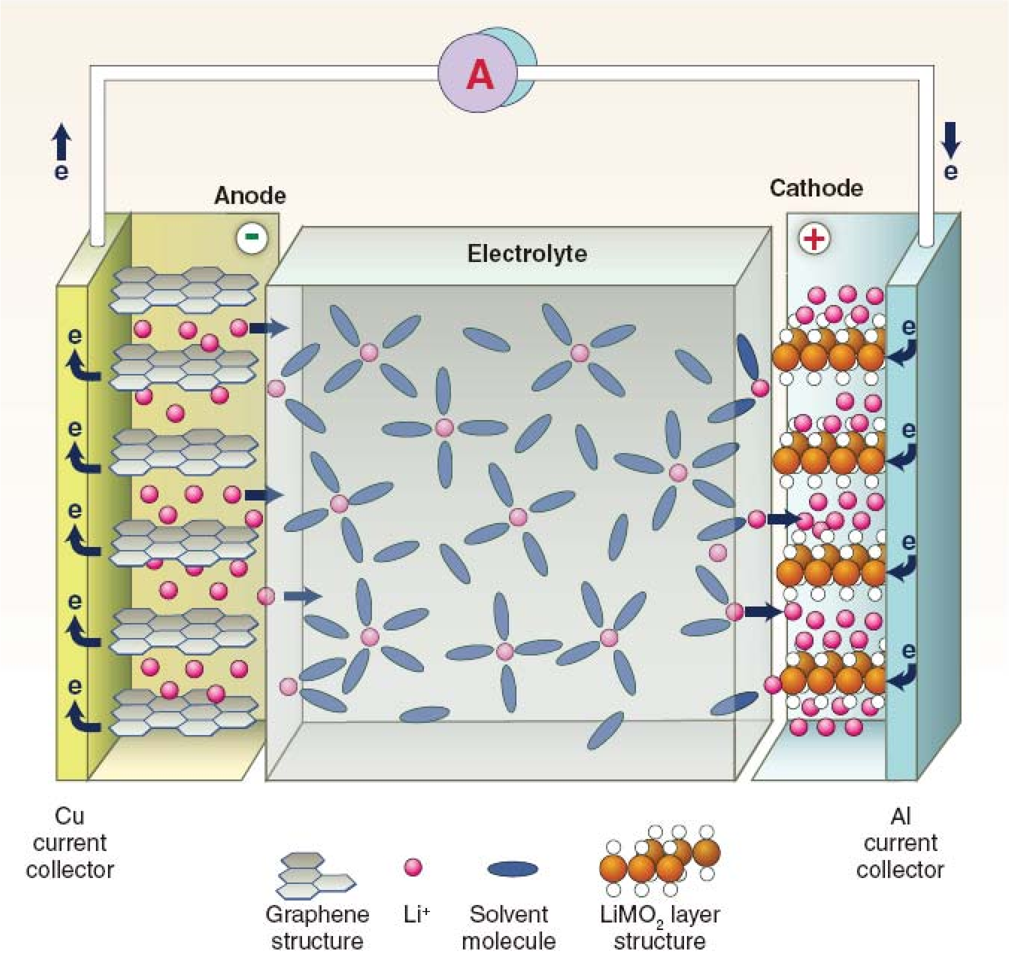

Figure 1.2: *Schematic of a LIB. The negative electrode is a graphitic carbon that holds Li in its layers, whereas the positive electrode is a Li-intercalation compound—usually an oxide because of its higher potential— that often is characterized by a layered structure. During charge and discharge, lithium ions shuttle between positive and negative electrodes. (Derived from [4])*

The chemical reactions involved in a typical LIB cell are described as follows:

Anode: $Li_xC_6 \rightarrow xLi^+ + 6C + xe^-$ (1.4)

Cathode: $Li_{(1-x)}CoO_2 + xLi^+ + xe^- \rightarrow LiCoO_2$ (1.5)

Overall reaction: $Li_xC_6 + Li_{(1-x)}CoO_2 \rightarrow C_6 + LiCoO_2$ (1.6)

The performance of rechargeable LIBs depends on active materials employed for Li storage in the electrodes. The basic requirements for active materials include high reversible capacity, good structural flexibility and stability, fast Li ion diffusion, long cycle life, improved safety, low cost, and environmental benignity [26-28]. In commercial LIBs, cathodes are mainly made from Li-ion host materials possessing high positive redox potentials such as $LiCoO_2$, $LiMn_2O_4$, and recently $LiFePO_4$ [23,29,30]. Graphite is the most used commercial anode material for LIBs because of its low and flat working potential, long cycle life, and low cost.

1.3 Cathode materials for Li-ion batteries

Unlike the anode, for which high–storage capacity materials are known to exist, the comparatively low storage capacity of current cathode materials has been recognized as a major limiting factor in the overall performance of Li-ion batteries. Since the successful commercial introduction of $LiCoO_2$ in 1991, numerous other positive electrodes have been investigated for commercial applications, but they fall mainly into two categories [20,31,32]. The first is layered lithium compounds with a close packed oxygen anion lattice, in which transition metal cations occupy alternate layers between the anions and Li ions are intercalated into the remaining empty layers. The members of this group have the advantage of higher operating voltage and specific energy than the second group owing to their highly oxidizing redox-active couples and more compact lattices. These materials are compositional variations to the layered $LiCoO_2$ (Figure 1.3*a*), such as $LiNiO_2$, $LiMnO_2$, $LiNi_{1-x}Co_xO_2$, and $LiNi_xMn_xCo_{1-2x}O_2$, as well as 3D spinel structures such as $LiMn_2O_4$ (Figure 1.3*b*). The second group consists of materials with more open structures, including layered V and Mo oxides such as V_2O_5 and MoO_3, layered or channeled compounds of Mn such as MnO_2, and transition metal phosphates such as the olivine $LiFePO_4$, with 1D Li ion diffusion channels (Figure 1.3*c*). Although they operate at lower voltages, the reduced cost, improved safety, and rate capabilities of these materials compared with the former group make them competitive cathode candidates.

This thesis will focus mainly on the $LiFePO_4$, which has recently become one of the most important cathode materials for Li-ion batteries because of its superior capacity retention, thermal stability, nontoxicity, safety, and potentially low cost [17,20,30,33].

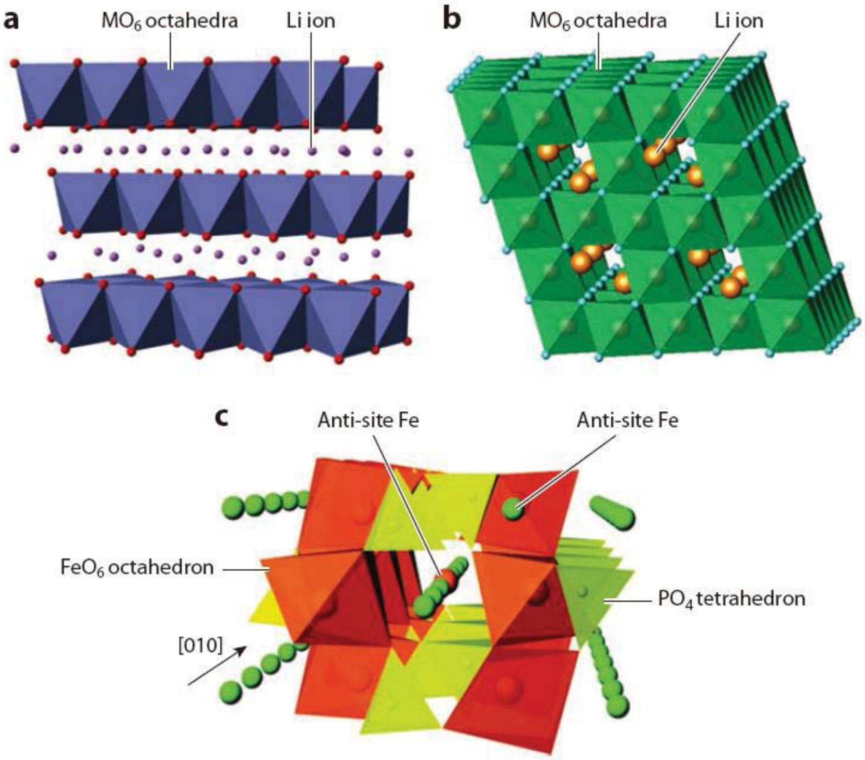

Figure 1.3: *Crystal structures of three typical cathode materials available for commercial Li-ion batteries: a) the layered* $LiCoO_2$*; b) 3D spinel structures derived from* $LiMn_2O_4$*; c) the olivine* $LiFePO_4$ *[31].*

1.3.1 The structure and characteristics of $LiFePO_4$

The olivine structure of $LiFePO_4$ was shown in Figure 1.3c. Its space group is Pnma contains four formula units, and the lattice parameters of a, b and c is 0.6008, 1.0334 and 0.4693 nm, respectively [30]. The cation arrangement in $LiFePO_4$ differs significantly from that of the layered and spinel cathode structures for LIBs. The Li and Fe ions are located in octahedral sites and P ions are located within tetrahedral sites of a distorted hexagonal close-packed framework [34,35]. The structure consists of an FeO_6 octahedron with the edge sharing of two LiO_6 octahedron and a PO_4 tetrahedron. In such a structure, there is a one dimensional tunnel formed by the edge shared Li octahedra, where Li^+ ions are mobile in this tunnel during the charge and discharge reaction of a LIB [36].

1.3.2 Synthesis methods for $LiFePO_4$

In recent years, many research groups have focused their efforts on new synthetic routes for the preparation of $LiFePO_4$ to improve its performance and reduce its cost. Methods such as solid-state reaction, sol-gel, microwave processes, hydrothermal synthesis, carbothermal reduction, spray pyrolysis technology and so forth have been used with varying degrees of success. Herein, we just review some methods which are related to our work in this thesis.

1.3.2.1 Solid-state reaction

Solid-state synthesis is a conventional method for preparing ceramics and includes several successive steps of intimate grinding and annealing of the stoichiometric mixture of starting materials. In general, in the case of $LiFePO_4$, the starting mixture consists of a stoichiometric amount of iron salt (Fe(II)-acetate, Fe(II)-oxalate), a lithium compound (lithium carbonate or lithium hydroxide), and a common phosphate source (ammonium phosphate) [30,33,37-43]. The starting mixture initiates its decomposition at the temperature of 300-400 °C expelling gases. This is followed by a calcination of the mixture at a temperatures ranging from 400 to 800 °C for 10-24 h. Typically, a carbon-containing compound, for example carboxylic acid [44], can be added to the precursor to form a carbon coated $LiFePO_4$ composite ($LiFePO_4/C$). The purity of the resulting material depends on the growth parameters, such as calcination temperature and exposure time [45,46]. During calcination, the use of inert (usually nitrogen or argon) or slightly reductive atmosphere (argon or nitrogen with the addition of hydrogen) is necessary since iron must remain in the 2+ oxidation state. Unfortunately, the presence of the residual Fe^{3+} phase is possible and often reported. Using a calcination temperature above 800 °C, both trivalent Fe_2O_3 and $Li_3Fe_2(PO_4)_3$ are formed [39]. Trivalent Fe might be formed by a small amount of oxygen included in inert gas flow and/or residual air trapped in the small pores of the particles [39]. Another disadvantage of the solid-state synthetic method is uncontrollable particle growth and agglomeration, which limits electrochemical activity [38,39,43].

1.3.2.2 Mechanochemical activation

Mechanical activation involves the blending of ingredients by high-energy ball milling followed by thermal treatment at high temperature. During mechanochemical activation, particles of the powder undergo repeated welding, fracturing and rewelding in a high-energy, ball-milling vessel. This results in pulverization, intimate powder mixing, and then solid state reaction to a new phase. Accordingly, when mechanochemical activation is applied to the synthesis of $LiFePO_4$, an improvement in electronic conductivity can be expected due to very small size of the particles and their large specific surface area [38,47,48]. However, no literature data have shown that single-phase lithium iron phosphate can be obtained by the mechanical alloying process alone without additional calcination at moderate temperatures. Nevertheless, it has been confirmed that it still provides an effective means in terms of homogenous and small particle size.

1.3.2.3 Carbothermal method

A carbothermal reduction method (CTR) [49-53] is a simple and low cost solid state method. The CTR is attractive since it uses low cost Fe^{3+} precursors and carbon and/or carbon precursor simultaneously as a reducing agent and as an in situ conductive additive. Fe_2O_3 has attracted great interests as Fe^{3+} precursors due to its low cost, good stability, nontoxicity, and environmentally friendliness.

Barker et al [52] and Kosova [53] et al. reported that $LiFePO_4$ was synthesized by a carbothermal reduction technique in inert atmosphere starting with LiH_2PO_4 and a very inexpensive and readily available Fe_2O_3:

$$LiH_2PO_4 + 0.5Fe_2O_3 + 0.25C \rightarrow LiFePO_4 + H_2O + 0.25CO_2 \quad (1.7)$$

Or $$LiH_2PO_4 + 0.5Fe_2O_3 + 0.5C \rightarrow LiFePO_4 + H_2O + 0.5CO \quad (1.8)$$

However, the high firing temperature and long reaction time utilized in CTR methods lead to a product with large particles and poor particle size distribution [54-56], and also consumes high energy which leads to an undesirable high synthesis cost.

1.3.2.4 Hydrothermal method

A hydrothermal synthetic method [57-61] is a simple and low energy consumption process to synthesize $LiFePO_4$ compared to solid state reactions that require high firing temperature and long dwell times [30]. Although it can be used to prepare fine particles, low temperature hydrothermal methods often result in the formation of olivine $LiFePO_4$ with poor crystallinity [42]. This decreases the electrochemical performance of the $LiFePO_4$ material. In addition, most previous hydrothermal methods for $LiFePO_4$ used expensive water soluble Fe^{2+} salts as starting materials [61]. More common and less expensive ferric precursors are seldom used to synthesize $LiFePO_4$ by a hydrothermal method. Yang et al synthesized $LiFePO_4$ using ferric precursors by a solvothermal method [62]. However, the use of a large excess of expensive LiI ($LiI:Fe^{3+}=10:1$), as well as an organic solvent and a surfactant will increase the synthetic cost and also make this process unfeasible for large scale production.

1.3.3 Approaches to improve the performance of $LiFePO_4$

$LiFePO_4$ has been attracting enormous research interest for its environmental friendliness, low price, non-toxic, natural abundance, high Li potential (3.4 V versus Li/Li^+) and exceptional stability. However, the main drawbacks of the olivine type $LiFePO_4$ are the low electronic conductivity and low lithium-ion diffusion coefficient [63]. To overcome these drawbacks, a number of strategies have been identified: (i) carbon coating to increase the electronic conductivity; (ii) dispersing metal powders or metal oxide coating; (iii) doping metal ions to increase the intrinsic electronic conductivity; (iv) optimization of the particle size and morphology. Herein, we will only discuss carbon coating.

Coating a layer of conductive carbon on the surface of a $LiFePO_4$ particle has been shown to be a very effective way to improve its electrochemical performance [64-67]. The addition of a carbon precursor during the synthesis of $LiFePO_4$ has the following advantages: (i) $LiFePO_4$ particles show less aggregation and are more evenly dispersed; particles; (ii) it can increase the electronic conductivity and Li-ion diffusion coefficient in $LiFePO_4$ [68]; (iii) and carbon can play the role of a reducing agent, avoiding the oxidation of iron (II) at elevated temperatures [69,70].

1.4 Anode materials for Li-ion batteries

1.4.1 Graphite

Since the launch of a commercial Li-ion battery by Sony in 1991, graphite has been the predominant anode material. Graphite is a crystalline, layered material consisting of individual *sp*^{2}-bonded graphene sheets held together by van der Waals force. It was selected as the anode material because it is inexpensive, easy to handle, abundant as well good cycling stability and safety features [71]. Because Li interacts weakly with graphite, its intercalation into graphite occurs at approximately 100 mV vs Li/Li+, which is sufficient to prevent plating of Li metal and the formation of Li dendrites that could short the electrodes and cause thermal instability [72], while maintaining a relatively high energy density for the LIB.

During the past decade, much research effort has been directed toward identifying alternative anode materials that involve new chemistry and are capable of higher theoretical capacity, higher charge/discharge rate, and greater electrode stability compared to graphite. Candidates for next-generation anode materials include insertion alloys (Si, Sn and Ge), redox metal oxides, and carbon allotropes (graphene, carbon nanotubes).

Herein, we review the metal oxides which are related to our work in this thesis.

1.4.2 Metal oxides

Various metal oxides have been extensively investigated as potential anode materials for rechargeable LIBs because these materials have diverse chemical and physical properties and can deliver high reversible capacities between 500 and 1000 mAh g^{-1} [73-81]. Metal oxide-based anodes can be classified into three groups depending on their reaction mechanisms: (i) Li alloy reaction mechanism, (ii) insertion/extraction reaction mechanism that involves the insertion and extraction of Li into and from the lattice of the transition metal oxide, and (iii) conversion reaction mechanism that involves the formation and decomposition of Li oxide (Li_2O), accompanying the reduction and oxidation of metal nanoparticles. The three reaction mechanisms are displayed as follows:

(i) Li-alloy reaction mechanism:

$$M_xO_y + 2yLi^+ + 2ye^- \rightarrow xM + yLi_2O \tag{1.9}$$

$$M + zLi^+ + ze^- \leftrightarrow Li_zM \tag{1.10}$$

(ii) Insertion reaction mechanism:

$$MO_x + yLi^+ + ye^- \leftrightarrow Li_yMO_x \tag{1.11}$$

(iii) Conversion reaction mechanism:

$$M_xO_y + 2yLi^+ + 2ye^- \leftrightarrow xM + yLi_2O \tag{1.12}$$

Herein, we discuss only the conversion reaction mechanism.

1.4.2.1 Conversion reaction mechanism

The conversion reaction mechanism has brought great interest since many important transitional metal oxides (MO_x, where M is Fe, Co, Ni, Cu, Mo, Ni, Gr, Ru, etc.) follow this route during electrode reactions [73,74]. According to Eq. (1.12), these oxides are converted to a metallic state along with the formation of Li_2O during the first lithiation and are reversibly returned to its initial state after delithiation. Anodes made from these metal oxides exhibit high reversible capacities and high energy densities because the various oxidation states of the M atom are fully utilized and more than one electron is involved in the conversion reaction [73,74,82-84]. However, they often show low coulombic efficiency (lower capacity obtained on delithition compared to lithiation) during the first cycle, unstable solid electrolyte interphase (SEI: a film composed of inorganic and organic electrolyte decomposition products formed during the initial charging of the battery) film formation, large potential hysteresis (Li insertion potential versus de-insertion potential), and poor capacity retention.

In the following section, we discuss one of the most widely studied conversion reaction-based transition metal oxide anodes: iron oxides.

1.4.2.2 Iron oxides

Iron oxides, such as hematite (Fe_2O_3) are attractive conversion reaction-based anode materials for rechargeable LIBs because of their very low cost and non-toxicity [83,84]. Li can be reversibly inserted into Fe_2O_3 in a wide potential range, e.g., 1.5–4.0 V vs. Li/Li^+. When lowering the potential to 0.9 V, an additional two moles of Li can react with Fe, but they cannot be extracted without damaging the crystal structure of the material [85,86]. A total of 8.5 moles of Li can react with each Fe_2O_3.

This yields a total theoretical capacity of 1007 mAh g^{-1} by the formation of Fe^0 from Fe^{3+} in Fe_2O_3. Recently, diverse α-Fe_2O_3 nanostructures, including nanoparticles [87,88], nanocubes [89], nanorods [90], and nanotubes [91], have been successfully synthesized, which promotes the increased use of iron oxide as a possible anode material.

1.5 Motivation and goals

Rechargeable Li-ion cells are key components of the portable, entertainment, computing and telecommunication equipment required by today's information-rich, mobile society. Despite the impressive growth in sales of batteries worldwide, the science underlying battery technology is often criticized for its slow advancement. It is now universally accepted that breakthroughs in lithium battery technology require innovative chemistries for both the electrode and the electrolyte components. Now worldwide research and development efforts are directed toward the replacement of the present battery components with materials having higher performance in terms of energy, power, cost, reliability, lifetime and safety [92].

Based on these research directions, we have developed two areas of concentration within this thesis. Part 1 concerns cathode materials, where, we exploit a low temperature hydrothermal method using low cost Fe^{3+} precursors to synthesize $LiFePO_4$ and $LiFe_{0.3}Mn_{0.7}PO_4$. The low temperature synthetic route with the low cost precursor will reduce the large scale synthetic cost for these materials, favoring their commercialization. **Initially**, a $LiFePO_4/C$ composite material was synthesized from a Fe_2O_3 precursor by a hydrothermal method to make $LiFePO_4(OH)$ in a first step followed by a fast calcination and carbon coating. The as-prepared $LiFePO_4/C$ provides enhanced discharge capacity and cycling stability compared to $LiFePO_4$ synthesized using a solid state method. **Secondly**, $LiFePO_4$ with good crystallinity and high purity was synthesized, in one step, with nanometric sized Fe_2O_3 by a hydrothermal method. **Thirdly**, $LiFe_{0.3}Mn_{0.7}PO_4$ has been prepared using low cost Fe_2O_3 as a precursor within the hydrothermal synthetic method. The low discharge capacity for the as-prepared $LiFe_{0.3}Mn_{0.7}PO_4$ material requires improvements through a more detailed analysis of the synthetic and electrochemical mechanisms.

The second part of this thesis is concerned about an improved anode material, α-Fe_2O_3, which has attracted great interests due to attractive features such as low cost, good stability, nontoxicity, and environmentally friendliness. In this thesis, we prepared α-Fe_2O_3 nanoparticles using two hydrothermal methods microwave assisted (MAH) and conventional hydrothermal (CH), both of which are promising methods to synthesize unique nano particles. We compared the physical properties and electrochemical performance of Fe_2O_3 prepared from both synthetic techniques. The CH-α-Fe_2O_3 material shows improved cycling performance and retains over 450 mAh g^{-1} for 15 cycles, indicating that CH is a more suitable method to prepare a low cost anode material, α-Fe_2O_3, with good electrochemical performance.

In summary, the goal of this thesis is to develop low cost cathode and anode materials with good performance for the lithium ion battery to grow the market and use of lithium-ion batteries.

1.6 References

1. Choi, N.-S.; Chen, Z.; Freunberger, S. A.; Ji, X.; Sun, Y.-K.; Amine, K.; Yushin, G.; Nazar, L. F.; Cho, J.; Bruce, P. G. *Angew. Chem. Int. Ed.* **2012**, 51, 9994.
2. Etacheri, V.; Marom, R.; Elazari, R.; Salitra, G.; Aurbach, D. *Energy Environ. Sci.* **2011**, 4, 3243.
3. Jeong, G.; Kim, Y.-U.; Kim, H.; Kim, Y.-J.; Sohn, H.-J. *Energy Environ. Sci.* **2011**, 4, 1986.
4. Dunn, B.; Kamath, H.; Tarascon, J.-M. *Science* **2011**, 334, 928.
5. Ji, L.; Lin, Z.; Alcoutlabi, M.; Zhang, X. *Energy Environ. Sci.* **2011**, 4, 2682.
6. Long, J. W.; Dunn, B.; Rolison, D. R.; White, H. S. *Chem. Rev.* **2004**, 104, 4463.
7. Chen, J.; Cheng, F. *Acc. Chem. Res.* **2009**, 42, 713.
8. Kim, M. G.; Cho, J. *Adv. Funct. Mater.* **2009**, 19, 1497.
9. Bruce, P. G.; Scrosati, B.; Tarascon, J.-M. *Angew. Chem. Int. Ed.* **2008**, 47, 2930.
10. Winter, M.; Brodd, R. J. *Chemical Reviews* **2004**, 104, 4245.
11. Arico, A. S.; Bruce, P.; Scrosati, B.; Tarascon, J.-M.; van Schalkwijk, W. *Nat. Mater.* **2005**, 4, 366.
12. Baxter, J.; Bian, Z.; Chen, G.; Danielson, D.; Dresselhaus, M. S.; Fedorov, A. G.; Fisher, T. S.; Jones, C. W.; Maginn, E.; Kortshagen, U.; Manthiram, A.; Nozik, A.; Rolison, D. R.; Sands, T.; Shi, L.; Sholl, D.; Wu, Y. *Energy Environ. Sci.* **2009**, 2, 559.
13. Deng, D.; Kim, M. G.; Lee, J. Y.; Cho, J. *Energy Environ. Sci.* **2009**, 2, 818.

14. Kang, K.; Meng, Y. S.; Bréger, J.; Grey, C. P.; Ceder, G. *Science* **2006**, 311, 977.

15. Manthiram, A.; Vadivel Murugan, A.; Sarkar, A.; Muraliganth, T. *Energy Environ. Sci.* **2008**, 1, 621.

16. Meng, Y. S.; Arroyo-de Dompablo, M. E. *Energy Environ. Sci.* **2009**, 2, 589.

17. Tarascon, J. M.; Armand, M. *Nature* **2001**, 414, 359.

18. Thavasi, V.; Singh, G.; Ramakrishna, S. *Energy Environ. Sci.* **2008**, 1, 205.

19. Wakihara, M. *Mater. Sci. Engi. R* **2001**, 33, 109.

20. Whittingham, M. S. *Chem. Rev.* **2004**, 104, 4271.

21. Winter, M.; Besenhard, J. O.; Spahr, M. E.; Novák, P. *Adv. Mater.* **1998**, 10, 725.

22. Palacin, M. R. *Chem. Soc. Rev.* **2009**, 38, 2565.

23. Peng, B.; Chen, J. *Coord. Chem. Rev.* **2009**, 253, 2805.

24. Chen, J.; Wang, J. Z.; Minett, A. I.; Liu, Y.; Lynam, C.; Liu, H.; Wallace, G. G. *Energy Environ. Sci.* **2009**, 2, 393.

25. Landi, B. J.; Ganter, M. J.; Cress, C. D.; DiLeo, R. A.; Raffaelle, R. P. *Energy Environ. Sci.* **2009**, 2, 638.

26. Guo, Y.-G.; Hu, J.-S.; Wan, L.-J. *Adv. Mater.* **2008**, 20, 2878.

27. Armand, M.; Grugeon, S.; Vezin, H.; Laruelle, S.; Ribiere, P.; Poizot, P.; Tarascon, J. M. *Nat. Mater.* **2009**, 8, 120.

28. Tarascon, J.-M.; Recham, N.; Armand, M.; Chotard, J.-N.; Barpanda, P.; Walker, W.; Dupont, L. *Chem. Mater.* **2009**, 22, 724.

29. Li, H.; Wang, Z.; Chen, L.; Huang, X. *Adv. Mater.* **2009**, 21, 4593.

30. Padhi, A. K.; Nanjundaswamy, K. S.; Goodenough, J. B. *J. Electrochem. Soc.* **1997**, 144, 1188.

31. Hayner, C. M.; Zhao, X.; Kung, H. H. *Ann. Rev. Chem. Biomole. Engi.* **2012**, 3, 445.

32. Wang, Y.; Cao, G. *Adv. Mater.* **2008**, 20, 2251.

33. Padhi, A. K.; Nanjundaswamy, K. S.; Masquelier, C.; Okada, S.; Goodenough, J. B. *J. Electrochem. Soc.* **1997**, 144, 1609.

34. Zhang, Y.; Huo, Q.-y.; Du, P.-p.; Wang, L.-z.; Zhang, A.-q.; Song, Y.-h.; Lv, Y.; Li, G.-y. *Synth. Met.* **2012**, 162, 1315.

35. Salah, A. A.; Mauger, A.; Julien, C. M.; Gendron, F. *Mater. Sci. Eng. B* **2006**, 129, 232.

36. Islam, M. S.; Driscoll, D. J.; Fisher, C. A. J.; Slater, P. R. *Chem. Mater.* **2005**, 17, 5085.

37. Jugovic, D.; Uskokovic, D. *J. Power Sources* **2009**, 190, 538.

38. Franger, S.; Le Cras, F.; Bourbon, C.; Rouault, H. *J. Power Sources* **2003**, 119–121, 252.

39. Yamada, A.; Chung, S. C.; Hinokuma , K. *J. Electrochem. Soc.* **2001**, 148, A224.

40. Wang, D.; Wu, X.; Wang, Z.; Chen, L. *J. Power Sources* **2005**, 140, 125.

41. Koltypin, M.; Aurbach, D.; Nazar, L.; Ellis, B. *J. Power Sources* **2007**, 174, 1241.

42. Yun, N. J.; Ha, H.-W.; Jeong, K. H.; Park, H.-Y.; Kim, K. *J. Power Sources* **2006**, 160, 1361.

43. Takahashi, M.; Tobishima, S.; Takei, K.; Sakurai, Y. *J. Power Sources* **2001**, 97–98, 508.

44. Fey, G. T.-K.; Lu, T.-L. *J. Power Sources* **2008**, 178, 807.

45. Julien, C. M.; Mauger, A.; Ait-Salah, A.; Massot, M.; Gendron, F.; Zaghib, K. *Ionics* **2007**, 13, 395.
46. Zaghib, K.; Ravet, N.; Gauthier, M.; Gendron, F.; Mauger, A.; Goodenough, J. B.; Julien, C. M. *J. Power Sources* **2006**, 163, 560.
47. Kwon, S. J.; Kim, C. W.; Jeong, W. T.; Lee, K. S. *J. Power Sources* **2004**, 137, 93.
48. Kosova, N.; Devyatkina, E. *Solid State Ion.* **2004**, 172, 181.
49. Liu, H.; Zhang, P.; Li, G. C.; Wu, Q.; Wu, Y. P. *J. Solid State Electrochem.* **2008**, 12, 1011.
50. Kim, C. W.; Lee, M. H.; Jeong, W. T.; Lee, K. S. *J. Power Sources* **2005**, 146, 534.
51. Liu, H.-p.; Wang, Z.-x.; Li, X.-h.; Guo, H.-j.; Peng, W.-j.; Zhang, Y.-h.; Hu, Q.-y. *J. Power Sources* **2008**, 184, 469.
52. Barker, J.; Saidi, M. Y.; Swoyer , J. L. *Electrochem. Solid-State Lett.* **2003**, 6, A53.
53. Kosova, N. V.; Devyatkina, E. T.; Petrov, S. A. *J. Electrochem. Soc.* **2010**, 157, A1247.
54. Liu, A. F.; Hu, Z. H.; Wen, Z. B.; Lei, L.; An, J. *Ionics* **2010**, 16, 311.
55. Zhong, M.-e.; Zhou, Z. *Solid State Ion.* **2010**, 181, 1607.
56. Zhi, X.; Liang, G.; Wang, L.; Ou, X.; Zhang, J.; Cui, J. *J. Power Sources* **2009**, 189, 779.
57. Qian, J.; Zhou, M.; Cao, Y.; Ai, X.; Yang, H. *J. Phys. Chem. C*, 114, 3477.

58. Lu, Z.; Chen, H.; Robert, R.; Zhu, B. Y. X.; Deng, J.; Wu, L.; Chung, C. Y.; Grey, C. P. *Chem. Mater.* **2011**, 23, 2848.

59. Yang, S.; Zavalij, P. Y.; Stanley Whittingham, M. *Electrochem. Commun.* **2001**, 3, 505.

60. Ellis, B.; Kan, W. H.; Makahnouk, W. R. M.; Nazar, L. F. *J. Mater. Chem.* **2007**, 17, 3248.

61. Chen, J. J.; Whittingham, M. S. *Electrochem. Commun.* **2006**, 8, 855.

62. Yang, H.; Wu, X.-L.; Cao, M.-H.; Guo, Y.-G. *J. Phys. Chem. C* **2009**, 113, 3345.

63. Wang, K.; Cai, R.; Yuan, T.; Yu, X.; Ran, R.; Shao, Z. *Electrochim. Acta* **2009**, 54, 2861.

64. Konarova, M.; Taniguchi, I. *Mater. Res. Bull.* **2008**, 43, 3305.

65. Liao, X.-Z.; Ma, Z.-F.; He, Y.-S.; Zhang, X.-M.; Wang, L.; Jiang, Y. *J. Electrochem. Soc.* **2005**, 152, A1969.

66. Wang, Y.; Wang, J.; Yang, J.; Nuli, Y. *Adv. Funct. Mater.* **2006**, 16, 2135.

67. Hanai, K.; Maruyama, T.; Imanishi, N.; Hirano, A.; Takeda, Y.; Yamamoto, O. *J. Power Sources* **2008**, 178, 789.

68. Yang, M.-R.; Teng, T.-H.; Wu, S.-H. *J. Power Sources* **2006**, 159, 307.

69. Wang, L.; Liang, G. C.; Ou, X. Q.; Zhi, X. K.; Zhang, J. P.; Cui, J. Y. *J. Power Sources* **2009**, 189, 423.

70. Ju, S. H.; Kang, Y. C. *Mater. Chem. Phys.* **2008**, 107, 328.

71. Chang, Z.-R.; Lv, H.-J.; Tang, H.-W.; Li, H.-J.; Yuan, X.-Z.; Wang, H. *Electrochim. Acta* **2009**, 54, 4595.

72. Megahed, S.; Scrosati, B. *J. Power Sources* **1994**, 51, 79.

73. Park, C.-M.; Kim, J.-H.; Kim, H.; Sohn, H.-J. *Chem. Soc. Rev.* **2010**, 39, 3115.
74. Cabana, J.; Monconduit, L.; Larcher, D.; Palacín, M. R. *Adv. Mater.* **2010**, 22, E170.
75. Li, H.; Huang, X.; Chen, L. *Solid State Ionics* **1999**, 123, 189.
76. Nazar, L. F.; Goward, G.; Leroux, F.; Duncan, M.; Huang, H.; Kerr, T.; Gaubicher, J. *Inter. J. Inorg. Mater.* **2001**, 3, 191.
77. Obrovac, M. N.; Dunlap, R. A.; Sanderson, R. J.; Dahn, J. R. *J. Electrochem. Soc.* **2001**, 148, A576.
78. Rumplecker, A.; Kleitz, F.; Salabas, E.-L.; Schüth, F. *Chem. Mater.* **2007**, 19, 485.
79. Wu, M.-S.; Chiang, P.-C. J. *Electrochem. Commun.* **2006**, 8, 383.
80. Yue; Zhou *Chem. Mater.* **2007**, 19, 2359.
81. Zhi, L.; Hu, Y.-S.; Hamaoui, B. E.; Wang, X.; Lieberwirth, I.; Kolb, U.; Maier, J.; Müllen, K. *Adv. Mater.* **2008**, 20, 1727.
82. Villevieille, C.; Fraisse, B.; Womes, M.; Jumas, J. C.; Monconduit, L. *J. Power Sources* **2009**, 189, 324.
83. Poizot, P.; Laruelle, S.; Grugeon, S.; Dupont, L.; Tarascon, J. M. *Nature* **2000**, 407, 496.
84. Adelhelm, P.; Hu, Y.-S.; Antonietti, M.; Maier, J.; Smarsly, B. M. *J. Mater. Chem.* **2009**, 19, 1616.
85. Larcher, D.; Masquelier, C.; Bonnin, D.; Chabre, Y.; Masson, V.; Leriche, J.-B.; Tarascon, J.-M. *J. Electrochem. Soc.* **2003**, 150, A133.

86. Reddy, M. V.; Yu, T.; Sow, C. H.; Shen, Z. X.; Lim, C. T.; Subba Rao, G. V.; Chowdari, B. V. R. *Adv. Funct. Mater.* **2007**, 17, 2792.
87. Pu, Z.; Cao, M.; Yang, J.; Huang, K.; Hu, C. *Nanotech.* **2006**, 17, 799.
88. Jin, J.; Ohkoshi, S.; Hashimoto, K. *Adv. Mater.* **2004**, 16, 48.
89. Woo, K.; Lee, H. J.; Ahn, J. P.; Park, Y. S. *Adv. Mater.* **2003**, 15, 1761.
90. Yin, Y.; Alivisatos, A. P. *Nature* **2005**, 437, 664.
91. Wang, X.; Zhuang, J.; Peng, Q.; Li, Y. *Nature* **2005**, 437, 121.
92. Scrosati, B.; Garche, J. *J. Power Sources* **2010**, 195, 2419.

Chapter 2 Experimental Procedures

2.1 Synthetic Methods

A hydrothermal synthetic method is a well-established approach for preparing inorganic nanocrystals due to its simplicity. With the proper preparation, it provides a means to control the grain size, morphology and crystallinity of nanocrystals through simple changes within the experimental procedure [1-3].

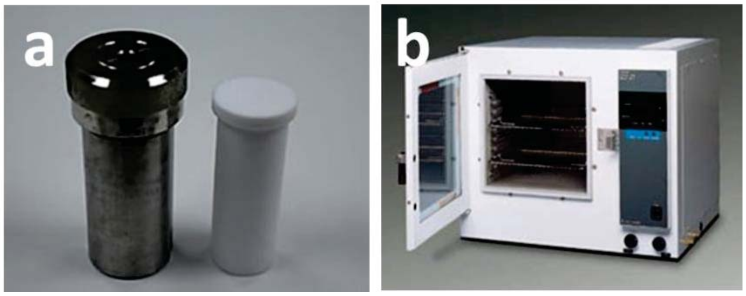

Figure 2.1: *Teflon liner, a stainless steel autoclave (a) and an oven (b) used during the conventional hydrothermal technique.*

In this thesis, both cathode ($LiFePO_4$ and $LiMn_{0.7}Fe_{0.3}PO_4$) and anode materials (Fe_2O_3) were prepared using a hydrothermal method. Figure 2.1 shows the equipment used with the conventional hydrothermal method. In a normal hydrothermal procedure, stoichiometric amounts of reactants and an excess of water are placed into a Teflon hydrothermal containment vessel (Figure 2.1a). The vessel is then purged with N_2 under sonication, sealed, and placed inside a stainless steel autoclave (Figure 2.1a). Subsequently, the autoclave is placed into an oven (Figure 2.1b) at the desired temperature.

A microwave–assisted hydrothermal method employing microwave irradiation as heat source was used during this thesis as a novel method offering shorter reaction times with a high degree of particle size and morphological control towards the particles [4-6]. Figure 2.2 shows the equipment used during the microwave-assisted hydrothermal method. The preparation procedure is essentially the same as normal hydrothermal method, but the reaction and heating vessels vary significantly. A double-walled Teflon digestion vessel is used to seal the reactants, which is then inserted into a turntable (Figure 2.2a), which is placed into a microwave digestion system (Figure 2.2b) for synthesis at the desired reaction temperature, power and time.

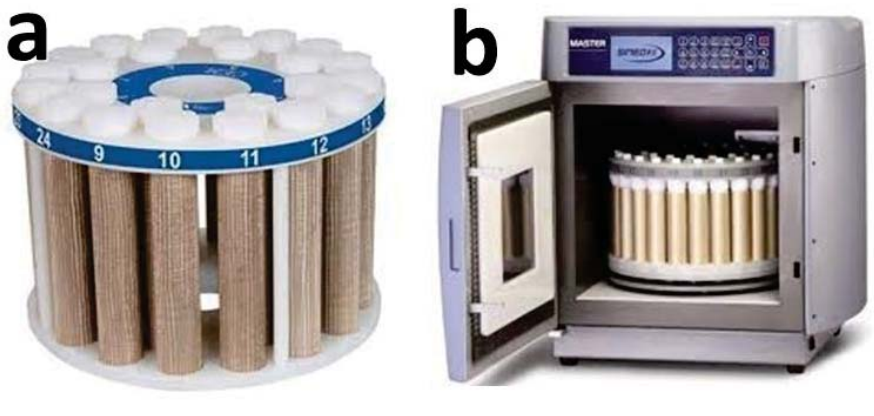

Figure 2.2: *Micro-wave equipment (b) and turntable (a) used for the micro-wave assisted hydrothermal technique.*

2.1.1 Two-Step Preparation of $LiFePO_4$/C nanoparticles

The preparation procedure of the $LiFePO_4$/C nanoparticles is described in detail in the experimental section of Chapter 3.

2.1.2 Preparation of $LiFePO_4$ using a hydrothermal method in one step

The preparation procedure of $LiFePO_4$ in one step using a hydrothermal method is described in detail in the experimental section of Chapter 4.

2.1.3 Preparation of $LiMn_{0.7}Fe_{0.3}PO_4$/C

The preparation procedure of the cathode material $LiMn_{0.7}Fe_{0.3}PO_4$/C is described in detail in Chapter 5.

2.1.4 Preparation of nano α-Fe_2O_3

The preparation procedure of nano α-Fe_2O_3 is described in detail in Chapter 6.

2.2 Characterization

2.2.1 Powder X-ray diffraction

Powder X-ray diffraction (XRD) is a versatile, non-destructive technique that reveals detailed information about the chemical composition and crystallographic structure of materials.

Max von Laue, in 1912 [8], discovered that crystalline substances act as three-dimensional diffraction gratings for X-ray wavelengths similar to the spacing of planes in a crystal lattice. X-ray diffraction is now a common technique for the study of crystal structures and atomic spacing.

X-ray diffraction is based on constructive interference between monochromatic X-rays and a crystalline sample.

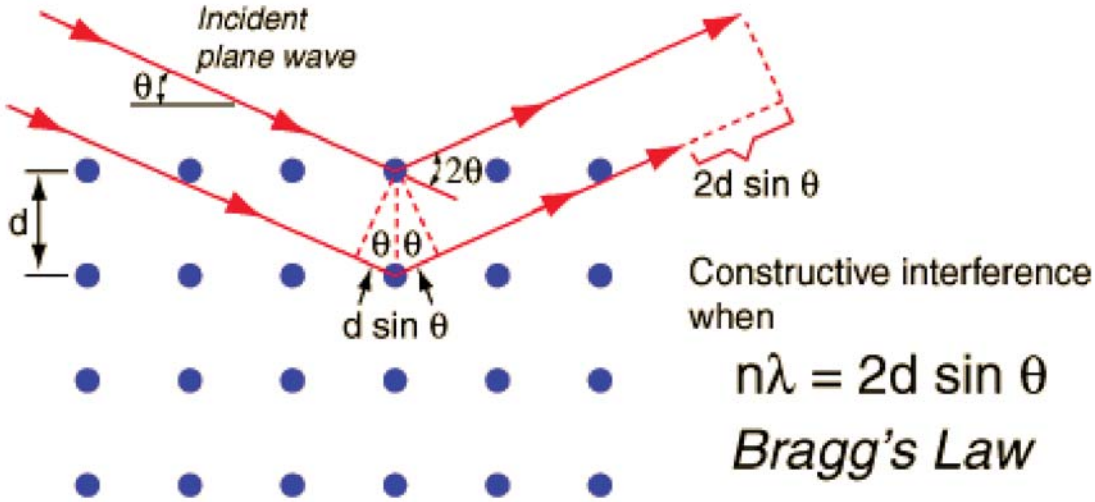

Figure 2.3: *Schematic illustration of Bragg's Law.*

X-ray that is not scattered passes through to the next layer of atoms, where again part of the X-ray is scattered and part passes through to the next layer. This causes an overall diffraction pattern, similar to how a grating diffracts a beam of light. In order for an X-ray to diffract, the sample must be crystalline and the spacing between atom layers must be close to the radiation wavelength. If beams diffracted by two different layers are in phase, constructive interference occurs and the diffraction pattern shows a peak, however if they are out of phase, destructive interference occurs appear and there is no peak. Diffraction peaks only occur when conditions satisfy Bragg's Law [8] as shown in Figure 2.3:

$$n\lambda = 2d \sin\theta \tag{2.1}$$

where θ is the angle of incidence of the X-ray, n is an integer, λ is the wavelength, and d is the spacing between atom layers. Since a highly regular structure is needed for diffraction to occur, only crystalline solids will diffract; thus amorphous materials by their disordered nature are not readily characterized by X-ray diffraction.

Bragg’s Law relates the wavelength of electromagnetic radiation to the diffraction angle and the lattice spacing within the crystalline sample. By scanning a crystalline sample through a range of 2θ angles, all possible diffraction directions of the lattice should be attained due to the random orientation of the powdered material. Conversion of the diffraction peaks to d-spacings allows identification of the mineral because each mineral has a set of unique d-spacings. Typically, this is achieved by comparison of d-spacing with standard reference patterns.

A powder X-ray diffractometer consists of an X-ray source (usually an X-ray tube), a sample stage, a detector and a way to vary angle θ, as shown in Figure 2.4. The sample rotates in the path of the collimated X-ray beam at an angle θ while the X-ray detector is mounted on an arm to collect the diffracted X-rays and rotates at an angle of 2θ. For typical powder patterns, data is collected at 2θ from ~5° to 70°. X-rays are generated in a cathode ray tube by heating a filament to produce electrons, accelerating these electrons toward a target via an applied voltage. When the incoming electrons have sufficient energy to dislodge the inner shell electrons of the target material, a characteristic X-ray spectrum of the target (Cu, Fe, Mo, Cr, Co) is produced. These spectra consist of several components, the most common being K_α and K_β. Filtering by foils or crystal monochrometers is required to produce the monochromatic X-rays needed for diffraction. Copper is the most common target material for diffraction, with Cu K_α radiation = 1.5418Å. These X-rays are collimated and directed onto the sample. As the sample and detector are rotated, the intensity of the reflected X-rays is recorded. When the geometry of the incident X-rays impinging on the sample satisfies the Bragg Equation, constructive interference occurs and a peak in intensity occurs. By scanning the sample through a range of 2θ angles, a series of peaks occur which correspond to the possible diffraction planes within the sample. A detector records and processes this X-ray signal and converts the signal to a count rate which is then recorded.

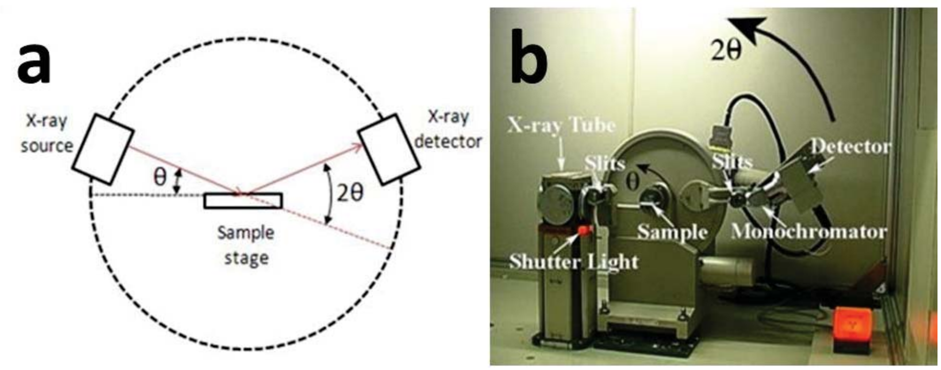

Figure 2.4: *Schematic representation and (a) a photo (b) of a powder X-ray diffractometer.*

The synthesized samples in this thesis were all analyzed by powder X-ray diffraction (XRD, Bruker D8 Advance) with either a Cu or Co Kα radiation source. The analyses were performed with a step size of 0.05° and a step time of 9 seconds in the diffraction angle range of 2θ from 15 to 70° (where 2θ is the angle between the sample and the incoming ray multiplied by two). Sample preparation included grinding the samples to powder form using a mortar and pestle and mounting the powder in specifically designed holders.

In this thesis, we employed XRD to determine the purity, crystallinity and crystal size of the as-prepared cathode and anode materials. Figure 2.5 shows an example of a typical XRD pattern for the as-prepated $LiFePO_4$ (peaks in black). The peaks in the XRD pattern correspond to the specific diffraction planes within the $LiFePO_{4.}$ The purity of $LiFePO_4$ can be identified by comparing the standard diffraction patterns of $LiFePO_4$ ((lines in red, available in a database) with the XRD pattern of the as-prepared $LiFePO_4$ (peaks in black). The crystallinity of the material can be determined by the relative intensity of the diffraction peak (with higher crystallinity giving more intense lines, since there is a higher degree of alignment in the crystal structure leading to more Bragg diffracted electrons); while the crystal size of the material can be estimated according to the Scherrer formular:

$$L = \frac{0.9\lambda_{K\alpha_l}}{B_{(2\theta)} cos\theta_{max}}$$

Where, $\lambda_{K\alpha l}$ is the incident wavelength (1.54056 Å) and B(2θ) is the width of half peak in radians.

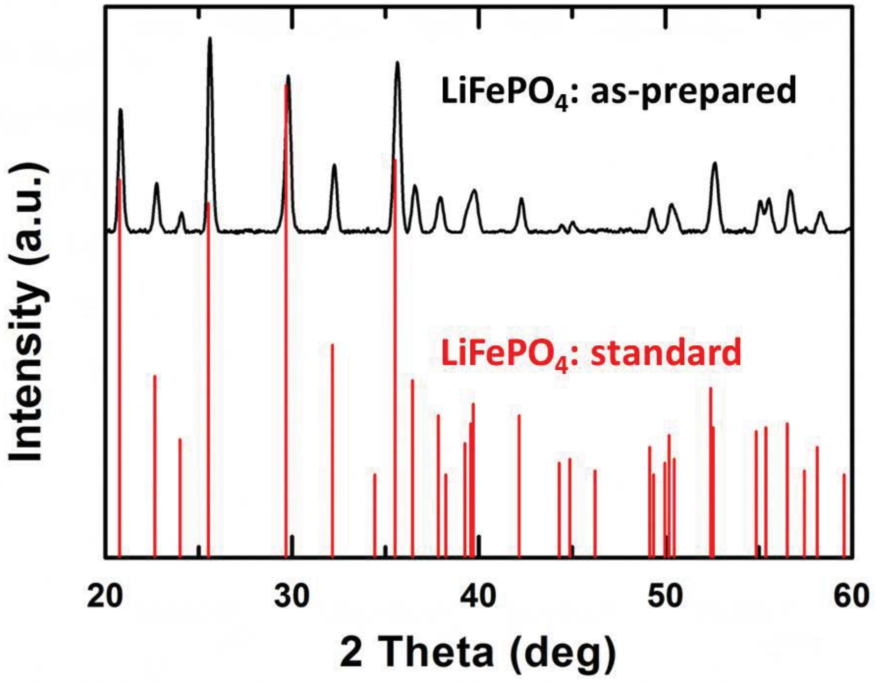

Figure 2.5: *A sample XRD pattern showing the diffraction pattern of an as-prepared LiFePO$_4$ (peaks in black) and that of a standard LiFePO$_4$ pattern (lines in red).*

2.2.2 X-ray photoelectron spectroscopy

X-ray photoelectron spectroscopy (XPS) is based on the photoelectric effect and was developed in the mid-1960's by Kai Siegbahn and his research group at the University of Uppsala, Sweden [9, 10]. Nowadays, it is a widely-used analytical technique for investigating the chemical composition, chemical and electronic state of solid surfaces.

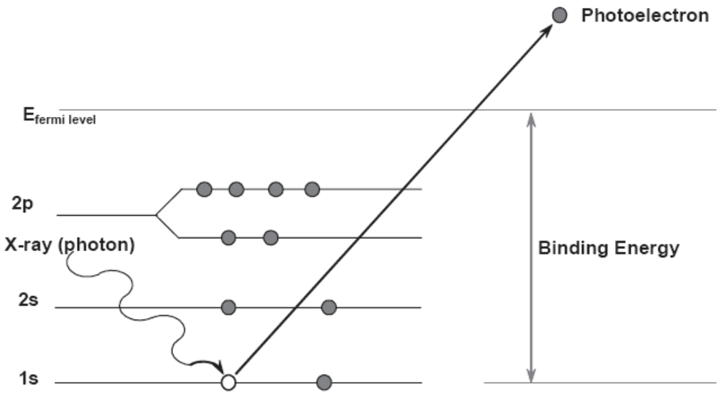

Figure 2.6: *Schematic representation of the XPS process.*

As seen from Figure 2.6, XPS spectra are obtained by irradiating a sample with mono-energetic soft X-rays (normally MgK_α 1253.6 eV or AlK_α 1486.6 eV) while simultaneously measuring the kinetic energy and number of electrons that escape from the top 1 to 10 nm of the material being analyzed. The emitted electrons have kinetic energies (KE) given by:

$$KE = hv - BE - \phi_s \tag{2.2}$$

where hv is the energy of the photon, BE is the binding energy of the atomic orbital from which the electron originates, and ϕ_s is the spectrometer work function.

As shown in Figure 2.7, an XPS instrument consists of an X-ray source, an energy analyzer for the photoelectrons, and an electron detector [9]. During a typical analysis, a sample is placed in an ultrahigh vacuum environment and exposed to a low-energy, monochromatic X-ray source. The incident X-ray causes the ejection of core-level electrons from sample atoms. The energy of a photoemitted core electron is a function of its binding energy and is characteristic of the element from which it was emitted. Energy analysis of the emitted photoelectrons is the primary data used for XPS.

When a core electron is ejected by the incident X-ray, an outer electron fills the hole left by the core electron. The energy of this transition is balanced by the emission of either an Auger electron or a characteristic x-ray for the atom. The photoelectrons and Auger electrons that are emitted from the sample are detected by an electron energy analyzer, and their energy is determined as a function of their velocity entering the detector. By counting the number of photoelectrons and Auger electrons as a function of their energy, a spectrum representing the surface composition is obtained. The energy corresponding to each peak is characteristic of a specific element present in the area under analysis. The area under a peak in the spectrum is a measure of the relative amount of the element represented by that peak. The peak shape and precise position indicates the chemical state for the element.

XPS is a surface sensitive technique because only those electrons generated near the surface escape and are detected. The photoelectrons of interest have relatively low kinetic energy. Due to inelastic collisions within the sample's atomic structure, photoelectrons originating more than 20 to 50 Å below the surface cannot escape with sufficient energy to be detected.

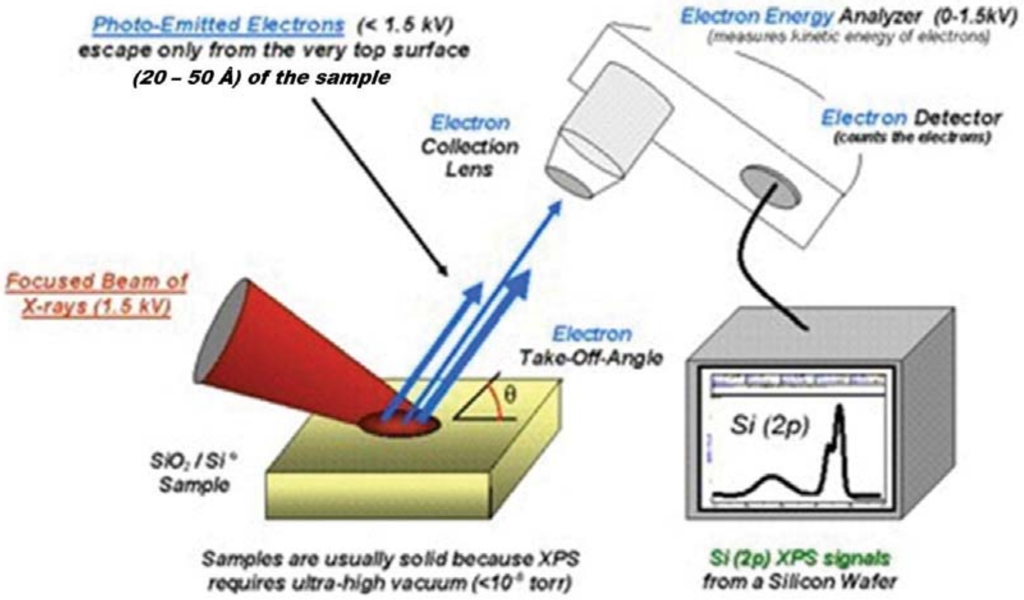

Figure 2.7: *Schematic representation and a photo of a XPS instrument.*

2.2.3 Scanning electron microscopy

A scanning electron microscope (SEM) is a type of electron microscope that produces images of a sample by scanning it with a focused beam of electrons. The electrons interact with atoms on the surface of the sample, producing various signals that can be detected and which contain information about the sample's topography and composition.

The SEM uses electrons instead of light to form an image [11-13]. It has many advantages over traditional microscopes [11-13]. The SEM has a large depth of field, which allows more of the specimen to be in focus at one time. The SEM also has much higher resolution, so closely spaced specimens can be magnified at much higher levels. Because the SEM uses electromagnets rather than lenses, the researcher has much more control in the degree of magnification required. All of these advantages, as well as strikingly clear images, make the scanning electron microscope one of the most useful instruments in research today.

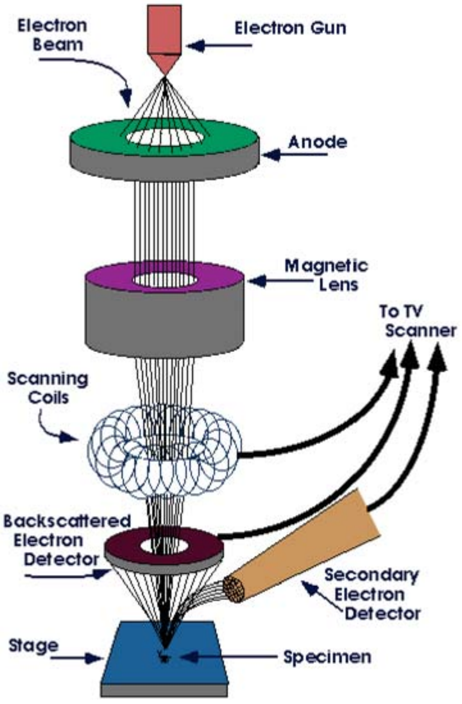

Figure 2.8: *Diagram of various components inside the SEM.*

Figure 2.9 shows schematic of a traditional SEM, whereby a beam of electrons is produced at the top of the microscope by an electron gun (Figure 2.8). The electron beam follows a vertical path through the microscope, which is held within a vacuum. The beam travels through electromagnetic fields and lenses, which focus the beam down toward the sample. Once the beam hits the sample, electrons and X-rays are ejected from the sample (Figure 2.9). Due to the low voltage used in the SEM, only electrons and X-rays on the sample's surface are ejected.

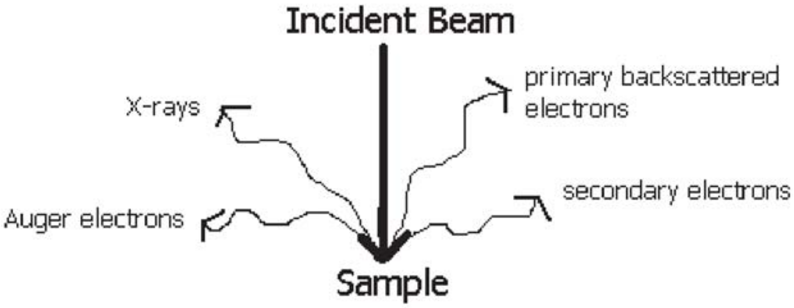

Figure 2.9: *Schematic representation of interaction of incent beam with sample.*

Detectors collect these X-rays, backscattered electrons, and secondary electrons and convert them into a signal that is sent to a screen similar to a television screen. This produces the final image.

A Field Emission Scanning Electron Microscopy (FESEM) is one of the many types of SEM instruments. It uses a field-emission cathode as the electron gun and provides a narrower electron probing beam, resulting in both an improved spatial resolution and minimized sample charging and damage.

In this thesis, SEM is a useful instrument to study the size and morphology of the synthesized nano materials. Samples described in this thesis were analyzed on a Hitachi S-4300 (FESEM) using a voltage of 5 to 10 kV with a working distance of 15 mm. All the samples were analyzed in the Laboratory of Microfabrication at the École Polytechnique de Montréal.

2.2.4 Electrochemical analysis

The synthesized materials were evaluated electrochemically in coin cells (Figure 2.8b) as the testing medium. The active material were prepared by combining 80 wt% of the active powder, 10 wt% of conductive carbon (Super-P Li, Timcal) and 10 wt% polyvinylidene difluoride (PVDF, 5% in N-methylpyrroldinone (NMP)) with an excess of NMP to form slurry. PVDF was added to the active material to act as a binder so that the electroactive material would maintain connection to the current collect over repeated charge/discharge cycles. The conductive carbon was used to ensure that each active particle in the electrode would be connected electrically. The prepared slurry was then deposited on a thin metallic current collector (Carbon coated Al for cathodes or Cu for anodes). After drying the slurry at 90 °C overnight, electrode disks (working electrode in Figure 2.10a) were punched from the foils and weighed for the cell assembly. Herein, we used standard 2032 coin-cell hardware

(Hohsen) with a piece of lithium metal foil as both counter and reference electrodes and a Celgard 2200 separator (Figure 2.10a). Cells were assembled in an argon-filled glove box using 1 M $LiPF_6$ in ethylene carbonate (EC) / diethyl carbonate (DEC) (2:1 by volume) as an electrolyte (UBE). Figure 2.10b shows an assembled lithium ion coin cell. Battery performance evaluations were performed by charging and discharging using a BT-2000 electrochemical station (Arbin).

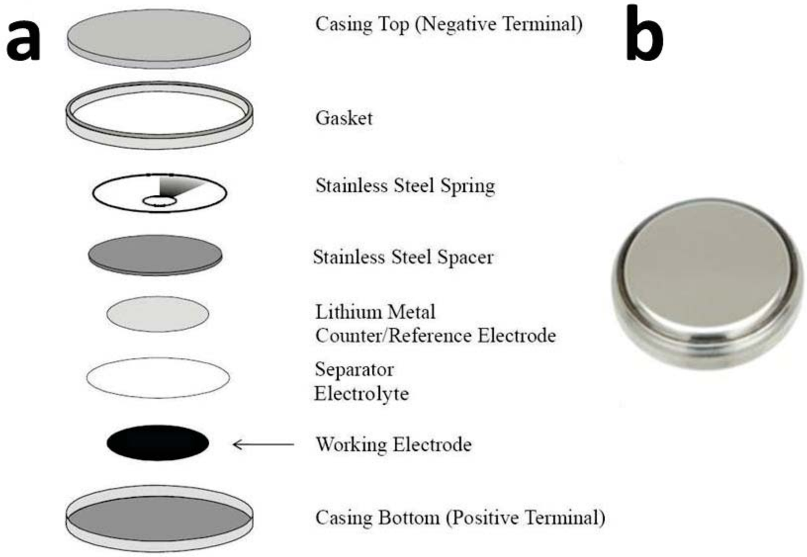

Figure 2.10: *Components (a) of a standard laboratory coin cell (b).*

The electrochemical evaluation of $LiFePO_4$ sample was performed by charging and discharging the cell from 2.2 V to 4.0 V, due to the redox couple of $Fe^{2+}/^{3+}$ that occurs at 3.45 V for $LiFePO_4$ *vs.* Li/Li^+. For the cathode material $LiMn_{0.7}Fe_{0.3}PO_4$, the electrochemical cycling was set from 2.2 to 4.5 V, based on the voltage of the redox couples $Mn^{3+}/^{4+}$ *vs.* Li/Li^+ was approximately 4 V.

For the anode material (Fe_2O_3), the cycling potentials for the experiments were set from 0.1 to 3.0 V considering the redox potential of the Fe^{3+}/Fe^{2+} (2.274 V) and Fe^{2+}/Fe (2.065 V) *vs*. Li/Li$^+$.

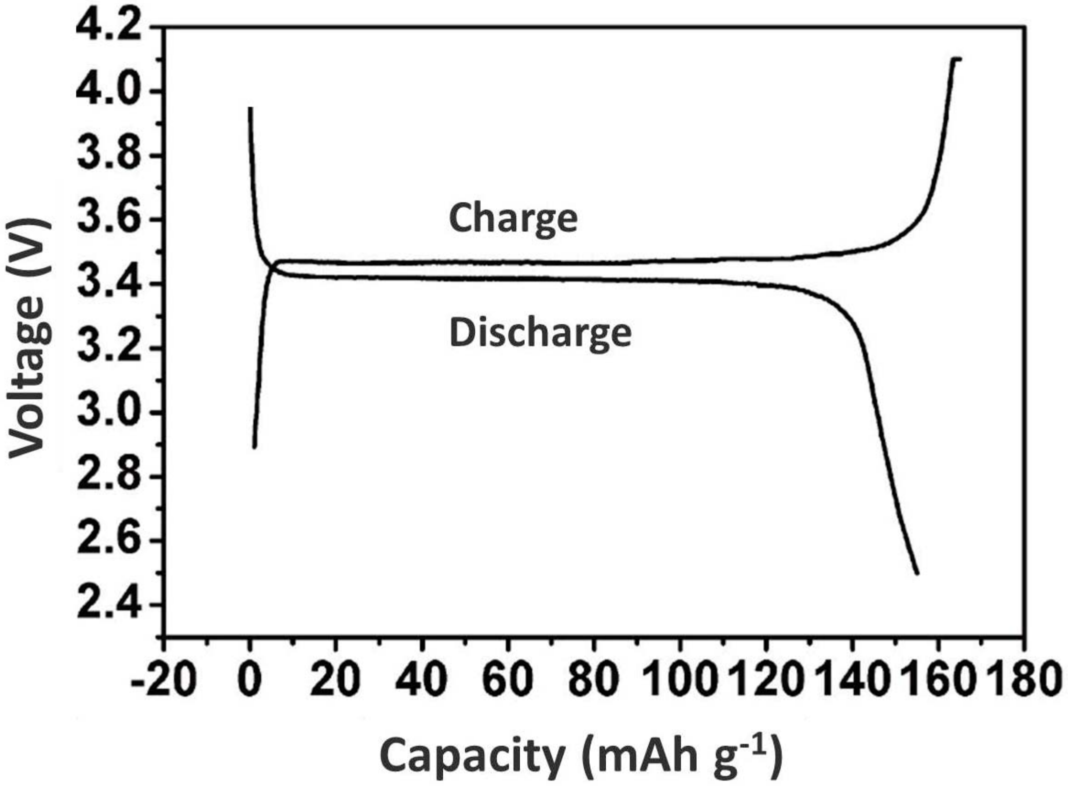

Figure 2.11: *A typical charge and discharge curve for* $LiFePO_4$ *at 0.1C (170 mA* g^{-1}*).*

Figure 2.11 provides an example of a typical charge/discharge curve for $LiFePO_4$. Here, the battery was charged and discharged between 2.5V and 4V vs Li/Li+, indicated by the y-axis.. The x-axis (capacity) is an indication of the number of electrons (and thus Li atoms) removed (charge) and inserted (discharge) from the material. There is a different in voltage between charge and discharge due to a number of processes including the impedance within the cell. The applied current used during this test is expressed in terms of “C-Rate”, where a C-Rate = C / 1 hour, where C is the battery rate capacity expressed in A-hour g^{-1}, or mA-hour g^{-1}. For instance, a 170 mA-h g^{-1} battery has a "C-Rate" of 170mA g^{-1}. The current corresponding to 0.1C charge or discharge is 17mA g^{-1} (or 1/10 the current required to fully charge (or discharge) the cell in one hour), while the current corresponding to 2C is 340mA g^{-1}. Normally, applying a high current leads to smaller capacity and a lower current leads to higher capacity due to the system being closer to an equilibrium state, minimizing possible capacity loss. In this thesis, we typically use a C/10 rate to test our batteries to provide quasi-equilibrium conditions which leads to optimal test conditions and values for capacity.

2.3 References

1. Cao, M.; Hu, C.; Peng, G.; Qi, Y.; Wang, E. *J. Am. Chem. Soc.* **2003**, 125, 4982.
2. Cao, M.; Wu, X.; He, X.; Hu, C. *Langmuir* **2005**, 21, 6093.
3. Pileni, M.-P. *Nat. Mater.* **2003**, 2, 145.
4. Subramanian, V.; Burke, W. W.; Zhu, H.; Wei, B. *J. Phys. Chem. C* **2008**, 112, 4550.
5. Guo, Y.-G.; Lee, J.-S.; Hu, Y.-S.; Maier, J. *J. Electrochem. Soc.* **2007**, 154, K51.
6. Liu, Y.; Chu, Y.; Zhuo, Y.; Li, M.; Li, L.; Dong, L. *Cryst. Growth Des.* **2007**, 7, 467.
7. Wu, X. L.; Guo, Y. G.; Wan, L. J.; Hu, C. W. *J. Phys. Chem. C* **2008**, 112, 16824.
8. Atkins, P.; Paula, J. d., *Physical Chemistry*, 8th ed., University of Oxford, **2006**.
9. Wagner, C. D.; Riggs, W. M.; Davis, L. E.; Moulder, J. F.; Muilenberg, G. E., *Handbook of X-ray Photoelectron Spectroscopy*, 1st ed., Perkin-Elemer Corporation, **1979**.
10. Watts, J. F.; Wolstenholme, J., *An Introduction to Surface Analysis by XPS and AES*, John Wiley & Sons Ltd, **2003**.
11. Goldstein, J.; Newbury, D. E.; Joy, D. C.; Lyman, C. E.; Echlin, P.; Lifshin, E.; Sawyer, L.; Michael, J. R., *Scanning Electron Microscopy and X-Ray Microanalysis*, 3rd ed., Springer, **2003**.
12. Flegler, S. L.; Heckman, J. W.; Klomparens, K. L., *Scanning and Transmission electron microscopy: An Introduction*, Oxford University Press, **1993**.

13. Egerton, R. F., *Physical Principles of Electron Microscopy: An Introduction to TEM, SEM, and AEM*, Springer, **2005**.

Chapter 3 Low Cost Synthesis of $LiFePO_4$/C Cathode Materials with Fe_2O_3

Lifeng Cheng[a], Guoxian Liang[b], Soumia El Khakani[a], Dean D. MacNeil[a*]

[a] Département de Chimie, Université de Montréal, Montréal, Québec H3T 1J4, Canada

[b] Clariant (Canada) Inc., 1475 Rue Marie-Victorin, St-Bruno, Québec J3V 6B7, Canada

Chapter 3 consists of an article published in the Journal of Power Sources (J. Power Sources. **2013**, 242, 656-661). *The article was prepared by the authors under the supervision of Dr. MacNeil and Dr. Guoxian Liang. Soumia El Khakani, Ph.D student in Dr. MacNeil's lab aided with the electrochemical tests.*

Abstract

$LiFePO_4$/C composite materials have been synthesized from a low cost Fe_2O_3 precursor by a hydrothermal method to make $LiFePO_4(OH)$ in a first step followed by a fast calcination and carbon coating. This method combines the advantages of both hydrothermal and solid state synthetic methods. The as-prepared $LiFePO_4$/C provides enhanced discharge capacity and cycling stability compared to $LiFePO_4$ synthesized using a solid state method with the same precursors. Thus, the method to be described herein is a promising option in the search to reduce the cost of large-

scale synthesis of $LiFePO_4/C$ for use in lithium-ion batteries, while maintaining adequate electrochemical performance.

***Keywords**:* lithium ion battery; lithium iron phosphate; ferric oxide; hydrothermal method; low cost; citric acid.

3.1 Introduction

Olivine-type $LiFePO_4$ has recently become one of the most important cathode materials for Li-ion batteries because of its superior capacity retention, thermal stability, nontoxicity, safety, and potentially low cost [1-4]. Despite these advantages, olivine $LiFePO_4$ has some disadvantages such as low intrinsic electronic and ionic conductivity [5-8]. One approach to overcome this insulating nature is to coat active particles with conductive carbon [9-13], while the poor lithium ion diffusion is addressed by synthesizing small particles with high purity [14-17].

A hydrothermal synthetic method [18-22] is a simple and low energy consumption procedure compared to solid state reactions that require high firing temperature and long dwell times [1]. Although they can be used to prepare fine particles, low temperature hydrothermal methods often result in the formation of olivine $LiFePO_4$ with poor crystallinity [23]. This decreases the electrochemical performance of the resulting $LiFePO_4$ material. In addition, most previous hydrothermal methods for $LiFePO_4$ used expensive water soluble Fe^{2+} salts as starting materials [18]. More common and less expensive ferric precursors are seldom used to synthesize $LiFePO_4$ by a hydrothermal method. Yang et al synthesized $LiFePO_4$ using ferric precursors by a solvothermal method [24], however, a large excess of expensive LiI ($LiI:Fe^{3+}=10:1$), as well as an organic solvent would increase the synthetic cost and make this process unfeasible for large-scale production.

Currently, the cost of lithium-ion batteries is still too high, with material costs accounting for up to 80% and 90% of the total costs of high power and high energy batteries, respectively [25]. Thus, there is a great potential for reducing the costs of lithium-ion batteries through development of low cost materials and material processing techniques [26, 27]. Clearly, novel large scale/low cost synthetic methods using low cost raw materials need to be developed.

In this work, we have employed a low cost ferric oxide (Fe_2O_3) and LiH_2PO_4 as precursor materials to prepare low cost electrochemically active $LiFePO_4$/C in two steps. In the first step, $LiFePO_4(OH)$ (tavorite) was obtained by a hydrothermal method using citric acid as a chelating agent. β-lactose was then mixed with the $LiFePO_4(OH)$ particles and the mixture was heated for a short period under a N_2 atmosphere to form $LiFePO_4$/C. The simultaneous realization of a carbon coating and $LiFePO_4(OH)$ reduction greatly improved the crystallinity, conductivity and thus the electrochemical performance of the resulting $LiFePO_4$ material.

3.2 Experimental

3.2.1 Preparation of LiFePO4/C nanoparticles

The preparation of $LiFePO_4/C$ nanoparticles was realized in two steps following the schema shown in Figure 3.1.

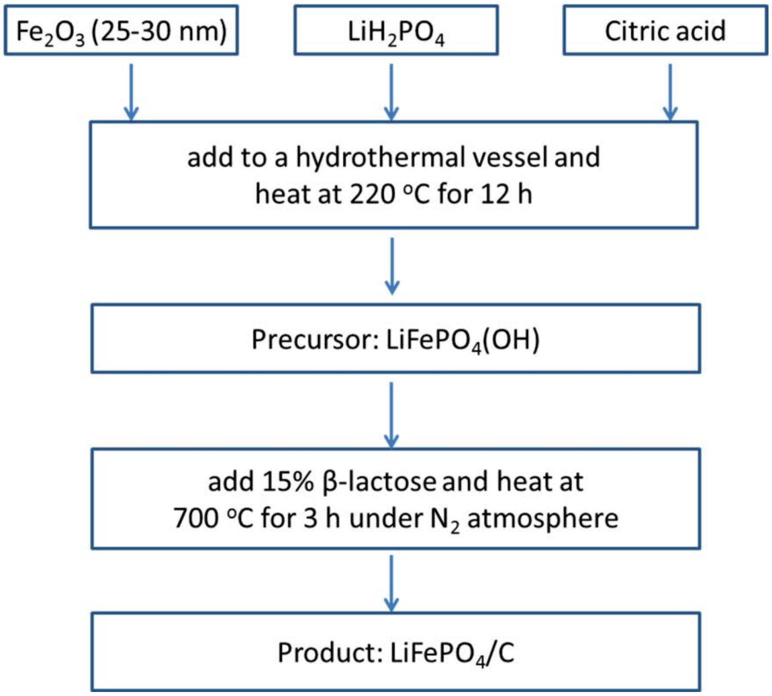

Figure 3.1: *Flow chart for the preparation of* $LiFePO_4/C$ *using nano-*Fe_2O_3 *precursor*

a) Synthesis of $LiFePO_4(OH)$ precursor using a hydrothermal method

Stoichiometric amounts of LiH_2PO_4, Fe_2O_3 (25-30 nm, Sigma—Aldrich Co. LLC) and citric acid were added to 30 ml of water in a 40 ml Teflon-lined hydrothermal vessel. The vessel was purged with N_2 under sonication, sealed, and then placed inside a stainless steel autoclave. Subsequently, the autoclave was placed into an oven at 220 °C for 12 hours. After cooling naturally to room temperature, the suspension was dried under continuous stirring at 80 °C. The solid sample was then analyzed by XRD and found to be mainly $LiFePO_4(OH)$. For comparison purposes, a second batch of $LiFePO_4(OH)$ was prepared using the above method, but in the absence of citric acid.

b) Synthesis of $LiFePO_4/C$ from the as-prepared $LiFePO_4(OH)$

Heat treating $LiFePO_4(OH)$ in the presence of β-lactose was performed for two purposes: a) to realize the formation of a carbon coating on the surface; and, b) the reduction of $LiFePO_4(OH)$ to $LiFePO_4$. β-lactose (Sigma—Aldrich Co. LLC) with a 15% weight ratio with respect to $LiFePO_4$ was dissolved in 5ml of distilled water and 40 ml of IPA (Isopropyl Alcohol).To the solution, $LiFePO_4(OH)$ was added and the resulting slurry was dried at 80 ^{o}C for 3 hours under vigorous stirring to remove the excess water and IPA. The powder was then calcined at 700 ^{o}C for 3 hours in a tube furnace under a N_2 atmosphere to obtain $LiFePO_4/C$.

3.2.2 Physicochemical characterizations

X-ray diffraction (XRD) was performed using a Bruker D8 Advance X-ray diffractometer equipped with Cu Kα radiation source. The particle size and morphology of each sample was examined by a Scanning Electron Microscope (Hitachi S-4300 microscope). A Fisons Instruments (SPA, model EA1108) elemental analyzer was used to determine the carbon content within the samples. The carbon content of all samples, using 2.1b, was determined to be 3.8% ± 0.1%.

3.2.3 Electrochemical measurements

Electrochemical evaluations were performed by combining 80 wt% of the $LiFePO_4$/C powder, 10 wt% of conductive carbon (Super-P Li, Timcal) and 10 wt% polyvinylidene difluoride (PVDF, 5% in N-Methylpyrrolidinone (NMP)) with an excess of NMP to form a slurry. The slurry was then deposited on a carbon coated Al foil. After drying at 90 °C overnight, electrode disks were punched and weighed for cell assembly in standard 2032 coin-cell hardware (Hohsen) using lithium metal foil as both counter and reference electrodes and a Celgard 2200 separator. The electrode area of the cathode was 1.54 cm^2 providing a $LiFePO_4$ active electrode loading of approximately 4.3 mg cm^{-2} for each sample under test. Cells were assembled in an argon-filled glove box using 1 M $LiPF_6$ in ethylene carbonate (EC) / diethyl carbonate (DEC) (2:1 by volume) as an electrolyte (UBE). Battery performance evaluations were performed by charging and discharging between 2.2 and 4.0 V with a current rate of 0.1 C at 30°C using a BT-2000 electrochemical station (Arbin).

3.3 Results and discussion

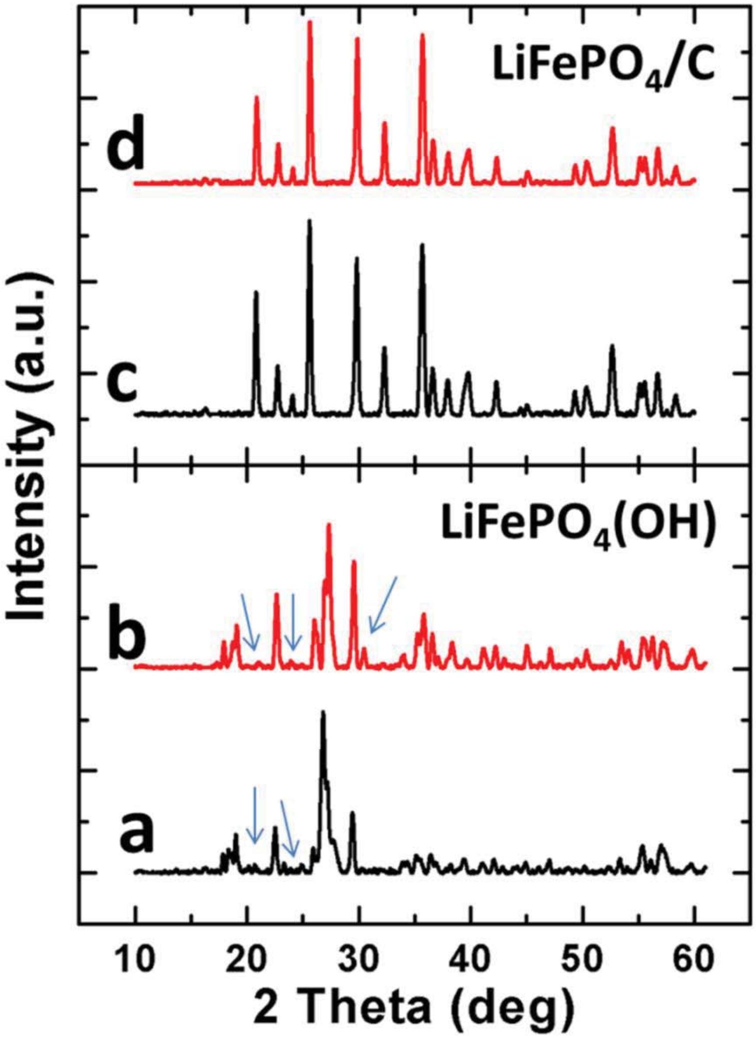

Figure 3.2: *XRD patterns of $LiFePO_4(OH)$ precursor synthesized from commercial nano Fe_2O_3 with citric acid (a) and without citric acid (b) and corresponding $LiFePO_4/C$ (c and d). Arrows indicate presence of impurities.*

Figure 3.2a and 3.2b provides the XRD patterns of $LiFePO_4(OH)$ synthesized in the presence (a) or absence (b) of citric acid using a hydrothermal method. The major peaks can be indexed to the triclinic crystal system using the $P\overline{1}$ space group [28, 29], except for several impurity peaks indicated by arrows. Citric acid, due to its strong coupling ability, has been widely used in the past as a chelating and reducing agent [21, 22, 30]. As shown in Table 3.1, the color of $LiFePO_4(OH)$ prepared with citric acid is green, while $LiFePO_4(OH)$ prepared without citric acid is yellow. The green color implies that there exists a small amount of a Fe^{2+} compound, likely the impurity seen in Figure 3.2a. Moreover, there is no obvious reduction in particle size with the addition of citric acid as calculated by the Scherrer formula (Table 3.1) [31, 32]. As mentioned in the Experimental section, the solid Fe_2O_3 precursor has a nanoscale particle size of 25-30 nm, thus, during the hydrothermal reaction, the particle size of the resulting products is not affected even in the presence of the chelating agent or surfactant. In stark comparison, a hydrothermal reaction using dissolved precursors requires a chelating agent or surfactant to be added to the solution such that the nucleation and Ostwald ripening processes can be controlled and a product with a fine particle size can be obtained.

Figure 3.2c and d shows the XRD patterns of $LiFePO_4/C$ obtained from heating $LiFePO_4(OH)$ at 700 ºC in the presence of 15% β-lactose under a N_2 atmosphere. During the heat treatment, carbon is generated from the pyrolysis of β-lactose and dispersed uniformly on the surface of $LiFePO_4(OH)$. The pyrolysis produces a strong reductive atmosphere for the resulting reduction of Fe^{3+} to Fe^{2+} and an in situ homogenous coating of carbon on the surface of the freshly formed $LiFePO_4$ particles. As seen from the XRD patterns, the in situ synthesis can produce $LiFePO_4/C$ composite materials with high crystlallinity and without impurity phases such as Fe_2O_3 and $Li_3Fe_2(PO_4)_3$ that often exist in $LiFePO_4$ products prepared by conventional solid state methods [33, 34]. In our case, we cannot identify any diffraction peaks resulting from carbon in the XRD pattern. The carbon likely exists in the form of an amorphous or a low-crystalline product on the surface of the $LiFePO_4$ samples. Another advantage of this in situ coating process is that the deposited carbon impedes the grain growth of $LiFePO_4$ at high temperature, thus limiting its size to that of the $LiFePO_4OH$ precursor (Table 3. 1).

Table 3.1: *Crystal size and color of $LiFePO_4(OH)$ and $LiFePO_4/C$ prepared with and without citric acid.*

Sample	$LiFePO_4(OH)$ with citric acid	$LiFePO_4/C$ with citric acid	$LiFePO_4(OH)$ without citric acid	$LiFePO_4/C$ without citric acid
Crystal size (nm)	28.8	33.0	29.6	33.4
Color	Green	Black	Yellow	Black

Figure 3.3 shows the SEM images of the as-synthesized $LiFePO_4(OH)$ (Figure 3.3a and b) and corresponding $LiFePO_4/C$ (Figure 3.3c and d). As shown in Figure 3.3b, $LiFePO_4(OH)$ synthesized by the hydrothermal method with citric acid exhibits a

uniform particle size distribution with an average particle size of ~0.7 μm. In contrast, for $LiFePO_4(OH)$ (Figure 3.3a) synthesized without citric acid addition, there exists an agglomeration of particles and a larger particle size distribution in the sample (from the nanoscale to the microscale).

There is no obvious change in crystallite size with the addition of citric acid, which is confirmed by the SEM images shown in Figure 3.3. However, the addition of citric acid induces a more homogenous particle distribution within the sample. This is due to the chelating nature of citric acid with iron oxide, preventing the aggregation of iron oxide and thus $LiFePO_4(OH)$. The morphology of the carbon coated $LiFePO_4$ final product is shown in Figure 3.3c and 3.3 d. As seen from SEM images, there is no obvious change in particle size after heat treatment at 700 ^{o}C during the in situ carbon deposition, which is in agreement with the XRD results. In addition, $LiFePO_4/C$ prepared with citric acid shows more uniform particle size distribution than that prepared without citric acid, as seen from the insert in Figure 3.3c and d. The carbon content in both $LiFePO_4/C$ samples is ~4 wt%.

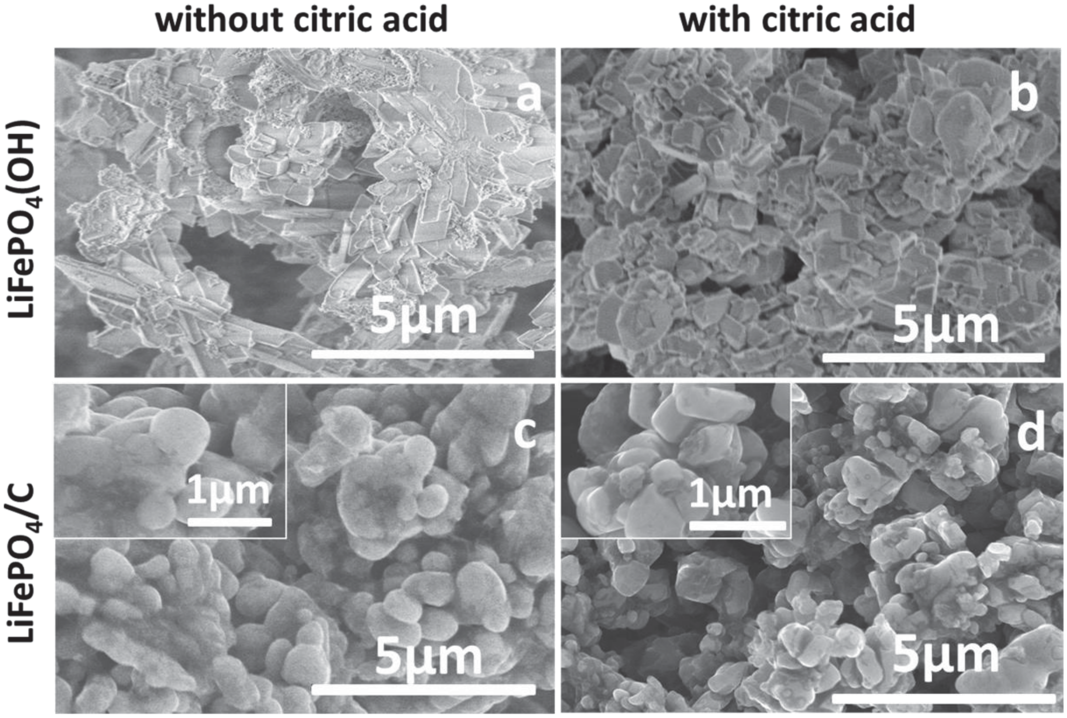

Figure 3.3: *SEM images of* $LiFePO_4$ *(OH) precursor synthesized from commercial nano* Fe_2O_3 *without citric acid (a) and with citric acid (b) and corresponding* $LiFePO_4/C$ *(c and d).*

The electrochemical properties of $LiFePO_4/C$ samples synthesized with and without citric acid during the initial hydrothermal treatment are shown in Figure 3.4. For both samples, there is an increase in capacity during the first several cycles due to the activation of electrode material that is a common for carbon coated $LiFePO_4$ [35-37]. This phenomenon has been discussed in detail in the literatures [38, 39] and can be attributed to a slow penetration of electrolyte into particles' interior. In addition, the formation of cracks within the amorphous carbon layer on $LiFePO_4$ results in a progressively increasing active surface area during the electrochemical reaction, leading to an increase in observable electrode capacity. $LiFePO_4/C$ synthesized in the absence of citric acid has a much lower specific discharge capacity (~130 mAh g^{-1} at 0.1 C) than in its presence. We believe this is due to the presence of large particles which can not be fully utilized during the electrochemical reaction, giving rise to transport limitations for both lithium ions and electrons resulting in capacity loss [40, 41]. A discharge capacity of 153 mAh g^{-1} at 0.1C is obtained for the $LiFePO_4/C$ prepared using citric acid in the reaction medium. This sample maintains high capacity even after 50 cycles (98% capacity retention), due to its high purity, small/uniform particle size, uniform carbon coating and good crystallinity.

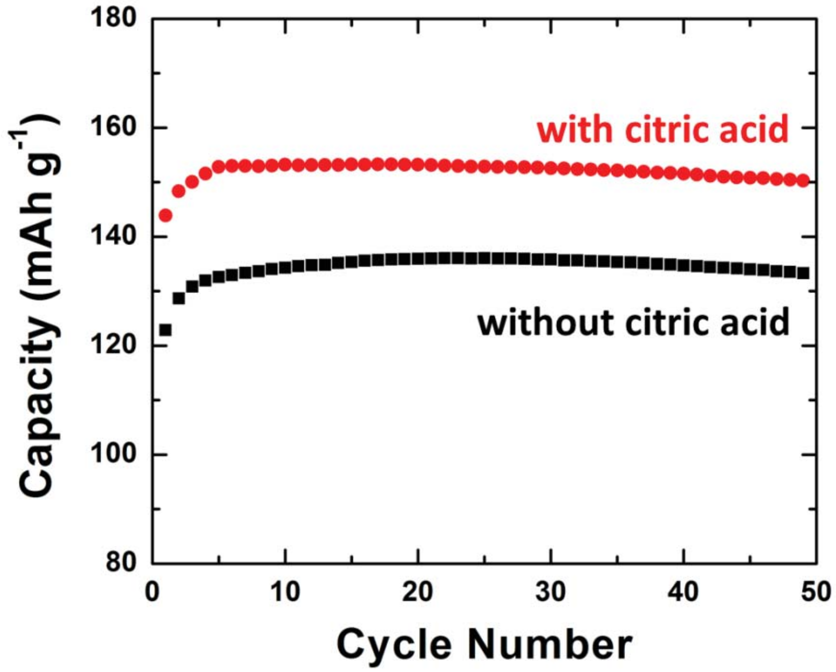

Figure 3.4: *Specific discharge capacity of batteries using* $LiFePO_4/C$ *obtained from the* $LiFePO_4$ *(OH) precursor synthesized without (black) and with (red) citric acid.*

We further optimized the initial hydrothermal treatment by varying the reaction temperature to obtain a high performing $LiFePO_4/C$ final product. Various hydrothermal temperatures (such as 140 ˚C, 160 ˚C, 180 ˚C and 220 ˚C) were explored for the preparation of $LiFePO_4(OH)$. As shown in Figure 3.5a, there is a mixture of complex products when the chosen hydrothermal temperature is below 220 ˚C. Moreover, the samples are gel like and difficult to process for post heat treatment. After heating these precursors at 700 ˚C under an N_2 atmosphere, all of them are transformed to carbon coated $LiFePO_4$， as shown in Figure 3.5b. All $LiFePO_4/C$ materials are pure and well crystallized and their electrochemical performances are shown in Figure 3.6. Clearly, their discharge capacity increases with increasing hydrothermal synthetic temperature. This is attributed to the higher crystallinity within the samples resulting from a higher hydrothermal reaction temperature.

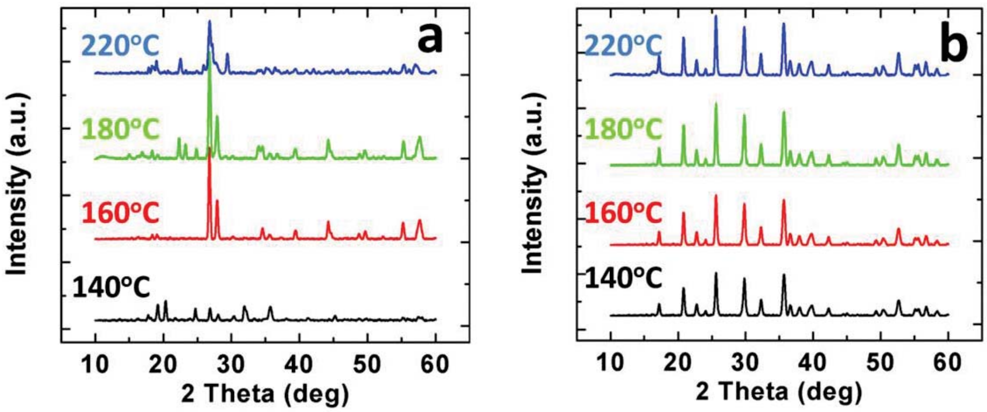

Figure 3.5: *(a) XRD patterns of precursors synthesized from commercial nano Fe_2O_3 at the indicated hydrothermal temperature (a) and corresponding $LiFePO_4/C$ final product in (b).*

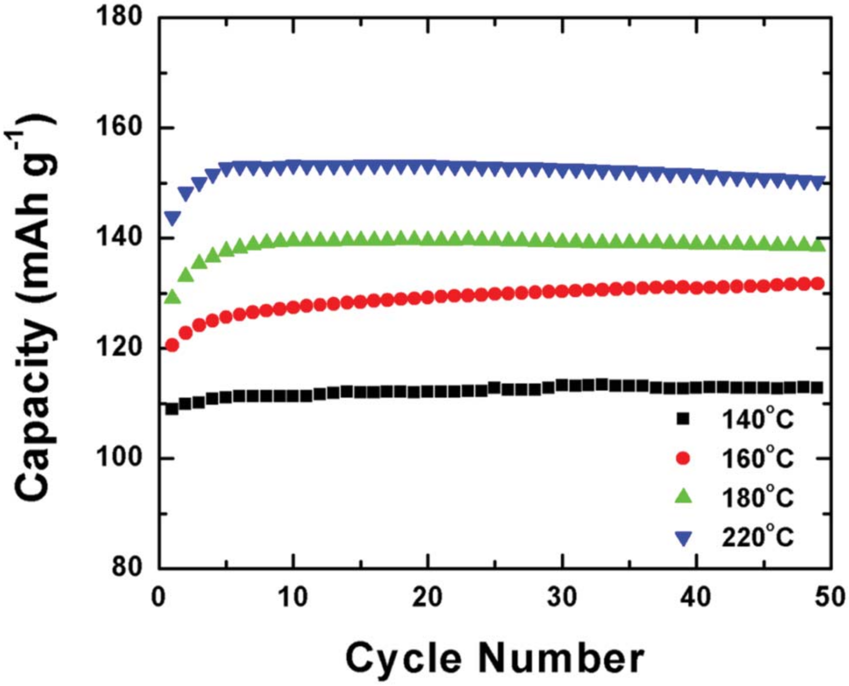

Figure 3.6: *Specific discharge capacity of batteries using* $LiFePO_4/C$ *obtained from* $LiFePO_4(OH)$ *precursors synthesized at the indicated hydrothermal temperature.*

For calcination, a temperature of 700 °C was chosen to limit particle growth and agglomeration, as well as to obtain enough carbonization to produce an electronically conductive carbon coating [17, 42]. In previous reports, low cost Fe^{3+} precursors have been used as a starting material but a long dwell time (> 10 hours) under the protection of an inert (N_2, or Ar) or reductive gas, such as N_2 (or Ar) and H_2, was required [21, 43]. In our experiments, post heat treatment was performed for only 3 hours under N_2, which may reduce the synthetic cost during large-scale implementation.

Currently, solid state reactions are considered as a suitable method for the commercial production of $LiFePO_4$. Carbon coated $LiFePO_4$ can be synthesized using LiH_2PO_4, Fe_2O_3 and carbon as raw materials by a carbothermal reduction method (CTR)[43-46], which is a simple and low cost. However, the high firing temperatures and long reaction times utilized in CTR methods leads to a product with large particles and poor particle size distribution [44].

In this work, for comparison purpose, we also synthesized $LiFePO_4/C$ using a CTR method with the same nanosize Fe_2O_3 precursors used in Section 3.2a. Two heat treatment times (3 and 10 hours) were chosen such that we could compare methods and ensure the complete reduction of Fe^{3+}. After heat treatment, both products contain a small amount of impurity identified within the XRD patterns (not shown here) and the particles tended to aggregate due to the high calcination temperatures (visible in the SEM image shown in Figure 3.7). The particle agglomeration is not favorable for the diffusion of lithium ions due to the longer pathway for migration and this leads to poor electrochemical performance (not shown here). This demonstrates the advantages of our experiments: in that, the hydrothermal reaction leads to a small and uniform particle size distribution, while the subsequent heat treatment induces high crystallinity and the complete reduction of Fe^{3+} to Fe^{2+}.

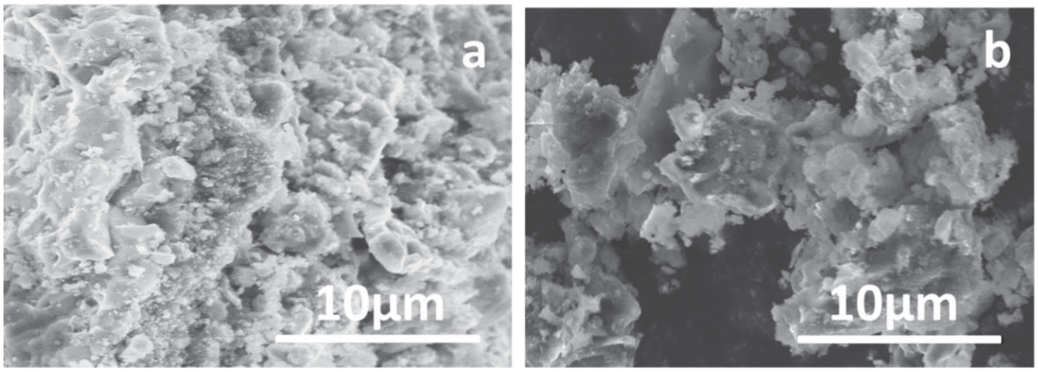

Figure 3.7: *SEM images of LiFePO$_4$/C obtained with commercial nano LiFePO$_4$ prepared by a solid state method at 700 ^{o}C for 3 h (a) and 10 h (b).*

In the above experiments, we used commercial nano Fe_2O_3 as a precursor for the synthesis of $LiFePO_4$. This nano Fe_2O_3 could be replaced with low cost micron sized iron oxide to further simplify large-scale production. Thus, Fe_2O_3 powders (particle size ~ 5 µm, 99% purity) were milled in water with a planetary ball mill to obtain Fe_2O_3 in nanoscale dimensions (~ 200 nm in diameter). This milled Fe_2O_3 was used as the precursor for the preparation of $LiFePO_4$/C under the same conditions as described in Section 3.2a. Figure 3.8a shows the SEM images of the milled Fe_2O_3. It has a particle size of ca. 200 nm and uniform size distribution. Figure 3.8b shows the morphology of $LiFePO_4$/C prepared with the milled Fe_2O_3, which is similar to that shown in Figure 3.3d using the commercial nano Fe_2O_3. As shown in Figure 3.8c, the specific discharge capacity of the as-prepared $LiFePO_4$/C is ~140 mAh g^{-1} which is much improved compared to that synthesized by the solid state method and similar in performance to that synthesized with the nano-Fe_2O_3 precursor. The results demonstrate that our method can be used as a low cost method for implementation into a large-scale production method for $LiFePO_4/C$ and eventual application within lithium-ion batteries. Another important aspect of our procedure is that we have eliminated the need to add additional lithium salts during hydrothermal synthesis. Traditional hydrothermal techniques use an excess of lithium salt (~3x) in their procedures and this significantly increases the costs for large-scale syntheses due to waste water treatment and precursor salt selection.

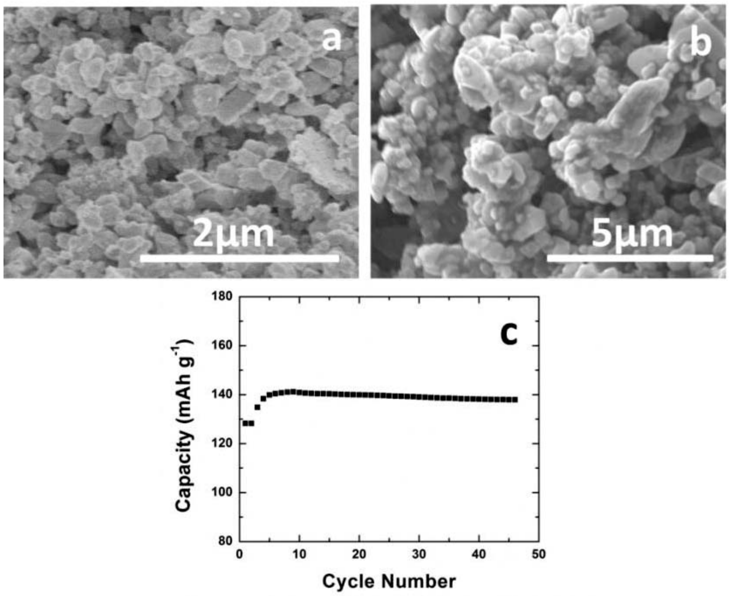

Figure 3.8: *(a) SEM image of commercial Fe_2O_3 precursor after planetary milling treatment. SEM image (b) and battery performance (c) of $LiFePO_4/C$ synthesized with a hydrothermal method followed by post heat treatment at 700 ^oC using (a) as a precursor.*

3.4 Conclusions

$LiFePO_4$/C composite materials have been synthesized with nano-Fe_2O_3 as a precursor using a modified hydrothermal method. Our two-step method combined the advantages of both hydrothermal and solid state methods. In the first step, a $LiFePO_4(OH)$ precursor with small particle size and uniform size distribution was prepared by a hydrothermal method. The heat treatment in the second step leads to the simultaneous realization of carbon coating and $LiFePO_4(OH)$ reduction, producing $LiFePO_4$/C with high purity, crystallinity, specific discharge capacity and cycle stability compared to samples synthesized with the same precursors using a solid state method. Whether commercial nano Fe_2O_3 or a milled micron sized Fe_2O_3 was used as a precursor, the final $LiFePO_4$/C product exhibited excellent battery performance. Our modified hydrothermal method combined with less expensive Fe_2O_3 precursors can greatly reduce synthetic costs for $LiFePO_4$ and it is thus very promising for the large scale synthesis of $LiFePO_4$/C cathode materials for lithium-ion batteries.

Acknowledgements

The authors thank NSERC and Clariant (Canada) Inc. (former Phostech Lithium Inc.) for funding this work under the auspices of the Industrial Research Chair program.

3.5 References

[1] A. K. Padhi, K. S. Nanjundaswamy, J. B. Goodenough, J. Electrochem. Soc. 144 (1997) 1188.

[2] A. K. Padhi, K. S. Nanjundaswamy, C. Masquelier, S. Okada, J. B. Goodenough, J. Electrochem. Soc. 144 (1997) 1609.

[3] J. M. Tarascon, M. Armand, Nature 414 (2001) 359.

[4] M. S. Whittingham, Chem. Rev. 104 (2004) 4271.

[5] M. S. Islam, D. J. Driscoll, C. A. J. Fisher, P. R. Slater, Chem. Mater. 17 (2005) 5085.

[6] D. Morgan, A. Van der Ven, G. Ceder, Electrochem. Solid-State Lett. 7 (2004) A30.

[7] C. W. Kim, J. S. Park, K. S. Lee, J. Power Sources 163 (2006) 144.

[8] S.-Y. Chung, J. T. Bloking,Y.-M. Chiang, Nat. Mater. 1 (2002) 123.

[9] Y.-D. Cho, G. T.-K. Fey, H.-M. Kao, J. Power Sources 189 (2009) 256.

[10] N. Ravet, J. B. Goodenough, S. Besner, M. Simoneau, P. Hovington, M. Armand, In The 196th Meeting of the Electrochemical Society, Honolulu, HI, October 17-22 (1999).

[11] J. D. Wilcox, M. M. Doeff, M. Marcinek, R. Kostecki, J. Electrochem. Soc. 154 (2007) A389.

[12] A. Vu, A. Stein, Chem. Mater. 23 (2011) 3237.

[13] M. M. Doeff, J. D. Wilcox, R. Kostecki, G. Lau, J. Power Sources 163 (2006) 180.

[14] M. Gaberscek, R. Dominko, J. Jamnik, Electrochem. Commun. 9 (2007) 2778.

[15] Y. Wang, Y. Wang, E. Hosono, K. Wang, H. Zhou, Angew. Chem. Int. Ed. 47 (2008) 7461.

[16] B. Kang, G. Ceder, Nature 458 (2009) 190.

[17] A. Yamada, S. C. Chung, K. Hinokuma, J. Electrochem. Soc. 148 (2001) A224.

[18] J. J. Chen, M. S. Whittingham, Electrochem. Commun. 8 (2006) 855.

[19] S. Yang, P. Y. Zavalij, M. Stanley Whittingham, Electrochem. Commun. 3 (2001) 505.

[20] B. Ellis, W. H. Kan, W. R. M. Makahnouk, L. F. Nazar, J. Mater. Chem. 17 (2007) 3248.

[21] J. Qian, M. Zhou, Y. Cao, X. Ai, H. Yang, J. Phys. Chem. C 114 3477.

[22] Z. Lu, H. Chen, R. Robert, B. Y. X. Zhu, J. Deng, L. Wu, C. Y. Chung, C. P. Grey, Chem. Mater. 23 (2011) 2848.

[23] N. J. Yun, H.-W. Ha, K. H. Jeong, H.-Y. Park, K. Kim, J. Power Sources 160 (2006) 1361.

[24] H. Yang, X.-L. Wu, M.-H. Cao,Y.-G. Guo, J. Phys. Chem. C 113 (2009) 3345.

[25] J. Li, C. Daniel, D. Wood, J. Power Sources 196 (2011) 2452.

[26] J. Li, B. L. Armstrong, J. Kiggans, C. Daniel, D. L. Wood, Langmuir 28 (2012) 3783.

[27] J. Orlenius, O. Lyckfeldt, K. A. Kasvayee, P. Johander, J. Power Sources 213 (2012) 119.

[28] N. Marx, L. Croguennec, D. Carlier, A. Wattiaux, F. L. Cras, E. Suard, C. Delmas, Dalton Trans. 39 (2010) 5108.

[29] Y. K. K. E. A. Genkina, B.A. Maksimov, O.K. Mel’Nikov, Kristallografiya 29 (1984) 50.

[30] K.-F. Hsu, S.-Y. Tsay, B.-J. Hwang, J. Mater. Chem. 14 (2004) 2690.

[31] L. Cheng, Z. Zhang, W. Niu, G. Xu,L. Zhu, J. Power Sources 182 (2008) 91.

[32] Z. Zhang, J. Ge, L. Ma, J. Liao, T. Lu, W. Xing, Fuel Cells 9 (2009) 114.

[33] G. Arnold, J. Garche, R. Hemmer, S. Ströbele, C. Vogler, M. Wohlfahrt-Mehrens, J. Power Sources 119–121 (2003) 247.

[34] K. S. Park, J. T. Son, H. T. Chung, S. J. Kim, C. H. Lee, K. T. Kang, H. G. Kim, Solid State Commun. 129 (2004) 311.

[35] J. Popovic, R. Demir-Cakan, J. Tornow, M. Morcrette, D. S. Su, R. Schlögl, M. Antonietti, M.-M. Titirici, Small 7 (2011) 1127.

[36] L. Wang, G. C. Liang, X. Q. Ou, X. K. Zhi, J. P. Zhang, J. Y. Cui, J. Power Sources 189 (2009) 423.

[37] X.-L. Wu, L.-Y. Jiang, F.-F. Cao, Y.-G. Guo, L.-J. Wan, Adv. Mater. 21 (2009) 2710.

[38] R. Dominko, M. Bele, M. Gaberscek, M. Remskar, D. Hanzel, J. M. Goupil, S. Pejovnik, J. Jamnik, J. Power Sources 153 (2006) 274.

[39] R. Dominko, J. M. Goupil, M. Bele, M. Gaberscek, M. Remskar, D. Hanzel, J. Jamnik, J. Electrochem. Soc. 152 (2005) A858.

[40] C. Fongy, S. Jouanneau, D. Guyomard, J. C. Badot, B. Lestriez, J. Electrochem. Soc. 157 (2010) A1347.

[41] J. Li, B. L. Armstrong, J. Kiggans, C. Daniel, D. L. Wood, J. Electrochem. Soc. 160 (2013) A201.

[42] S.-H. Wu, K.-M. Hsiao,W.-R. Liu, J. Power Sources 146 (2005) 550.

[43] X. Zhi, G. Liang, L. Wang, X. Ou, J. Zhang, J. Cui, J. Power Sources 189 (2009) 779.

[44] H. Liu, P. Zhang, G. C. Li, Q. Wu,Y. P. Wu, J. Solid State Electrochem. 12 (2008) 1011.

[45] C. W. Kim, M. H. Lee, W. T. Jeong, K. S. Lee, J. Power Sources 146 (2005) 534.

[46] H.-p. Liu, Z.-x. Wang, X.-h. Li, H.-j. Guo, W.-j. Peng, Y.-h. Zhang, Q.-y. Hu, J. Power Sources 184 (2008) 469.

Chapter 4 One Step Hydrothermal Synthesis of $LiFePO_4$ with Nano Fe_2O_3

Lifeng Cheng[a], Guoxian Liang[b], Dean D. MacNeil[a*]

[a] Département de Chimie, Université de Montréal, Montréal, Québec H3T 1J4, Canada

[b] Clariant (Canada) Inc., 1475 Rue Marie-Victorin, St-Bruno, Québec J3V 6B7, Canada

Chapter 4 consists of an article submitted to the Journal of Materials Chemistry A. The article was prepared by the author under the supervision of Dr. MacNeil and Guoxian Liang.

Abstract

In this work, $LiFePO_4$ *has been synthesized, in one step, with nanosized* Fe_2O_3 *by a hydrothermal method. As a preliminary study, commercial nanosized* Fe_2O_3 *was explored as a* Fe^{3+} *precursor, while ascorbic acid and* H_3PO_3 *were used as co-reducing agents. The dual reducing agents within a sealed high pressure condition provided adequate reducing and crystallization conditions to obtain pure* $LiFePO_4$ *with good crystallinity. This work is promising in reducing the synthetic cost of* $LiFePO_4$ *prepared through a low temperature route, by using inexpensive precursors and reducing agents. An in situ product transformation mechanism during the*

hydrothermal reaction is proposed based on an analysis of both XRD and SEM measurements.

4.1 Introduction

The demand for sustainable and clean energy is booming, but without energy storage, renewable electricity generation (wind, wave, solar) will be much less viable. This has led to the research and development of more efficient and less expensive high energy batteries, in particular lithium-ion batteries [1,2]. For lithium-ion batteries, the proper choice of cathode material is crucial to the improvement of the lithium ion battery.

In the past, numerous attempts to replace the traditional $LiCoO_2$ cathode material have been suggested, because $LiCoO_2$ is expensive and has thermal stability issues [1,3]. Among the alternatives, $LiFePO_4$, with an ordered olivine structure [4-6], has been identified as promising due to its low toxicity, low cost, and high thermal/chemical stability in the fully charged state. Moreover, it shows a very flat voltage curve with a plateau near 3.5 V versus Li/Li^+ and has a high theoretical capacity of 170 mAh g^{-1}. However, the main obstacle in reaching the theoretical performance limits of $LiFePO_4$ is its very low electronic conductivity [7-10] and the difficulty in synthesizing single-phase $LiFePO_4$ because of the facile oxidation of Fe^{2+} to Fe^{3+}. Various synthetic methods such as a solid-state [4], mechanochemical activation [11], sol–gel [12], hydrothermal [13], molten salt [14] and microwave heating [15] synthetic methods have been successfully used to solve these problems. Unfortunately, the costs of the chosen procedures are high, since either expensive starting materials are used or the process is tedious and hard to control. This high synthetic cost hinders large scale deployment of $LiFePO_4$ as a commercial cathode material. Although low cost Fe^{3+} precursor compounds have been used to reduce the synthetic cost in the past, reducing agents such as polyethylene glycol and LiI must be added in excess, which increases the processing cost [16, 17]. Alternatively, carbothermal reduction (CTR) is a simple and inexpensive method to obtain $LiFePO_4$ from a Fe^{3+} source (Fe_2O_3) with LiH_2PO_4 and carbon. However, it is unavoidable that long dwell times at high firing temperature is required in the carbothermal reduction method, which consumes high energy, and thus leads to an undesirable elevated synthetic cost.

Obviously, in order to reduce the production cost of $LiFePO_{4,}$ it is necessary to develop a low temperature synthetic method utilizing inexpensive iron precursors in place of divalent iron compounds. A hydrothermal synthetic method [18-22] is a simple and low energy consumption process compared to solid state reactions, which require high firing temperature. Fe_2O_3 is a readily available and an inexpensive source of Fe^{3+}. Recently, nano-Fe_2O_3 has been synthesized from inexpensive Fe^{3+} soluble precursors and inorganic additives using a hydrothermal method [23-25].

In this work, $LiFePO_4$ has been prepared by a hydrothermal method using nano Fe_2O_3 as a precursor. As a preliminary study, commercial nano Fe_2O_3 was explored as a possible Fe precursor, while ascorbic acid and H_3PO_3 were used as co-reducing agents. For the first time, pure $LiFePO_4$ has been synthesized from Fe_2O_3 using a hydrothermal method. This work is promising in reducing the synthetic cost of $LiFePO_4$ by using a low temperature route with inexpensive precursors and reducing agents.

4.2 Experimental

4.2.1 Preparation of $LiFePO_4$ using a hydrothermal method

a) Synthesis of $LiFePO_4$ with ascorbic acid as a reducing agent.

LiH_2PO_4, Fe_2O_3 (25-30 nm, Sigma-Aldrich Co. LLC), ascorbic acid with a mole ratio of 1:0.5:0.5 and 30 mL of water were sealed in a 40 mL Teflon-lined stainless steel autoclave. The autoclave was then maintained at 230 °C for 48 h. Herein, the ascorbic acid served as a reducing agent. After cooling the autoclave naturally to room temperature, the product was isolated by evaporating the solution at 80 °C. In a comparative hydrothermal test, carbon black was used in place of ascorbic acid to see if carbon can function as a reducing agent under hydrothermal conditions.

b) Synthesis of $LiFePO_4$ with the combination of ascorbic acid and H_3PO_3 as reducing agents

The procedure followed that of section (a), except that LiOH, H_3PO_3, H_3PO_4, Fe_2O_3 (25-30 nm) and ascorbic acid were introduced into the vessel at a mole ratio of

1:0.5:0.5:0.5:0.5. Ascorbic acid and H_3PO_3 served as co-reducing agents within this reaction scheme. To further study the reaction mechanism, we carried out the hydrothermal reactions at 230 °C for various time intervals (3, 9, 12, 36 and 48 hours). To clarify the function of each reducing agent, the reaction was also duplicated while eliminating ascorbic acid from the reaction mixture.

4.2.2 Physicochemical characterizations

X-ray diffraction (XRD) was performed using a Bruker D8 X-ray Advance diffractometer equipped with Cu Kα as radiation source. The particle size and morphology of samples were examined by a Scanning Electron Microscope (Hitachi S-4300 microscope). X-ray photoelectron spectroscopy (XPS) was performed with a Scanning Auger Multi Probe PHI Spectrometer (Model 25-120) equipped with Al source operating at 250 W. The signals were filtered using a hemispherical analyzer (pass energy = 100 eV for survey spectra and 25 eV for fine spectra). The C(1s) photoelectron line at 284.6 eV was used as an internal standard for the correction of the charging effect in all samples.

4.3 Results and discussion

In order to use Fe(III) materials as precursors for $LiFePO_4$, reducing agents are required. Ascorbic acid has been found to be an effective option in preventing the undesirable oxidation of Fe(II) species during hydrothermal treatments [18,26,27]. In this work, ascorbic acid is employed to reduce Fe(III) to Fe(II). Figure 4.1a shows the XRD pattern of product using ascorbic acid as a reducing agent. The main phase of the product can be identified as $LiFePO_4$ with an ordered orthorhombic crystal structure (JCPDS # 40-11499, space group: pnma), while minor peaks from impurity phase(s) are identified with an asterisk. The majority of the impurity is due to the presence of Li_3PO_4 and $Fe_3(PO_4)_2(OH)_3$ within the sample. This indicates that there is still some residual Fe(III) in the final product after 48 hours of reaction. The hydrothermal process provides a condition of high-pressure, which leads to the decomposition of ascorbic acid and the formation of a reductive atmosphere such as CO, H_2 and/or other organics of strong reducing power. To clarify the role of ascorbic acid in the reduction of Fe(III) to Fe(II), we replaced ascorbic acid with carbon black during the hydrothermal reaction. The product of the reaction exhibits a poor XRD pattern as seen from Figure 4.1b, indicating that the formation/crystallization of $LiFePO_4$ has not occurred. This confirms that the reductive atmosphere from the decomposition of ascorbic acid is required to reduce Fe(III) to Fe(II) within these conditions. This phenomenon has also been reported by Ravet et al [28] during their study on the mechanism of $LiFePO_4$ synthesis. They found that the reductive atmosphere created by the pyrolysis of a polymer rather than the presence of carbon powder reduces Fe(III) to Fe(II) at high temperature. A similar procedure, likely occurs under these hydrothermal conditions. Unfortunately, impurities are still present within our sample (Figure 4.1a) even though numerous permutations of ascorbic acid concentration, temperatures and reaction times were investigated.

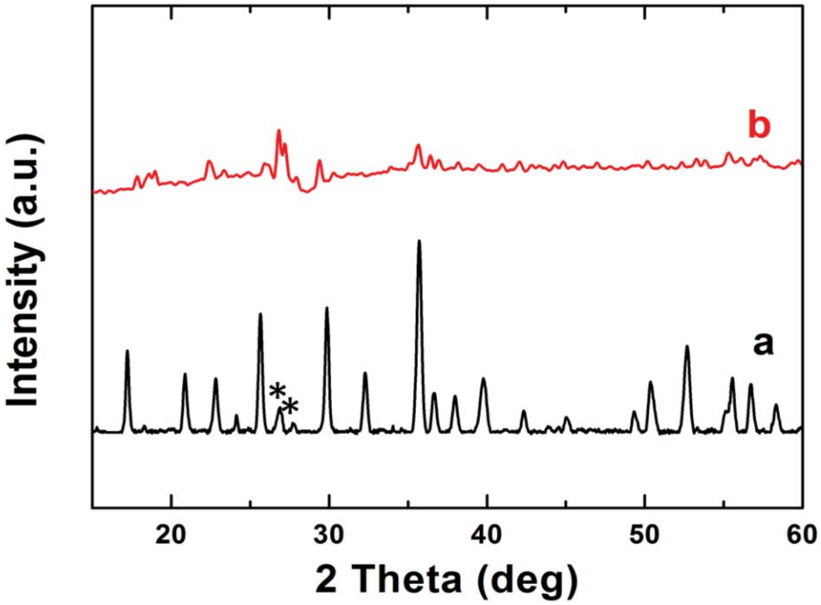

Figure 4.1: *XRD patterns of $LiFePO_4$ prepared with ascorbic acid (a) or carbon (b) as reducing agents.*

H_3PO_3 is a reducing agent that has been used for the preparation of nanomaterials in the past [29,30]. Figure 4.2a displays the XRD pattern of the product prepared using H_3PO_3 as a reducing agent. Obviously, the product is a mixture of $LiFePO_4(OH)$ and $LiFePO_4$. This indicates that H_3PO_3 is a weak reducing agent and cannot completely reduce Fe(III) to Fe(II) in this reaction mixture. Figure 4.2b is identical to Figure 4.1a where ascorbic acid is used as a reducing agent in the reaction mixture. Due to the incomplete reduction when either ascorbic acid or H_3PO_3 is used independently as a reducing agent, we explored the feasibility of combining both reducing agents in the same reaction mixture. Under the same synthetic conditions as used previously, there is no indication of impurities within the sample (see Figure 4.2c). This signifies that Fe(III), for the first time has been completely reduced to Fe(II) to produce

$LiFePO_4$ at low temperature using both ascorbic acid and H_3PO_3. An amorphous Fe(III) impurity could be present in the product mixture, but this is unlikely as the precursor is a highly crystalline Fe_2O_3 material, further study by Mossbauer spectroscopy would be required to clearly indicate that all products (amorphous or crystalline) are in the Fe(II) state. H_3PO_3 likely changes the pH value of the reaction mixture, aiding the reduction and removal of the impurities. Thus, our low temperature hydrothermal method with dual reductants can provide a good reducing atmosphere and crystallization environment to obtain pure $LiFePO_4$ with good crystallinity, as shown in Figure 4.2c.

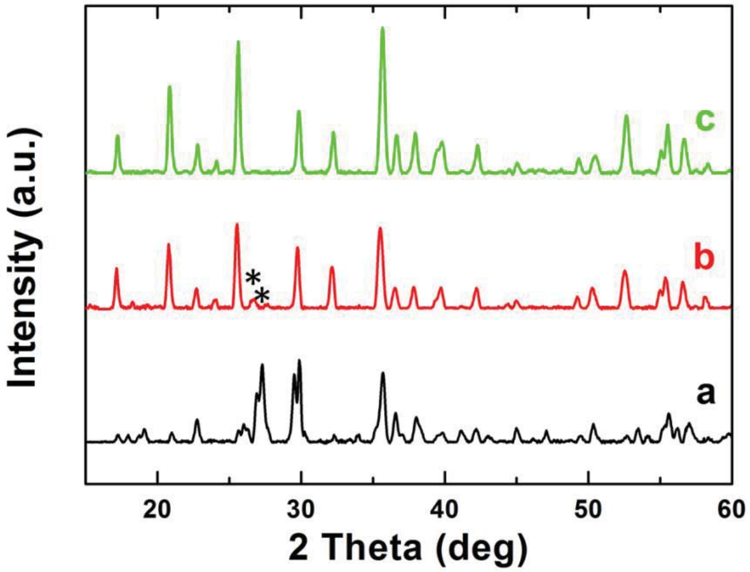

Figure 4.2: *XRD patterns of $LiFePO_4$ prepared with H_3PO_3 (a), ascorbic acid (b), and a mixture (1:1 in molar ratio) of H_3PO_3 and ascorbic acid (c).*

An XPS analysis [31, 32] was used to investigate the chemical compositions and valence states of the as-synthesized $LiFePO_4$/C material [33, 34]. As shown in the

XPS survey spectrum of Figure 4.3a, the sample consists of Fe, P, O, C and Li elements. The Li(1s) spectrum overlaps with the Fe(3p) spectrum as seen from the insert in Figure 4.3a, which is consistent with that reported by Rho et al [34]. As shown in Figure 4.3b and 4.3c, both O(1s) and P(2p) have a symmetrical shape and well-defined features. Their XPS peaks, located at 530.1 eV and 130.7 eV, respectively, are due to the phosphate moiety in $LiFePO_4$. The Fe(2p) spectrum (Figure 4.3d) shows a doublet at 724.0 eV for Fe(2p1/2) and at 710.9 eV for Fe(2p3/2), which is typical of Fe in a (II) oxidation state. There was no indication of any Fe(III) residuals on the surface of this sample. The results of both XRD and XPS analyses confirm the high purity of the $LiFePO_4$.

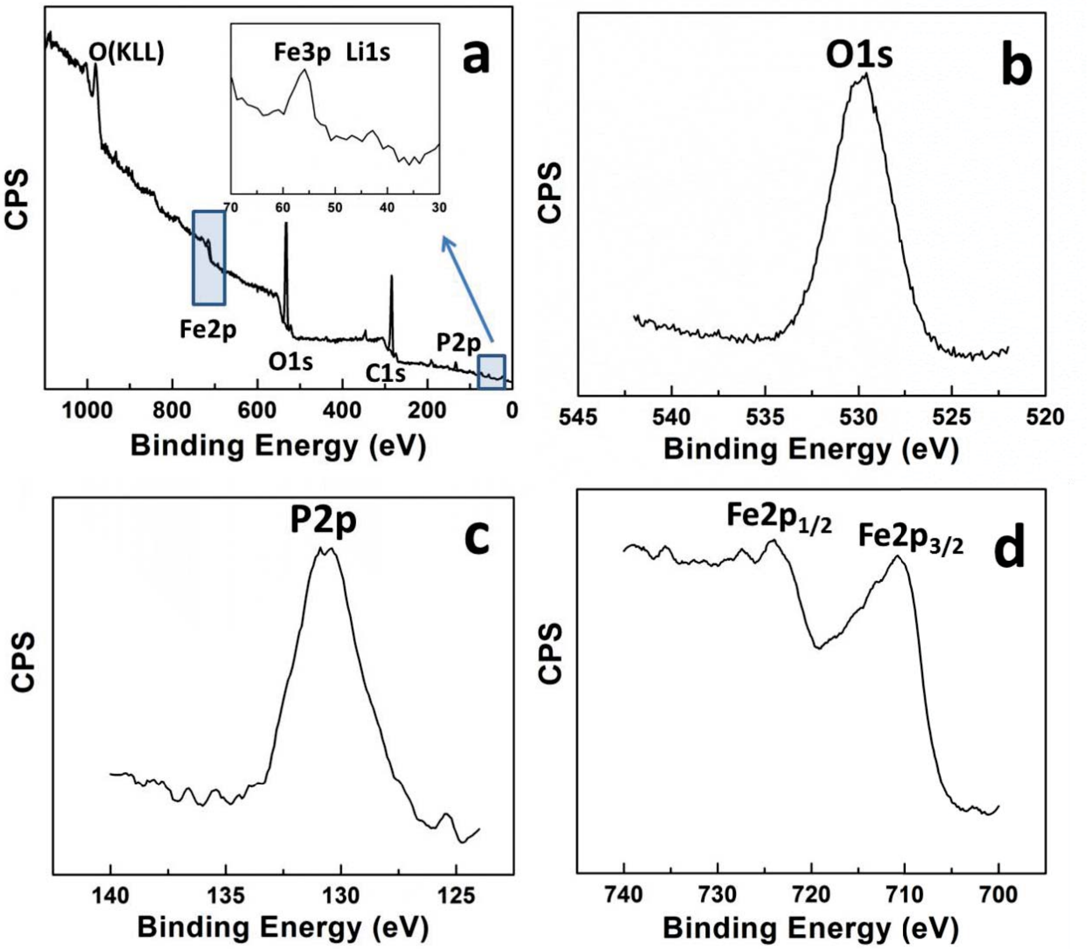

Figure 4.3: *XPS spectra of the as-prepared $LiFePO_4$ prepared under hydrothermal condition at 230^oC for 48 h. (a) survey spectrum. The insert is the expanded view of the Fe(3p) and Li(1s) in survey spectrum. (b) O(1s) fine spectrum; (c) P(2p) fine spectrum; (d) Fe(2p) fine spectrum.*

To further our understanding into the formation process of $LiFePO_4$ using our procedure, a number of carefully conducted time-dependent experiments were performed. Figure 4.4 shows the XRD patterns of the product of these reactions after

3, 6, 9, 12, 36 and 48 hours respectively at 230 °C. Surprisingly after only 3 hours, the main phase of the product can be indexed to $LiFePO_4$. Unfortunately, this sample contains the presence of impurity peaks that are attributed to Li_3PO_4 and $Fe_3(PO_4)_2(OH)_3$ and the crystallinity of the product is low since the sintering time is short. While increasing the reaction time from 6 h to 36 h, the peaks from the impurity become gradually weaker, and the crystallinity and purity of $LiFePO_4$ is greatly improved. The phase pure $LiFePO_4$ product is obtained after 48 hours of reaction at 230 °C.

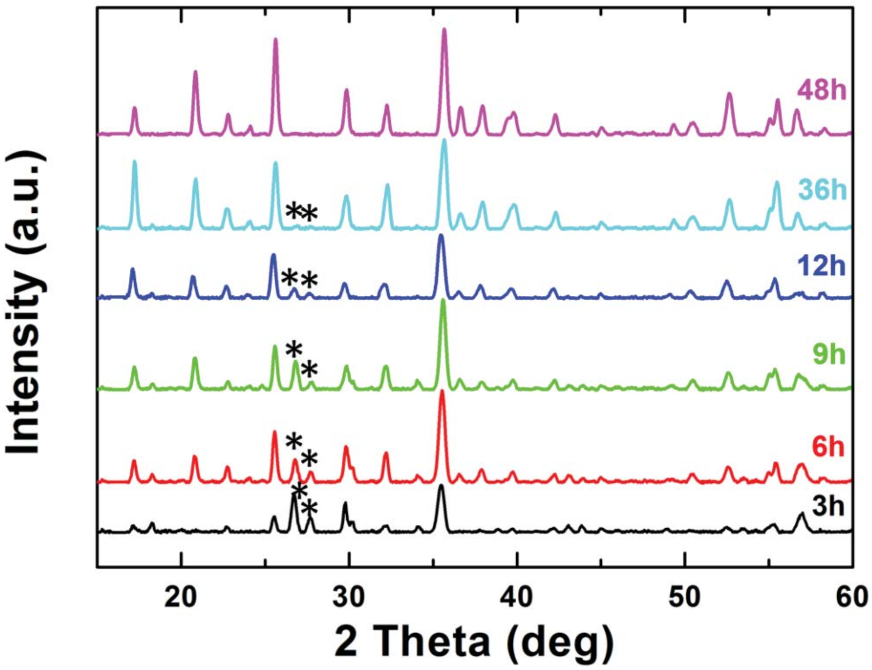

Figure 4.4: *XRD patterns of $LiFePO_4$ prepared using different hydrothermal reaction time using mixture of H_3PO_3 and ascorbic acid (1:1 in molar ratio).*

Figure 4.5 shows a series of SEM micrographs depicting the typical morphologies of the precursor and final product. Figure 4.5a shows an SEM image of the Fe(III) precursor, which is a commercial 25-30 nm of nano Fe_2O_3 material that is aggregated into 10-20 μm particles. A solid Fe_2O_3 precursor was chosen rather than a soluble Fe(III) precursors because soluble precursors tend to require extra Li salts (normally three times the stoichiometric ratio of Li salt is required), which increase the synthetic cost and also the extra soluble Li salt within the solution needs to be treated before disposal, increasing production cost [35,36]. Nano Fe_2O_3 can be easily synthesized from inexpensive soluble Fe(III) precursors and inorganic additives within a hydrothermal method [23-25]. Herein, we used commercial nano Fe_2O_3, but it is likely that other Fe_2O_3 materials could be used to synthesize $LiFePO_4$, although a careful balance between particle size and reaction time would be required.

After 3h within the hydrothermal reaction, the primary particles of the product grow to 2-3 μm in dimension and are uniformly dispersed (Figure 4.5b). However, after 12 h, the microparticles evolve into microrods, with an irregular shape and size disparity (Figure 4.5c). These microrods continue to grow after 24 h (Figure 4.5d) and 36 h (Figure 4.5e), and finally the agglomerated pure $LiFePO_4$ is prepared after 48 h (Figure 4.5f).

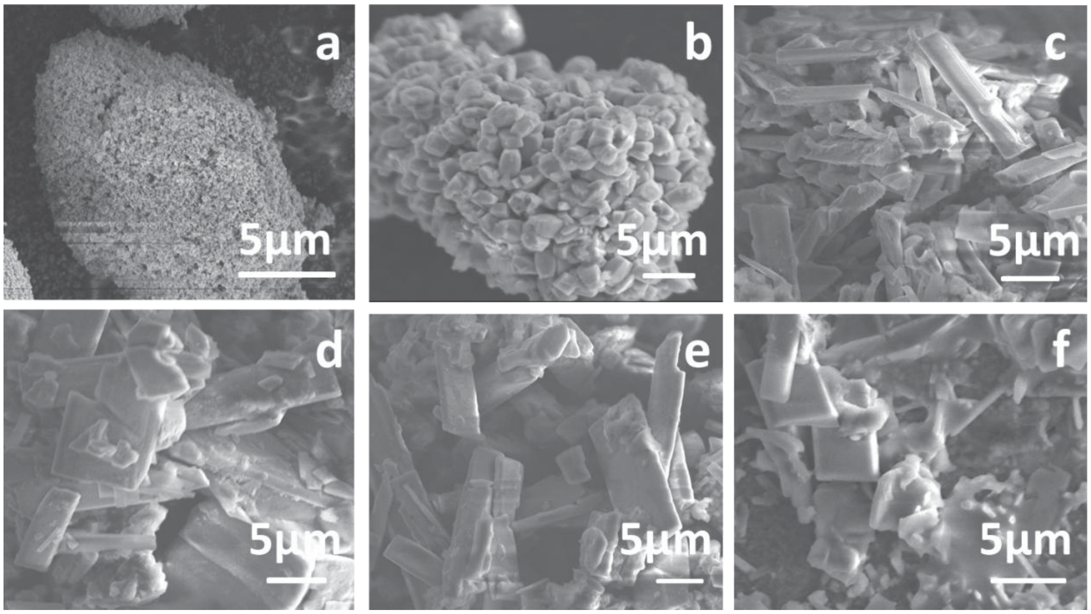

Figure 4.5: *SEM of the nano Fe_2O_3 precursor (a) and the as-prepared $LiFePO_4$ using different hydrothermal reaction times (b: 3 h; c: 12 h; d: 24 h; e: 36 h; f: 48 h) of Figure 4.4.*

There are three well-known mechanisms for crystal formation and particle growth during hydrothermal conditions. They include either precipitation from a supersaturated solution, an in situ product transformation or a dissolution-precipitation mechanism [37-39]. In the present work, based on the SEM morphological observations shown in Figure 4.5 and the phase transformation seen in the XRD analysis (Figure 4.4), we assume an in situ product transformation mechanism accounts for the formation of our hydrothermal $LiFePO_4$ product (Figure 4.6). Thus, the nano Fe_2O_3 precursors provide an initial nucleation site over which dissolved precursors diffuse around and react with it to produce $LiFePO_4$ (product) over the span of 48 hours. In contrast to the dissolution-precipitation mechanism, an in situ transformation mechanism normally requires much longer reaction times due to ions slowly diffusing through the insoluble solid compound [40,41]. In our case, the ions diffuse through the insoluble solid cores (Fe_2O_3) quickly due to the nano size of Fe_2O_3 and the high pressure conditions. Thus, an observable amount of $LiFePO_4$ (product) were produced after 3h (Figure 4.6), While the impurities (Li_3PO_4 and $Fe_3(PO4)_2(OH)_3$) likely exist in the center of the particles and cannot transform to $LiFePO_4$ rapidly probably due to the inadequate contact to the reductive atmosphere and the growing particle size of product during reaction. In the conventional $LiFePO_4$ synthesis process using soluble iron precursors, $Fe_3(PO4)_2{\cdot}XH_2O$ and Li_3PO_4 are formed as intermediate phases, in which case the overall reaction was faster probably due to the small size of those intermediate phases. In the present case, the $Fe_3(PO4)_2(OH)_3$ and Li_3PO_3 are already agglomerated within large micron sized particles resulting in elevated reaction times.

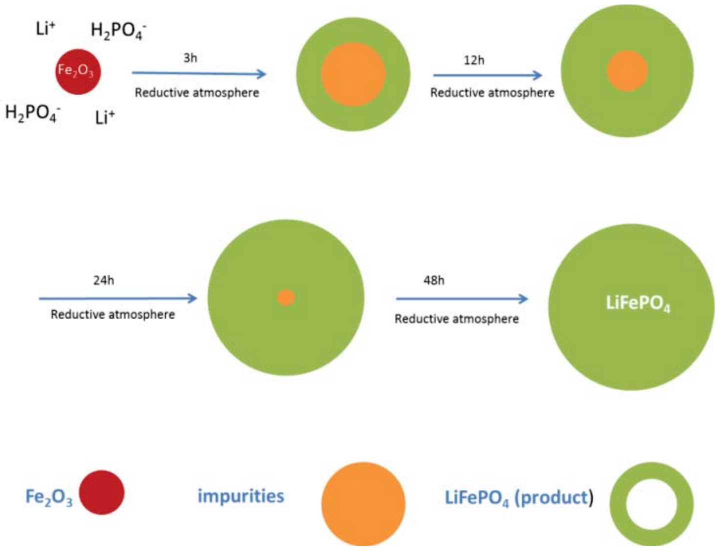

Figure 4.6: *Schematic illustration of an in-situ product transformation mechanism of the formation of the pure* $LiFePO_4$ *product.*

4.4 Conclusions

In this work, pure $LiFePO_4$ has been synthesized with nano Fe_2O_3 by a hydrothermal method in one step. As a preliminary study, commercial nano Fe_2O_3 is explored as a possible Fe(III) precursor, while ascorbic acid and H_3PO_3 were used as co-reducing agents. The main reducing agent is ascorbic acid, which produces CO or H_2 in the atmosphere that reduces most of Fe(III) to Fe(II) The H_3PO_3 was used as a co-reducing agent and it may change the pH value of reaction environment. Our hydrothermal method is a low temperature synthetic route providing a good reducing atmosphere and crystallization environment to obtain pure $LiFePO_4$ with good crystallinity. An in-situ product transformation mechanism during the hydrothermal reaction was proposed based on the XRD and SEM measurements. Although the particle size of as-prepared $LiFePO_4$ is large, our work is promising in preparing pure $LiFePO_4$ from nano Fe_2O_3 at low temperature using a combination of proper precursors and reducing agents.

Acknowledgements

The authors thank NSERC and Clariant (Canada) Inc. (former Phostech Lithium Inc.) for funding this work under the auspices of the Industrial Research Chair program.

4.5 References

1. Tarascon, J. M.; Armand, M. *Nature* **2001**, 414, 359.
2. Yuan, L.-X.; Wang, Z.-H.; Zhang, W.-X.; Hu, X.-L.; Chen, J.-T.; Huang, Y.-H.; Goodenough, J. B. *Energy Environ. Sci.* **2011**, 4, 269.
3. Ohzuku, T.; Brodd, R. J. *J. Power Sources* **2007**, 174, 449.
4. Padhi, A. K.; Nanjundaswamy, K. S.; Goodenough, J. B. *J. Electrochem. Soc.* **1997**, 144, 1188.
5. Padhi, A. K.; Nanjundaswamy, K. S.; Masquelier, C.; Okada, S.; Goodenough, J. B. *J. Electrochem. Soc.* **1997**, 144, 1609.
6. Whittingham, M. S. *Chem. Rev.* **2004**, 104, 4271.
7. Islam, M. S.; Driscoll, D. J.; Fisher, C. A. J.; Slater, P. R. *Chem. Mater.* **2005**, 17, 5085.
8. Morgan, D.; Van der Ven, A.; Ceder, G. *Electrochem. Solid-State Lett.* **2004**, 7, A30.
9. Kim, C. W.; Park, J. S.; Lee, K. S. *J. Power Sources* **2006**, 163, 144.
10. Chung, S.-Y.; Bloking, J. T.; Chiang, Y.-M. *Nat. Mater.* **2002**, 1, 123.
11. Franger, S.; Benoit, C.; Bourbon, C.; Le Cras, F. *J. Phys. Chem. Solids* **2006**, 67, 1338.
12. Yang, J. S.; Xu, J. J. *Electrochem. Solid-State Lett.* **2004**, 7, A515.
13. Recham, N.; Armand, M.; Chotard, J.-N.; Barpanda, P.; Walker, W.; Dupont, L. *Chem. Mater.* **2009**, 22, 724.

14. Chen, Z.-y.; Zhu, W.; Zhu, H.-l.; Zhang, J.-l.; Li, Q.-f. *Trans. Nonferr. Met. Soc. Chin.* **2010**, 20, 809.
15. Guo, X.; Zhang, Y.; Zhan, H.; Zhou, Y. *Solid State Ion.* **2010**, 181, 1757.
16. Yang, H.; Wu, X.-L.; Cao, M.-H.; Guo, Y.-G. *J. Phys. Chem. C* **2009**, 113, 3345.
17. Wang, L. N.; Zhang, Z. G.; Zhang, K. L. *J. Power Sources* **2007**, 167, 200.
18. Chen, J. J.; Whittingham, M. S. *Electrochem. Commun.* **2006**, 8, 855.
19. Yang, S.; Zavalij, P. Y.; Stanley Whittingham, M. *Electrochem. Commun.* **2001**, 3, 505.
20. Ellis, B.; Kan, W. H.; Makahnouk, W. R. M.; Nazar, L. F. *J. Mater. Chem.* **2007**, 17, 3248.
21. Qian, J.; Zhou, M.; Cao, Y.; Ai, X.; Yang, H. *J. Phys. Chem. C* **2010**, 114, 3477.
22. Lu, Z.; Chen, H.; Robert, R.; Zhu, B. Y. X.; Deng, J.; Wu, L.; Chung, C. Y.; Grey, C. P. *Chem. Mater.* **2011**, 23, 2848.
23. Hu, X.; Yu, J. C. *Adv. Funct. Mater.* **2008**, 18, 880.
24. Wu, C.; Yin, P.; Zhu, X.; OuYang, C.; Xie, Y. *J. Phys. Chem. B* **2006**, 110, 17806.
25. Wu, X. L.; Guo, Y. G.; Wan, L. J.; Hu, C. W. *J. Phys. Chem. C* **2008**, 112, 16824.
26. Xia, Y.; Zhang, W.; Huang, H.; Gan, Y.; Tian, J.; Tao, X. *J. Power Sources* **2011**, 196, 5651.
27. Uchiyama, H.; Imai, H. *Cryst. Growth Des.* **2010**, 10, 1777.
28. Ravet, N.; Gauthier, M.; Zaghib, K.; Goodenough; Mauger, A.; Gendron, F.; Julien *Chem. Mater.* **2007**, 19, 2595.

29. Antonio Lopez-Sanchez, J.; Bartley, J. K.; Wells, R. P. K.; Rhodes, C.; Hutchings, G. J. *New J. Chem.* **2002**, 26, 1613.
30. Niida, H.; Takahashi, M.; Uchino, T.; Yoko, T. *J. Mater. Res.* **2003**, 18, 1.
31. Zhang, Z.; Ge, J.; Ma, L.; Liao, J.; Lu, T.; Xing, W. *Fuel Cells* **2009**, 9, 114.
32. Zhang, Z.; Désilets, F.; Felice, V.; Mecheri, B.; Licoccia, S.; Tavares, A. C. *J. Power Sources* **2011**, 196, 9176.
33. Liu, H.; Tang, D. *Solid State Ion.* **2008**, 179, 1897.
34. Rho, Y.-H.; Nazar, L. F.; Perry, L.; Ryan, D. *J. Electrochem. Soc.* **2007**, 154, A283.
35. Chen, J.; Bai, J.; Chen, H.; Graetz, J. *J. Phys. Chem. Lett.* **2011**, 1874.
36. Chen, J. J.; Vacchio, M. J.; Wang, S. J.; Chernova, N.; Zavalij, P. Y.; Whittingham, M. S. *Solid State Ionics* **2008**, 178, 1676.
37. Qin, X.; Wang, X.; Xiang, H.; Xie, J.; Li, J.; Zhou, Y. *J. Phys. Chem. C* **2010**, 114, 16806.
38. Zhang, L.; Chen, D.; Jiao, X. *J. Phys. Chem. B* **2006**, 110, 2668.
39. Xu, Z. P.; Lu, G. Q. *Chem. Mater.* **2005**, 17, 1055.
40. Hertl, W. *J. Am. Ceram. Soc.* **1988**, 71, 879.
41. Eckert, J. O.; Hung-Houston, C. C.; Gersten, B. L.; Lencka, M. M.; Riman, R. E. *J. Am. Ceram. Soc.* **1996**, 79, 2929.

Chapter 5 Low Cost Synthesis of $LiMn_{0.7}Fe_{0.3}PO_4$ with Fe_2O_3 and MnO through a Hydrothermal Method

Lifeng Cheng[a], Guoxian Liang[b], Soumia EL Khakani, Dean D. MacNeil[a*]

[a] Département de Chimie, Université de Montréal, Montréal, Québec H3T 1J4, Canada

[b] Clariant (Canada) Inc., 1475 Rue Marie-Victorin, St-Bruno, Québec J3V 6B7, Canada

Chapter 5 consists of an article submitted to the Materials Research Bulletin. The article was prepared by the author under the supervision of Dr. MacNeil and Dr. Guoxian Liang. Soumia EL Khakani, Ph.D student in Dr. MacNeil's lab aided with the electrochemical tests.

Abstract

In this work, $LiFe_{0.3}Mn_{0.7}PO_4$ *has been prepared using a hydrothermal synthetic method. Low cost precursors* Fe_2O_3 *and MnO were used in this hydrothermal synthesis. This work demonstrates that the reduction of* Fe^{3+} *to* Fe^{2+} *at low temperature can be realized through the selection of proper precursors and reducing agents and a pure* $LiMn_{0.7}Fe_{0.3}PO_4$ *material can be obtained. The inferior discharge capacity for the as-prepared* $LiFe_{0.3}Mn_{0.7}PO_4/C$ *may be attributed to the presence of*

a large amount of carbon, lower conductivity of $LiMn_{0.7}Fe_{0.3}PO_4$ *and possible* Mn^{2+} *disorder. Further study is underway to determine the cause of the low capacity.*

5.1 Introduction

Increasing attention has been paid to electric vehicles (EVs) and hybrid electric vehicles (HEVs) in an attempt to relieve the pressure of lower fossil fuel reserves and environmental pollution. Lithium-ion batteries have been highlighted as a desirable advanced system for electrochemical energy storage and conversion [1,2]. Since the pioneering work of Padhi et al. [3], $LiMPO_4$ compounds (M=Fe, Mn, Co, or Ni, theoretical capacity around 170 mAhg_1) have been investigated as promising cathode materials for rechargeable lithium-ion batteries. Among these materials, LiFePO4 has attracted great interest due to its high theoretical capacity (170 mAh g^{-1}), moderate operating voltage (3.45 V vs. Li^+/Li^0), low cost, environmental friendliness and high safety [3]. However, an inherent poor kinetic property, due to the low electronic conductivity for $LiFePO_4$, leads to poor rate capability in electrochemical testing. An attractive alternative to $LiFePO_4$ is $LiMnPO_4$, which provides higher energy density compared with $LiFePO_4$ and is also compatible with current electrolytes used within lithium ion batteries. However, the full utilization of the theoretical energy density of $LiMnPO_4$ is seldom achieved due to poor mass and charge transport effects, hindering Li^+ intercalation/deintercalation kinetics in this electrode material [4,5]. Some researches demonstrated an increase in kinetics when some of the Mn ions were replaced with Fe to form the solid solution

$LiFe_xMn_{1-x}PO_4$ [6-9].

A solid solution of $LiFe_xMn_{1-x}PO_4$ has been studied by a number of research groups [10-16] using numerous synthetic methods such as precipitation, sol-gel, polyol or spray pyrolysis techniques. However, these methods used expensive precursors, and a simple low cost synthetic process is crucial for commercializing any lithium-ion battery material.

Hydrothermal synthetic methods [17-21] are simple and consume lower energy compared to high temperature solid state reactions with long dwell times. Herein, we prepared pure $LiMn_{0.7}Fe_{0.3}PO_4$ with a hydrothermal method using low cost Fe_2O_3 and MnO as a precursor. Initially, $LiMn_{0.7}Fe_{0.3}PO_4$ was prepared with a hydrothermal method followed by milling the product to an average particle size of 100-200 nm. The resulting nano particles were then carbon coated using the thermal decomposition of β-lactose as a carbon source. These milled and carbon coated $LiFe_{0.3}Mn_{0.7}PO_4$ products with dimensions of ~ 100 nm were then tested for electrochemical performance. Although the electrochemical performance requires improvement, low cost precursors and low temperature synthesis conditions will greatly reduce large-scale synthetic cost, favoring the commercialization of $LiMn_{0.7}Fe_{0.3}PO_4$ as a cathode material for lithium-ion battery.

5.2 Experimental

5.2.1 Sample synthesis

Stoichiometric amounts of LiH_2PO_4, Fe_2O_3 (25-30 nm, Sigma-Aldrich Co. LLC), MnO (Sigma-Aldrich Co. LLC) and ascorbic acid with a mole ratio of 1:0.15:0.7:0.25 were milled for 3 h in water by a planetary ball mill (Fritsch). The planetary ball milling was performed using a 250 ml Syalon container with 25 mm zirconia balls. The suspension was then transferred to a 110 ml Teflon-lined stainless steel autoclave. An additional 0.25 mole percent of ascorbic acid was added to the autoclave. After bubbling N_2 for 30 min, the autoclave was sealed and maintained at 230 °C for 24 h.

5.2.2 Sample processing

To obtain improved electrochemical performance, $LiMn_{0.7}Fe_{0.3}PO_4$ synthesized by the hydrothermal method described in section 2.1, was milled in a continuous-flow agitator bead mill (MicroCer by Netszch) using 500 micron ZrO2 milling media to reduce its particle size. The milling was performed for 2 h to obtain a uniform particle size distribution. β-lactose (Fisher) (10 wt% with respect to the active materials) was added into the milling slurry during the last 15 minutes of milling. The samples were collected from the mill and the water was then evaporated from the milling mixture by stirring at 80°C. The materials were subsequently carbon coated by heating at 700 °C for 3 h under nitrogen atmosphere.

5.2.3 Physicochemical characterizations

X-ray diffraction (XRD) was performed using a Bruker D8 X-ray Advance diffractometer equipped with a Cu Kα (λ = 1.5405 Å) radiation source. The particle size and morphology of samples were examined by a Scanning Electron Microscope (Hitachi S-4300 microscope). A Fisons Instruments (SPA, model EA1108) elemental analyzer was used to determine the carbon content in each sample.

5.2.4 Electrochemical measurements

Electrochemical evaluations were performed by combining 80 wt% of the $LiMn_{0.7}Fe_{0.3}PO_4/C$ powder, 10 wt% of conductive carbon (Super-P Li, Timcal) and 10 wt% polyvinylidene difluoride (PVDF, 5% in N-methylpyrroldinone (NMP)) with an excess of NMP to form slurry. The slurry was then deposited on a carbon coated Al foil. After drying at 90 °C overnight, electrode disks were punched and weighed before cell assembly in standard 2032 coin-cell hardware (Hohsen) using a lithium metal foil as both counter and reference electrodes and a Celgard 2200 separator. Cells were assembled in an argon-filled glove box using 1 M $LiPF_6$ in ethylene carbonate (EC) / diethyl carbonate (DEC) (2:1 by volume) as an electrolyte (UBE). Battery performance evaluations were performed by charging and discharging between 2.2 and 4.5 V with a current rate of 0.01 C at 30°C using a BT-2000 electrochemical station (Arbin).

5.3 Results and discussion

The X-ray diffraction (XRD) pattern of the as-prepared $LiMn_{0.7}Fe_{0.3}PO_4$ sample is shown in Figure 5.1a. All the diffraction peaks are clearly indexed as olivine-type $LiMnPO_4$, which belongs to the *Pnma* space group of orthorhombic crystal system. This is in agreement with reported values (JCPDS card no.74-0375) except for a slight shift in XRD peaks. Fe^{2+} and Mn^{2+} ions are located at the tetrahedral 4c sites in the olivine structure of $LiMn_xFe_{1-x}PO_4$. Since tetrahedrally coordinated Fe^{2+} has a smaller ionic radius (0.92 Å) than tetrahedrally coordinated Mn^{2+} (0.97 Å), a lattice contraction within the olivine structure (compared to LiMnPO4) occurs and the lattice parameters of LiMnPO4 decrease with the substitution of Mn^{2+} by Fe^{2+} [6,22]. This explains why the diffraction peaks have a slight shift towards higher angles as shown in Figure 5.1a. As a result, the as-prepared $LiFe_{0.7}Mn_{0.3}PO_4$ is a solid solution of $LiFePO_4$ and $LiMnPO_4$. There is no impurity phase detected within the scanning range used during this analysis. Figure 5.1b is an expanded view of Figure 5.1a in the range of 25 to 40^o to clearly demonstrate the displacement of the diffraction peaks with the incorporation of Fe into the crystal lattice. The average crystallite size of $LiFe_{0.7}Mn_{0.3}PO_4$, L, was calculated as 508 nm according to Scherrer formula [23,24]:

$$L = \frac{0.9\lambda_{K\alpha1}}{B_{(2\theta)}cos\theta_{max}}$$

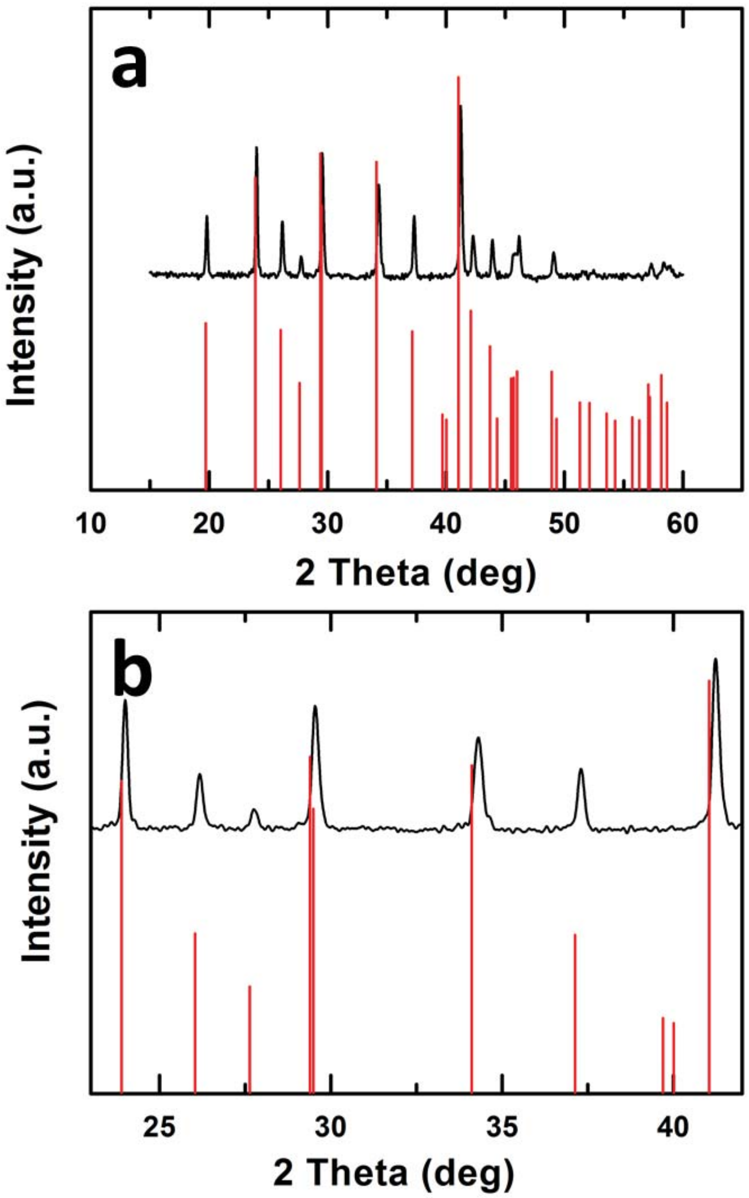

Figure 5.1: *(a) XRD patterns of* $LiFe_{0.3}Mn_{0.7}PO_4$ *synthesized by a hydrothermal method; (b) the expanded view of (a) to view the shift in peak position. The red peaks indicate the location of the diffracted peaks for a standard* $LiMnPO_4$ *material.*

As described in Experimental Section, the precursors (MnO and Fe_2O_3) used in our study have particle sizes in the micro length scale. To obtain a smaller particle size and more homogenous particle size distribution for the product of the hydrothermal reaction, a milling process for the precursors is required. The milling process increases the free energy of systems, and enhances the reactivity of the precursors [25]. This improves the ability of the hydrothermal method to produce a pure product. To demonstrate the necessity of the milling process before the hydrothermal treatment, the same precursors without milling were treated under identical conditions. Figure 5.2a shows the XRD pattern of the as-prepared product. The arrows in Figure 5.2a clearly indicate the impurity phases present within this sample. Obviously, the product is not as pure as that prepared with a pre-milling process (Figure 5.1). Thus, the milling process promotes the completeness of reaction during the hydrothermal treatment, leading to a pure $LiMn_{0.7}Fe_{0.3}PO_4$ product.

Ascorbic acid is often used as a reducing agent to prevent the oxidation of Fe^{2+} to Fe^{3+} during hydrothermal treatments for the synthesis of $LiFePO_4$ [26]. In this work, ascorbic acid is employed not only in the hydrothermal treatment but also in the pre-milling process. In the pre-milling process, ascorbic acid was used to prevent the aggregation of particles. The red color of the slurry after the whole pre-milling process implies that Fe^{3+} was not reduced during the milling process. Due to the high energy milling process, ascorbic acid is believed to be oxidized and loses its reduction effectiveness. Thus, an additional portion of ascorbic acid was added during the hydrothermal treatment to reduce Fe^{3+} to Fe^{2+}. To confirm this assumption, ascorbic acid was added only during the pre-milling process for one sample while all other conditions were kept identical. Figure 5.2b shows the resulting XRD pattern of the as-prepared product without additional ascorbic acid. As the arrows show in Figure 5.2b, the product is obviously not pure. The XRD results confirm that additional ascorbic acid is necessary to effectively reduce all Fe^{3+} in the sample to Fe^{2+} and thus obtain pure $LiMn_{0.7}Fe_{0.3}PO_4$. As described previously [27], ascorbic acid provides a strong reductive atmosphere during the hydrothermal process, such that the reduction of Fe^{3+} to Fe^{2+} is feasible. In summary, ascorbic acid has two functions: (1) to prevent aggregation of particle size during the pre-milling process and (2) to reduce Fe^{3+} to Fe^{2+} during the hydrothermal treatment. Any residual ascorbic acid was reduced to carbon during the elevated temperature treatment.

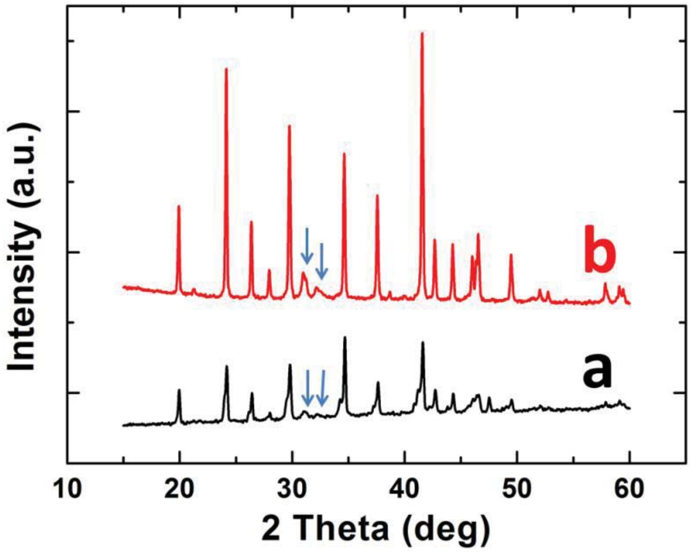

Figure 5.2: *(a) XRD patterns of* $LiFe_{0.3}Mn_{0.7}PO_4$ *synthesized by a hydrothermal treatment without a pre-milling process. (b) XRD patterns of* $LiFe_{0.3}Mn0.7PO_4$ *synthesized by a pre-milling process with ascorbic acid and a hydrothermal treatment without ascorbic acid (blue arrows are indicative of impurities within the sample).*

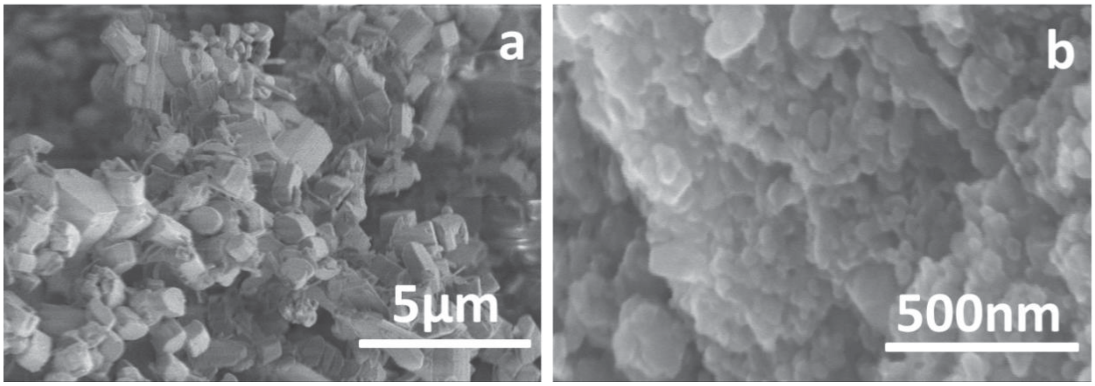

Figure 5.3: *(a) SEM images of* $LiFe_{0.3}Mn_{0.7}PO_4$ *synthesized by a hydrothermal method. (b) SEM images of* $LiFe_{0.3}Mn_{0.7}PO_4/C$ *produced from the product of (a) after nanomilling and carbon coating.*

A carbon coating process would be necessary to improve the conductivity of $LiMn_{0.7}Fe_{0.3}PO_4$ and obtain adequate electrochemical performance. Figure 5.3a provides the SEM images of the as-prepared $LiMn_{0.7}Fe_{0.3}PO_4$ samples. As shown in Figure 5.3a, the product has a uniform particle distribution of ~ 1-2 µm. In order to obtain good electrochemical performance, the as-prepared $LiMn_{0.7}Fe_{0.3}PO_4$ was milled and then coated with a film of carbon to improve its conductivity. As seen from Figure 5.3b, the particle size is reduced to ~50-100 nm and a thin film of carbon was coated on the particles (~7 wt%). Carbon coated $LiMn_{0.7}Fe_{0.3}PO_4$ powders were composed of individual particles with a small degree of particle agglomeration.

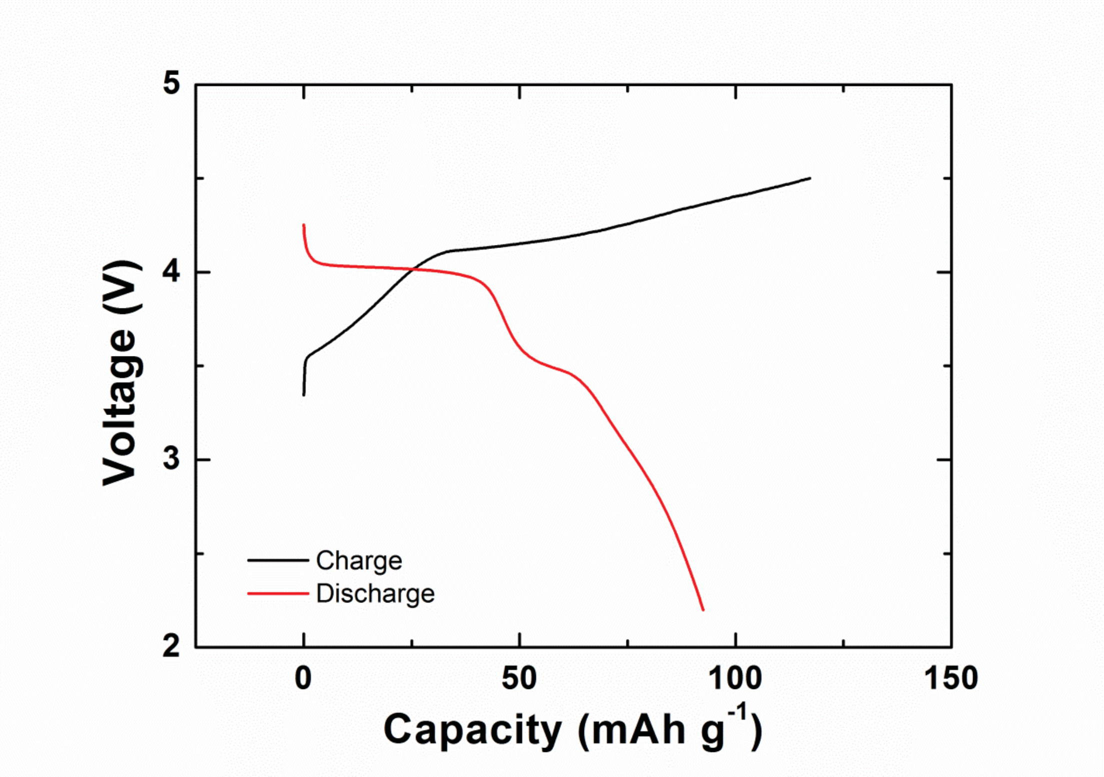

Figure 5.4: *Initial charge-discharge curves of carbon coated LiFe$_{0.3}$Mn$_{0.7}$PO$_4$. Cells are charged and discharged at a rate of C/100 at 30 °C.*

Figure 5.4 presents the initial charge-discharge curve of LiMn$_{0.7}$Fe$_{0.3}$PO$_4$/C. The cells at 30 °C were charged to 4.5 V in a constant current mode at a rate of C/100 (where 1 C = 170 mAh g^{-1}), followed by a discharge to 2.2 V at the same rate. The as-prepared LiMn$_{0.7}$Fe$_{0.3}$PO$_4$/C exhibits, as expected, two reversible charge-discharge plateaus. The one at ca. 4.1 V vs. Li/Li$^+$ corresponds to the Mn^{3+}/Mn^{2+} redox couple, while the other at ca. 3.5 V vs. Li/Li$^+$ corresponds to the Fe^{3+}/Fe^{2+} redox couple. The presence of both plateaus indicates that the charge/discharge reaction proceeds via first-order phase transitions. The redox process at the higher potential in LiFe$_x$Mn$_{1-x}$PO$_4$ compared to that in pure LiFePO$_4$, indicates that LiFe$_x$Mn$_{1-x}$PO$_4$ will have a higher energy density than pure $LiFePO_4$ [3]. The initial specific discharge capacity for $LiFe_{0.3}Mn_{0.7}PO_4/C$ is 100 mAh g^{-1}, and this leaves a lot of room for improvement in capacity for this material. Clearly, the electrochemical performance of olivine structures depends on several factors: crystallinity, morphology, particle size, homogeneity, specific surface area and electrode kinetics [28-30]. In our specific case, the product is pure and has a high purity as evidenced from XRD characterization. Secondly, it has a uniform particle distribution and small particle size as shown in the SEM images. Thirdly, chemical analysis indicated that the carbon content in $LiFe_{0.3}Mn_{0.7}PO_4/C$ is high (at ~ 7 wt%). Normally, a carbon content of 2-3 wt% is considered to be an optimum for elevated electrochemical performance of olivine cathode materials. Thus, the presence of a large amount of carbon is probably one of the causes leading to the poor performance of this electrode material. In addition, as reported in some papers, low-temperature routes could lead to Mn^{2+} disorder on the Li^+ sites in $LiMnPO_4$ (anti-site substitution), which blocks the one-dimensional (1D) diffusion path of Li ions, thus limiting electrochemical activity [5,31-33]. This may also be one of the reasons leading to the low performance of our material prepared at low temperature. Another probable cause is the low electronic conductivity of olivine-structure materials. A follow-up study on the structure and conductivity of $LiFe_{0.3}Mn_{0.7}PO_4/C$ is underway to understand the real causes and thus improve electrochemical performance of $LiFe_{0.3}Mn_{0.7}PO_4$.

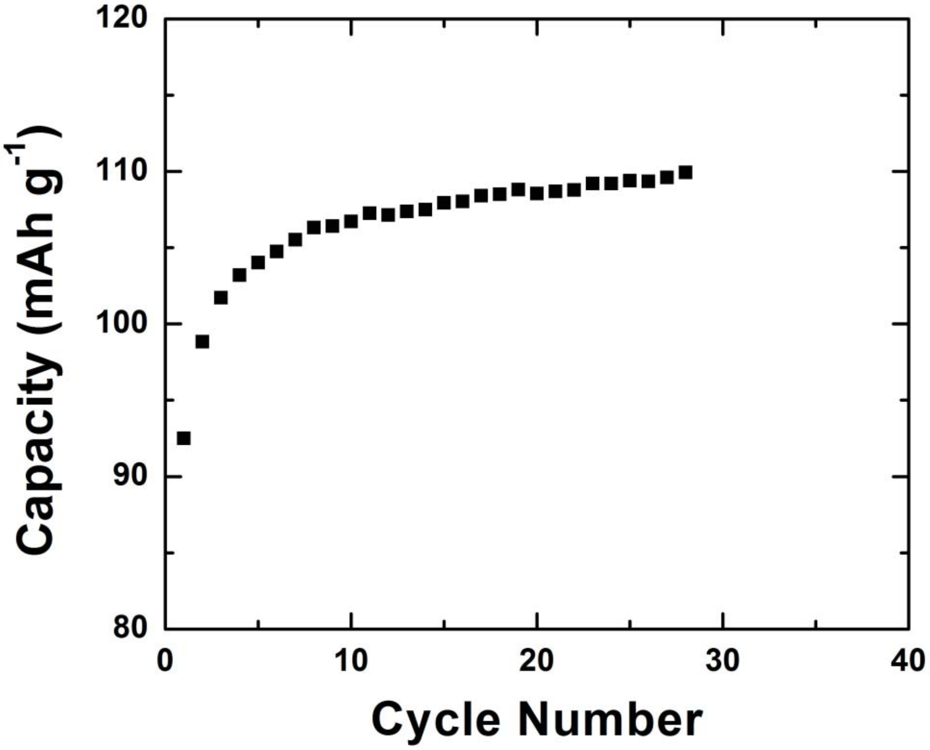

Figure 5.5: *Cyclic tests of carbon coated* $LiFe_{0.3}Mn_{0.7}PO_4$*. Cells are charged and discharged at a rate of C/100.*

Figure 5.5 provides the cycle life stability of the as-prepared $LiMn_{0.7}Fe_{0.3}PO_4/C$ at a rate of C/100 at 30^{o}C. Interestingly, the discharge capacity of $LiFe_{0.3}Mn_{0.7}PO_4/C$ is increasing gradually with cycle number although the initial discharge capacity is lower. This is likely due to the partial agglomeration of nano particles during the carbon coating process at 700 °C. Consequently, not all the surface of an individual particle is exposed to the electrolyte. Upon repeated charge-discharge cycling, the particles de-agglomerated, exposing more surfaces to the electrolyte providing improved performance. Another possible explanation for the capacity improvement upon cycling in olivine/carbon composites could be due to the improved penetration of the electrolyte into the interiors of the particle as a result of the formation of cracks in the amorphous carbon layer [34]. Recently, Ruhul et al. [35] and Doeff et al [36] have observed a similar behavior of capacity enhancement upon cycling $LiMnPO_4$ and $LiFe_{0.3}Mn_{0.7}PO_4$.

5.4 Conclusions

In this work, we developed a low cost method to prepare pure $LiMn_{0.7}Fe_{0.3}PO_4$ with low cost precursor Fe_2O_3 and MnO using a hydrothermal method. This is the first time a low temperature route has been used for a Fe substituted $LiMnPO_4$ material using a low cost Fe3+ precursor Fe_2O_3. A pre-milling process was required to provide small size and a homogenous precursor for the preparation of the pure $LiMn_{0.7}Fe_{0.3}PO_4$ material. Ascorbic acid was used to prevent particle aggregation in the pre-milling process. It also leads to a strong reductive atmosphere for the reduction of Fe^{3+} to Fe^{2+} during hydrothermal process. The lower discharge capacity for the as-prepared $LiFe_{0.3}Mn_{0.7}PO_4/C$ may be attributed to the presence of a large amount of carbon, lower conductivity and possible Mn^{2+} disorder. Further study is underway to determine the cause of low performance, such that $LiFe_{0.3}Mn_{0.7}PO_4$ with low cost synthesis and high performance is developed The advantage of our method to prepare $LiMn_{0.7}Fe_{0.3}PO_4$ is low cost and high purity. This report demonstrates that a reduction of Fe^{3+} to Fe^{2+} can be accomplished under low temperature condition, by choosing the proper precursors and reduction agent.

Acknowledgements

The authors thank NSERC and Clariant (Canada) Inc. (former Phostech Lithium Inc.) for funding this work under the auspices of the Industrial Research Chair program.

5.5 References

1. Tarascon, J. M.; Armand, M. *Nature* **2001**, 414, 359.
2. Yuan, L.-X.; Wang, Z.-H.; Zhang, W.-X.; Hu, X.-L.; Chen, J.-T.; Huang, Y.-H.; Goodenough, J. B. *Energy Environ. Sci.* **2011**, 4, 269.
3. Padhi, A. K.; Nanjundaswamy, K. S.; Goodenough, J. B. *J. Electrochem. Soc.* **1997**, 144, 1188.
4. Delacourt, C.; Laffont, L.; Bouchet, R.; Wurm, C.; Leriche, J.-B.; Morcrette, M.; Tarascon, J.-M.; Masquelier, C. *J. Electrochem. Soc.* **2005**, 152, A913.
5. Morgan, D.; Van der Ven, A.; Ceder, G. *Electrochem. Solid-State Lett.* **2004**, 7, A30.
6. Martha, S. K.; Grinblat, J.; Haik, O.; Zinigrad, E.; Drezen, T.; Miners, J. H.; Exnar, I.; Kay, A.; Markovsky, B.; Aurbach, D. *Angew. Chem. Int. Ed.* **2009**, 48, 8559.
7. Lee, K. T.; Lee, K. S. *J. Power Sources* **2009**, 189, 435.
8. Wang, Z.-H.; Yuan, L.-X.; Zhang, W.-X.; Huang, Y.-H. *J. Alloys Compd.* **2012**, 532, 25.
9. Chang, X. Y.; Wang, Z. X.; Li, X. H.; Zhang, L.; Guo, H. J.; Peng, W. J. *Mater. Res. Bull.* **2005**, 40, 1513.
10. Yamada, A.; Chung, S. C.; Hinokuma , K. *J. Electrochem. Soc.* **2001**, 148, A224.
11. Yamada, A.; Kudo, Y.; Liu, K.-Y. *J. Electrochem. Soc.* **2001**, 148, A747.

12. Li, G.; Kudo, Y.; Liu, K.-Y.; Azuma, H.; Tohda, M. *J. Electrochem. Soc.* **2002**, 149, A1414.

13. Li, G.; Azuma, H.; Tohda , M. *J. Electrochem. Soc.* **2002**, 149, A743.

14. Zhang, B.; Wang, X.; Liu, Z.; Li, H.; Huang, X. *J. Electrochem. Soc.* **2010**, 157, A285.

15. Baek, D.-H.; Kim, J.-K.; Shin, Y.-J.; Chauhan, G. S.; Ahn, J.-H.; Kim, K.-W. *J. Power Sources* **2009**, 189, 59.

16. Wang, D.; Ouyang, C.; Drézen, T.; Exnar, I.; Kay, A.; Kwon, N.-H.; Gouerec, P.; Miners, J. H.; Wang, M.; Grätzel, M. *J. Electrochem. Soc.* **2010**, 157, A225.

17. Chen, J. J.; Whittingham, M. S. *Electrochem. Commun.* **2006**, 8, 855.

18. Yang, S.; Zavalij, P. Y.; Stanley Whittingham, M. *Electrochem. Commun.* **2001**, 3, 505.

19. Ellis, B.; Kan, W. H.; Makahnouk, W. R. M.; Nazar, L. F. *J. Mater. Chem.* **2007**, 17, 3248.

20. Qian, J.; Zhou, M.; Cao, Y.; Ai, X.; Yang, H. *J. Phys. Chem. C* **2010**, 114, 3477.

21. Lu, Z.; Chen, H.; Robert, R.; Zhu, B. Y. X.; Deng, J.; Wu, L.; Chung, C. Y.; Grey, C. P. *Chem. Mater.* **2011**, 23, 2848.

22. Wang, Y.; Zhang, D.; Yu, X.; Cai, R.; Shao, Z.; Liao, X.-Z.; Ma, Z.-F. *J. Alloys Compd.* **2010**, 492, 675.

23. Zhang, Z.; Ge, J.; Ma, L.; Liao, J.; Lu, T.; Xing, W. *Fuel Cells* **2009**, 9, 114.

24. Cheng, L.; Zhang, Z.; Niu, W.; Xu, G.; Zhu, L. *J. Power Sources* **2008**, 182,

91.

25. Liu, X.-h.; Zhao, Z.-w. *Powder Technol.* **2010**, 197, 309.
26. Chen, J.; Vacchio, M. J.; Wang, S.; Chernova, N.; Zavalij, P. Y.; Whittingham, M. S. *Solid State Ionics* **2008**, 178, 1676.
27. Cheng, L.; Liang, G.; Khakani, S. E.; MacNeil, D. D. *J. Power Sources* **2012**, submitted.
28. Kim, J.-K.; Chauhan, G. S.; Ahn, J.-H.; Ahn, H.-J. *J. Power Sources* **2009**, 189, 391.
29. Doan, T. N. L.; Taniguchi, I. *J. Power Sources* **2011**, 196, 1399.
30. Gaberscek, M.; Dominko, R.; Jamnik, J. *Electrochem. Commun.* **2007**, 9, 2778.
31. Fang, H.; Pan, Z.; Li, L.; Yang, Y.; Yan, G.; Li, G.; Wei, S. *Electrochem. Commun.* **2008**, 10, 1071.
32. Islam, M. S.; Driscoll, D. J.; Fisher, C. A. J.; Slater, P. R. *Chem. Mater.* **2005**, 17, 5085.
33. Amin, R.; Maier, J.; Balaya, P.; Chen, D. P.; Lin, C. T. *Solid State Ion.* **2008**, 179, 1683.
34. Dominko, R.; Bele, M.; Gaberscek, M.; Remskar, M.; Hanzel, D.; Goupil, J. M.; Pejovnik, S.; Jamnik, J. *J. Power Sources* **2006**, 153, 274.
35. Amin, R.; Liang, G.; Gauthier, M.; MacNeil, D. *J. Power Sources* **2012**, submitted.
36. Doeff, M. M.; Chen, J.; Conry, T. E.; Wang, R.; Wilcox, J.; Aumentado, A. *J. Mater. Res.* **2010**, 25, 1460.

Chapter 6 Comparison of a Microwave Assisted and a Conventional Hydrothermal Synthesis of α-Fe_2O_3 Nanoparticles for Use as Anode Materials for Lithium Ion Batteries

Lifeng Cheng[a], Guoxian Liang[b], Soumia El Khakani[a], Dean D. MacNeil[a*]

[a] Département de Chimie, Université de Montréal, Montréal, Québec H3T 1J4, Canada

[b] Clariant (Canada) Inc., 1475 Rue Marie-Victorin, St-Bruno, Québec J3V 6B7, Canada

Chapter 6 consists of an article submitted to the International Journal of Electrochemistry. The article was prepared by the author under the supervision of Dr. MacNeil and Dr. Liang. Soumia EL Khakani, Ph.D student in Dr. MacNeil's lab aided with the electrochemical tests.

Abstract

In this work, a comparison between a microwave assisted (MAH) and conventional hydrothermal (CH) synthesis of α-Fe_2O_3 nanoparticles for use as anode materials for lithium ion batteries will be shown. MAH-α-Fe_2O_3 nanoparticles due to their smaller particle size deliver higher initial capacity than CH-α-Fe_2O_3 nanoparticles.

However, fine nanoparticles induce secondary reactions, which may cause large irreversible capacity loss (i.e., low coulombic efficiency) and consumption of active material yielding poor cycle life and capacity retention. However, CH-α-Fe_2O_3 *shows good cycling performance and retains over 450 mAh* g^{-1} *for 15 cycles. The moderate particle size and good crystallinity of CH-α-*Fe_2O_3 *favors the retention of the crystalline structure during Li insertion/extraction.*

6.1 Introduction

Lithium ion batteries (LIBs) are currently the dominant power source for portable electronic devices. The ever-growing need for high capacity and/or high power, especially for emerging large-scale applications (e.g., electric cars), has prompted numerous research efforts towards developing new high-performance electrode materials for next-generation LIBs [1-4].

Hematite (α-Fe_2O_3), as one of the transition metal oxides [4-7], can in principle deliver as high as three times the capacity of currently used lithium-ion anode material (graphite, < 372 mAh g^{-1}). It has attracted great interests due to attractive features such as low cost, good stability, nontoxicity, and environmentally friendliness. Recently, diverse α-Fe_2O_3 nanostructures, including nanoparticles [8], nanocubes [9], nanorods [10], and nanotubes [11], have been successfully synthesized, which promotes the increased use of iron oxide as a possible anode material. It was found that the particle size and morphology of the various α-Fe_2O_3

nanostructures has a remarkable effect on their electrochemical performance toward lithium storage.

A hydrothermal synthetic method has been a well-established approach for preparing controlled inorganic nanocrystals due to its simplicity, allowing the control of grain size, morphology and crystallinity through simple changes within the experimental procedure [12-14]. A microwave–assisted hydrothermal method employing microwave irradiation as heat source has been considered as a novel method offering shorten reaction times with a high degree of control of particle size and morphology [15-17].

In this work, we have explored two methods, conventional hydrothermal (CH) and microwave-assisted hydrothermal (MAH) methods, to prepare α-Fe_2O_3 while comparing their electrochemical performance as anode materials for LIBs. Both as-prepared α-Fe_2O_3 nanostructures show different electrochemical behaviors toward lithium storage. It is found that the conventional hydrothermal method is more suitable to prepare α-Fe_2O_3 nanostructure which shows better lithium storage properties than that prepared by the microwave-assisted hydrothermal method.

6.2 Experimental

6.2.1 Preparation of hematite nanostructures

6.2.1.1 Conventional hydrothermal method (referred as CH-α-Fe_2O_3)

α-Fe_2O_3 nanostructures were prepared based on that reported in [18]. In a typical procedure, 4 mmol of $FeCl_3$ was dissolved into 15 mL of distilled water to form a transparent solution. To control its size and morphology, 12 mmol of NaCl was added to the above solution. After stirring for 30 min, the solution was transferred and sealed into a 25 mL Teflon-lined autoclave. The autoclave was then heated at 180°C for 24 h, following cooling to room temperature naturally. The as-prepared precipitate was collected by centrifuging and repeatedly washed with distilled water and ethanol. The sample was then dried in vacuum for further characterizations and electrochemical tests.

6.2.1.2 Microwave-assisted hydrothermal method (referred as MAH-α-Fe_2O_3)

The solution prepared in 2.1.1 was sealed in a double-walled Teflon digestion vessel and treated at 180 °C for 45 min using a microwave digestion system (MARS-5, CEM Corp). After being cooled to room temperature, the product was collected as described in 6.2.1.1.

6.2.2 Physicochemical characterizations

X-ray diffraction (XRD) was performed using a Bruker D8 X-ray Advance diffractometer equipped with a Cu Kα (*k* = 1.5405 Å) radiation source. Phase purity was checked by comparison with the standard data (JCPDS card). The particle size and morphology of samples were examined by a Scanning Electron Microscope (Hitachi S-4300 microscope).

6.2.3 Electrochemical measurements

Electrochemical evaluations were performed by combining 80 wt% α-Fe_2O_3 powder, 10 wt% of conductive carbon (Super-P Li, Timcal) and 10 wt% polyvinylidene difluoride (PVDF, 5% in N-methylpyrroldinone (NMP) with an excess of NMP to form slurry. The slurry was then deposited on a Cu foil. After drying at 90 °C overnight, electrode disks were punched and weighed for the cell assembly in standard 2032 coin-cell hardware (Hohsen) using a lithium metal foil as both counter and reference electrodes and a Celgard 2200 separator. Cells were assembled in an argon-filled glove box using 1 M $LiPF_6$ in ethylene carbonate (EC) / diethyl carbonate (DEC) (2:1 by volume) as an electrolyte (UBE). Battery performance evaluations were performed by charging and discharging between 3.0 and 0.1 V with a current rate of C/10 at 30°C using a BT-2000 electrochemical station (Arbin).

6.3 Results and Discussion

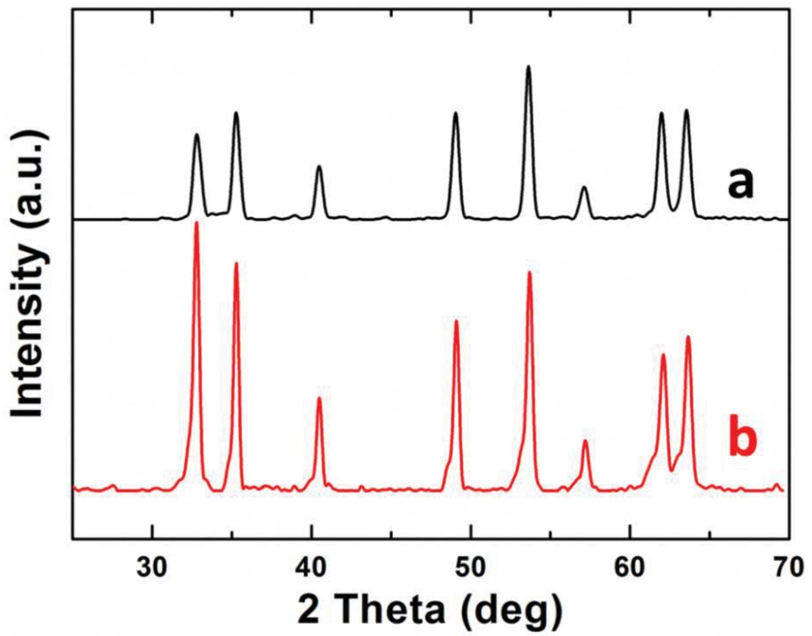

Figure 6.1: *XRD patterns of α-Fe_2O_3 nanoparticles synthesized by microwave assisted hydrothermal (a: MAH-α-Fe_2O_3) and conventional hydrothermal methods (b: CH-α-Fe_2O_3).*

Figure 6.1 shows the XRD patterns of MAH-α-Fe_2O_3 and CH-α-Fe_2O_3. All diffraction peaks are in good agreement with rhomb-centered hexagonal α-Fe_2O_3 [JCPDS Card # 03-0664, space group: *R*3j*c*(167)]. No other peaks are observed, indicating the high purity of α-Fe_2O_3 prepared by both methods [18]. MAH-α-Fe_2O_3 (Figure 6.1a) has larger half peak width than CH-α-Fe_2O_3 (Figure 6.1b), indicating a smaller particle size and lower crystallinity than CH-α-Fe_2O_3.

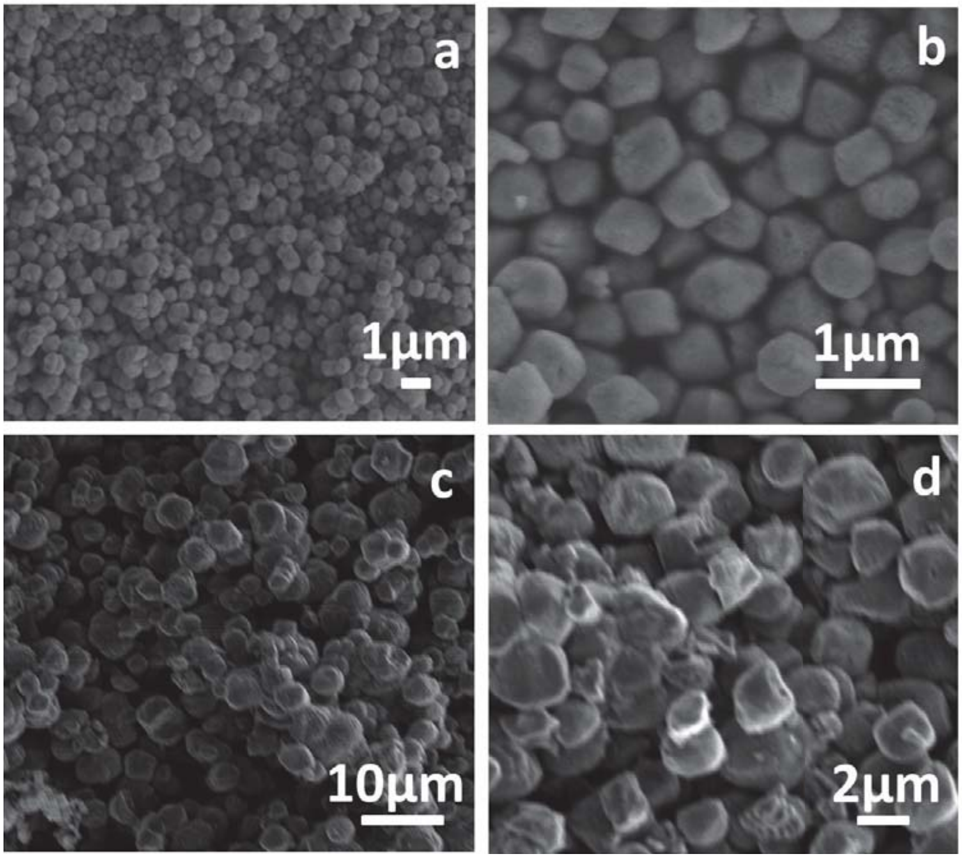

Figure 6.2: *SEM images of MAH-α-Fe_2O_3 nanoparticles (a, b) and CH-α-Fe_2O_3 nanoparticles (c, d).*

SEM is used to observe the size and morphology of MAH-α-Fe_2O_3 and CH-α-Fe_2O_3. As shown in Figure 6.2, both samples show sphere-like α-Fe_2O_3 morphology with a uniform particle size distribution. As reported previously, the inorganic salt Cl^- functions as a size and morphology directing agent [18]. As expected, MAH-α-Fe_2O_3 synthesized by the microwave method has a smaller particle size (500 nm, Figure 6.2a and 6.2b) than CH-α-Fe_2O_3 (2μm, Figure 6.2c and 6.2d) prepared by the conventional hydrothermal method. It is well known that the microwave heating, due to high penetration depth of microwaves, is very fast and uniform, and thus can minimize thermal gradients and the time required for particle diffusion within the solution. This favors the formation of precipitated products in a relatively short time. Moreover, the sintering of particles is unfavorable, thus small particles sizes can be achieved [19-21]. However, a normal hydrothermal method cannot avoid long sintering times, which induces the product with larger particle sizes.

To compare the electrochemical properties of the as-prepared α-Fe_2O_3 nanoparticles as anode materials for LIBs, we carried out a preliminary investigation into their electrochemical performance with respect to Li insertion/extraction. Figure 6.3 shows the initial discharge/charge voltage profiles for the MAH-α-Fe_2O_3 (Figure 6.3a) and CH-α-Fe_2O_3 (Figure 6.3b) at a rate of *C*/10 (100.7 mA g^{-1}) in the voltage window of 0.1-3.0 V (vs. Li^+/Li). For both types of α-Fe_2O_3 nanoparticles, there exist two plateaus: a poorly defined plateau (1.6-0.8 V, inset) followed by a well-defined one at 0.8 V. Similar electrochemical behaviors for Fe_2O_3 have been reported in the past [22,23]. The electrochemical reaction mechanism of Li with α-Fe_2O_3 in LIBs can be described by Equations (1) and (2).

$$Fe_2O_3 + 2Li^+ + 2e^- \rightarrow Li_2(Fe_2O_3) \qquad (1)$$

$$Li_2(Fe_2O_3) + 4Li^+ + 4e^- \rightarrow 2Fe + 3Li_2O \qquad (2)$$

Therefore, the first plateau (1.6-0.8 V) can be ascribed to the formation of cubic $Li_2Fe_2O_3$, while the second one (0.8 V) can be attributed to the reduction of Fe^{3+} to Fe^0 and the formation of amorphous Li_2O.

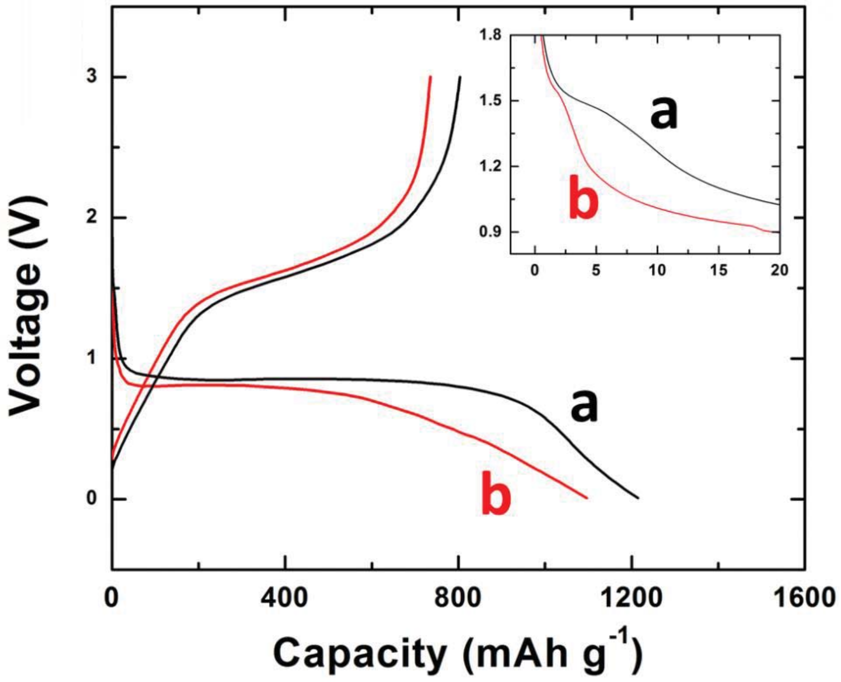

Figure 6.3: Initial discharge/charge curves of MAH-α-Fe_2O_3 nanoparticles (a) and CH-α-Fe_2O_3 nanoparticles (b). The insert is the enlarged view of the discharge/charge curves in the capacity range of 0-50 mAh g^{-1}.

On the basis of a complete reduction of Fe^{3+} to Fe^0, a maximum capacity uptake of 1007 mA h g^{-1} (e.g. 6 Li per α-Fe_2O_3) is expected for α-Fe_2O_3. However, as revealed in Figure 6.3, the initial discharge capacity of CH-α-Fe_2O_3 and MAH-α-Fe_2O_3 is

1100 and 1250 mA hg-1, respectively, both of which are larger than the theoretical capacity (1007 mA h g^{-1}). The difference of the lithium storage ability between both α-Fe_2O_3 nanostructures is ascribed to the different capacity in the region of 0.01-0.8 V as shown in the Figure 6.3. The phenomenon that the initial discharge capacity exceeds the theoretical capacity has been reported previously for transition metal oxides [24,25]. Generally, the exceeded capacity is due to the electrolyte being reduced at low voltage (generally below 0.8 V vs. Li^+/Li) to form a solid electrolyte interphase (SEI) layer and possible interfacial lithium storage [26,27]. This is related to the particle size and surface area of samples [18]. Therefore, MAH-α-Fe_2O_3 with its smaller particle size and higher surface area has higher capacity than CH-α-Fe_2O_3.

Figure 6.4 shows the cycling performance of both α-Fe_2O_3 nanoparticles. As seen from Figure 6.4a, the specific capacity of MAH-α-Fe_2O_3 decreases quickly to 325 mAh g^{-1} after 15 cycles although it delivers a higher initial charge capacity. After 15 cycles, the specific capacity of CH-α-Fe_2O_3 nanoparticles is still 425 mAh g^{-1} (Figure 6.4b), which is much higher than the theoretical specific capacity of currently used graphite (LiC_6, 372 mA h g^{-1}).

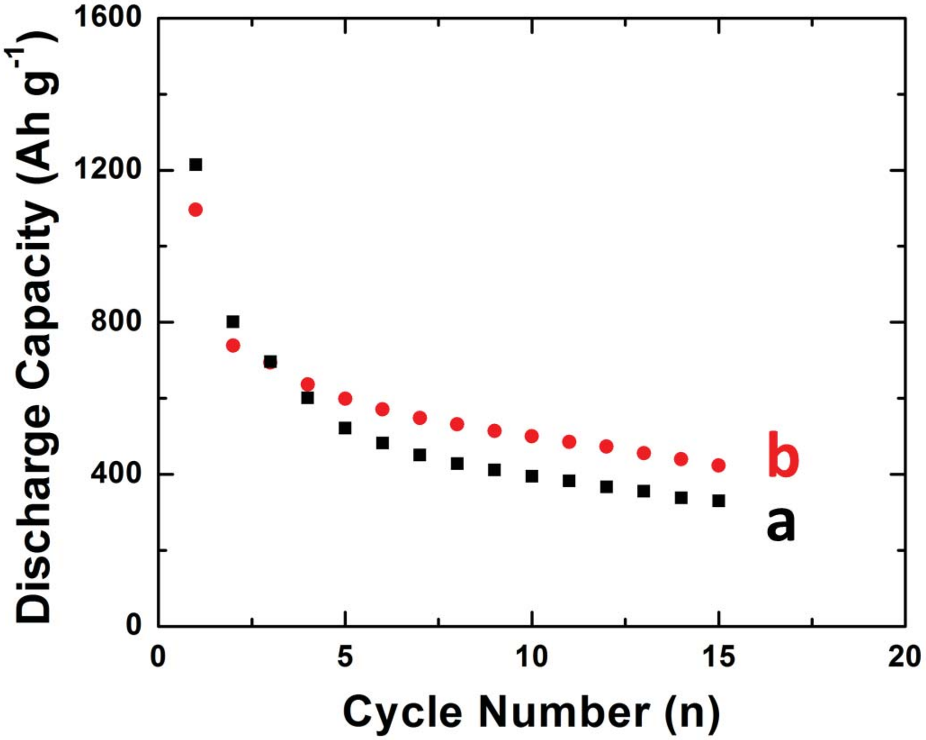

Figure 6.4: *Cycling performance of MAH-α-Fe_2O_3 nanoparticles (a) and CH-α-Fe_2O_3 nanoparticles (b).*

To further illustrate the difference in cycling performances between both Fe_2O_3, the discharge/charge voltage profiles and coulombic efficiency are displayed in Figure 6.5. Figure 6.5a and 6.5b show the discharge/charge voltage profiles for both α-Fe_2O_3 nanostructures. For the CH-α-Fe_2O_3 (Figure 6.5b), it can be observed that the plateau at 0.8 V of the first discharge curve and the slope at 1.6 V on the first charge curve are still present in all subsequent discharge/charge curves. In the case of MAH-α-Fe_2O_3 nanospheres (Figure 6.5a), the plateau at 0.8 V of the first discharge curve and the slope at 1.6 V of the first charge curve are still present in the all subsequent discharge/charge curves. However, a new feature develops at 2.8 V after the third charge cycle, which means that secondary reactions or crystallinity structural damage occurs during the cycling process. It is known that the crystalline texture and surface atomic arrangement of synthesized nanostructures are the primary factors for the size and morphology-dependent electrochemical properties. Though nanometer-sized particles have multifold merits, for example, preferable accommodation to the strain of Li+ insertion/extraction in the processes of discharge and charge to maintain the integrity of electrode materials [27,28], the high surface areas raise the risk of secondary reactions, including formation and (or) decomposition of SEI layers. The secondary reactions may cause a large irreversible capacity loss (i.e., low Coulombic efficiency), consumption of active materials and poor cycle life. As shown in Figure 6.5c, both α-Fe_2O_3 nanostructures exhibit the same low coulombic efficiency of about 63% for the first cycle. After the first cycle, the coulombic efficiency of H-α-Fe_2O_3 is above 95% and thereafter stabilizes at about 98%. In contrast, MAH-α-Fe_2O_3 shows a quite different behavior in which the coulombic efficiency is not stable and lower than that of H-α-Fe_2O_3.

The higher initial capacity of MAH-Fe_2O_3 may be ascribed to its smaller particle size and thus larger specific surface area than CH-Fe_2O_3. The difference in cycling performance and coulombic efficiency should result from the different crystallinity of both α-Fe_2O_3 nanostructures. The MAH-α-Fe_2O_3 with lower crystallinity, due to its shorter sintering time, leads to the lower capacity retention and the destruction of the structure during repetitive Li insertion/extraction process.

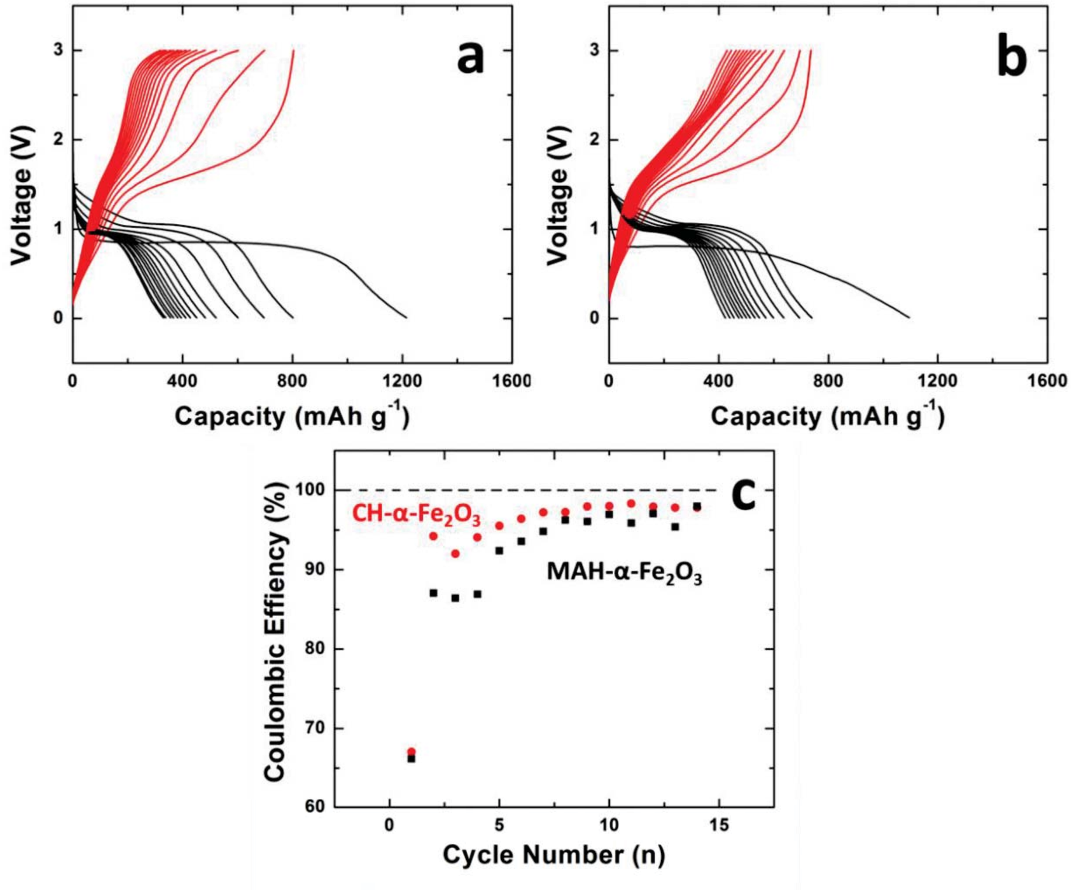

Figure 6.5: *Galvanostatic discharge/charge voltage profiles for MAH-α-Fe_2O_3 (a) and CH-α-Fe_2O_3 (b) cycled at a rate of C/10. (c) Corresponding coulombic efficiency profiles of both α-Fe_2O_3 nanostructures.*

In summary, microwave irradiation offers an inexpensive and convenient method of heating, resulting in products with smaller particle size in a shorter reaction time. The smaller particle size leads to higher initial capacity, however, it raises the risk of secondary reactions, causing a large irreversible capacity loss (i.e. low Coulombic efficiency), the consumption of active materials and a poor cycle life. Shorter sintering times lead to lower crystallinity, accommodating the change in structure during repetitive Li insertion/extraction processes. A conventional hydrothermal method has been shown to be a promising method to prepare fine, uniform and well-crystallized products. The long sintering times increases the particle size and contributes to good crystallinity. This favors improved cycling performance, making CH-α-Fe_2O_3 a promising anode material for lithium-ion batteries.

6.4 Conclusions

In this work，two α-Fe_2O_3 nanoparticles with different size and morphology have been prepared using sodium chloride as a structure-directing agent by microwave-assisted hydrothermal and conventional hydrothermal methods, respectively. Both α-Fe_2O_3 nanoparticles were used as anode materials for lithium ion batteries. MAH-α-Fe_2O_3 nanoparticles due to their smaller particle size deliver a higher initial capacity than CH-α-Fe_2O_3 nanoparticles. However, the fine nanoparticles in MAH Fe_2O_3 also increased secondary reactions, causing a large irreversible capacity loss and consumption of active materials leading to poor cycle life. The specific capacity of MAH-α-Fe_2O_3 decreases rapidly to 352 mAh g^{-1} after 15 cycles. However, CH-α-Fe_2O_3 shows good cycling performance of 452 mAh g^{-1} after 15 cycles that is higher than the theoretical specific capacity of currently used graphite (LiC_6, 372 mA h g^{-1}) materials. This is due to the good crystallinity and moderate particle size of CH-α-

Fe_2O_3 that favors the retention of its structure during repetitive Li insertion/extraction. By comparison, the conventional hydrothermal method was found to be more suitable than a microwave-assisted method to prepare α-Fe_2O_3 nanostructure with high cycling performance for lithium-ion batteries.

Acknowledgements

The authors thank NSERC and Clariant (Canada) Inc. (former Phostech Lithium Inc.) for funding this work under the auspices of the Industrial Research Chair program.

6.5 References

1. Lou, X. W.; Deng, D.; Lee, J. Y.; Feng, J.; Archer, L. A. *Adv. Mater.* **2008**, 20, 258.
2. Arico, A. S.; Bruce, P.; Scrosati, B.; Tarascon, J.-M.; van Schalkwijk, W. *Nat. Mat.* **2005**, 4, 366.
3. Tarascon, J. M.; Armand, M. *Nature* **2001**, 414, 359.
4. Poizot, P.; Laruelle, S.; Grugeon, S.; Dupont, L.; Tarascon, J. M. *Nature* **2000**, 407, 496.
5. Reddy, M. V.; Yu, T.; Sow, C. H.; Shen, Z. X.; Lim, C. T.; Rao, G. V. S.; Chowdari, B. V. R. *Adv. Funct. Mater.* **2007**, 17, 2792.
6. He, T.; Chen, D.; Jiao, X.; Wang, Y.; Duan, Y. *Chem. Mater.* **2005**, 17, 4023.
7. Park, J. C.; Kim, J.; Kwon, H.; Song, H. *Adv. Mater.* **2009**, 21, 803.
8. Jin, J.; Ohkoshi, S.; Hashimoto, K. *Adv. Mater.* **2004**, 16, 48.
9. Pu, Z.; Cao, M.; Yang, J.; Huang, K.; Hu, C. *Nanotech.* **2006**, 17, 799.
10. Woo, K.; Lee, H. J.; Ahn, J. P.; Park, Y. S. *Adv. Mater.* **2003**, 15, 1761.
11. Chen, J.; Xu, L.; Li, W.; Gou, X. *Adv. Mater.* **2005**, 17, 582.
12. Wang, G. X.; Shen, X. P.; Yao, J. N.; Wexler, D.; Ahn, J. *Electrochem. Commun.* **2009**, 11, 546.
13. Zhou, F.; Zhao, X. M.; Yuan, C. G.; Xu, H. *Chem. Lett.* **2006**, 35, 1410.

14. Ni, S.; Wang, X.; Zhou, G.; Yang, F.; Wang, J.; Wang, Q.; He, D. *Mater. Lett.* **2009**, 63, 2701.
15. Pires, F. I.; Joanni, E.; Savu, R.; Zaghete, M. A.; Longo, E.; Varela, J. A. *Mater. Lett.* **2008**, 62, 239.
16. Lebedev, V.; Gavrilov, A.; Shaporev, A.; Ivanov, V.; Churagulov, B.; Tret'yakov, Y. *Dokl. Chem.* **2012**, 444, 117.
17. Hu, X. L.; Yu, J. C. *Adv. Funct. Mater.* **2008**, 18, 880.
18. Wu, X. L.; Guo, Y. G.; Wan, L. J.; Hu, C. W. *J. Phys. Chem. C* **2008**, 112, 16824.
19. Parada, C.; Morán, E. *Chem. Mater.* **2006**, 18, 2719.
20. Whitfield, P. S.; Davidson, I. J. *J. Electrochem. Soc.* **2000**, 147, 4476.
21. Nuchter, M.; Ondruschka, B.; Bonrath, W.; Gum, A. *Green Chem.* **2004**, 6, 128.
22. Zhou, G.; Wang, D.-W.; Hou, P.-X.; Li, W.; Li, N.; Liu, C.; Li, F.; Cheng, H.-M. *J. Mater. Chem.* **2012**, 22, 17942.
23. Liu, J.; Li, Y.; Fan, H.; Zhu, Z.; Jiang, J.; Ding, R.; Hu, Y.; Huang, X. *Chem. Mater.* **2009**, 22, 212.
24. Morimoto, H.; Tobishima, S.-i.; Iizuka, Y. *J. Power Sources* **2005**, 146, 315.
25. Hang, B. T.; Doi, T.; Okada, S.; Yamaki, J.-i. *J. Power Sources* **2007**, 174, 493.
26. Balaya, P.; Li, H.; Kienle, L.; Maier, J. *Adv. Funct. Mater.* **2003**, 13, 621.
27. Maier, J. *Nat. Mat.* **2005**, 4, 805.
28. Hu, Y. S.; Kienle, L.; Guo, Y. G.; Maier, J. *Adv. Mater.* **2006**, 18, 1421.

Chapter 7 Conclusion and Perspectives

7.1 Conclusion

This thesis concentrated on finding new low cost synthetic methods to electrode materials for lithium-ion batteries.

In chapter 3, $LiFePO_4/C$ composite materials were synthesized with nano Fe_2O_3 as a precursor using a modified hydrothermal method. The two-step method combined the advantages of both hydrothermal and solid state synthetic methods. In the first step, a $LiFePO_4(OH)$ precursor with small particle size and uniform size distribution was prepared by a hydrothermal method. The heat treatment in the second step lead to the simultaneous realization of carbon coating and $LiFePO_4(OH)$ reduction, producing $LiFePO_4/C$ with high purity and crystallinity. The electrode from this material provided high specific discharge capacity and cycle stability compared to samples synthesized with the same precursors using only a solid state method. The modified hydrothermal method combined with less expensive Fe_2O_3 precursors can greatly reduce synthetic costs of $LiFePO_4$. It is thus very promising for the large scale synthesis of $LiFePO_4/C$ cathode materials for lithium ion batteries.

In chapter 4, $LiFePO_4$ with good crystallinity and high purity was synthesized with nano Fe_2O_3 by a hydrothermal method in one step. As a preliminary study, commercial nano Fe_2O_3 was explored as a possible Fe^{3+} precursor, while ascorbic acid and H_3PO_3 were used as co-reducing agents. The main reducing agent is ascorbic acid, which is pyrolyzed to produce CO or H_2 in the atmosphere that reduces most of Fe^{3+} to Fe^{2+}. The H_3PO_3 was used as a co-reducing agent and it may change the pH value of reaction environment. Although the particle size of as-prepared $LiFePO_4$ is large (leading to lower electrochemical performance), the work is promising since, for the first time, pure $LiFePO_4$ can be prepared with nano Fe_2O_3 at low temperature by choosing proper precursors and reducing agents.

In chapter 5, a low cost method to prepare pure $LiMn_{0.7}Fe_{0.3}PO_4$ with low cost precursor Fe_2O_3 using a hydrothermal method was developed. This is the first time a low temperature route has been used for a Mn substituted $LiFePO_4$ material. A pre-milling process was required to reduce particle size and to provide a homogenous precursor distribution for the preparation of the pure $LiMn_{0.7}Fe_{0.3}PO_4$ material. Ascorbic acid was used to prevent particle aggregation during the pre-milling process. It also provided a strong reductive atmosphere for the reduction of Fe^{3+} to Fe^{2+} during the subsequent hydrothermal process. The lower discharge capacity for the as-prepared $LiFe_{0.3}Mn_{0.7}PO_4/C$ may be attributed to the presence of a large amount of carbon, lower conductivity and possible Mn^{2+} disorder. Further study is underway to determine the cause of low performance, such that $LiFe_{0.3}Mn_{0.7}PO_4$ with low cost synthesis and high performance is developed and can be commercialized.

For the study on the low cost anode materials, a comparison between microwave assisted (MAH) and conventional hydrothermal (CH) syntheses of α-Fe_2O_3 nanoparticles was performed.

In chapter 6, two α-Fe_2O_3 nanoparticles with different particle size and morphology were prepared using sodium chloride as a structure-directing agent by microwave-assisted hydrothermal (MAH) and conventional hydrothermal methods (CH). Both α-Fe_2O_3 nanoparticles were used as anode materials for lithium ion batteries. MAH-α-Fe_2O_3 nanoparticles due to their smaller particle size delivered a higher initial capacity than CH-α-Fe_2O_3 nanoparticles. However, the fine nanoparticles in MAH Fe_2O_3 also increased the rate of parasitic secondary reactions, causing a large irreversible capacity loss and consumption of active materials leading to poor cycle life. The specific capacity of MAH-α-Fe_2O_3 decreases rapidly to 352 mAh g^{-1} after 15 cycles. However, CH-α-Fe_2O_3 shows good cycling performance of 452 mAh g^{-1} after 15 cycles that is higher than the theoretical specific capacity of currently used graphite (LiC_6, 372 mA h g^{-1}) materials. This is due to the good crystallinity and moderate particle size of CH-α-Fe_2O_3 that favors the retention of its structure during repetitive Li insertion/extraction.

7.2 Perspectives

There is still some valuable work to be pursued based on the results of this thesis. For example, the product from chapter 4 requires a smaller particle size such that electrochemical tests can be improved for commercial lithium-ion batteries. Thus, further study should concentrate on reducing particle size by choosing improved precursors, reducing agents or by adding proper surfactants.

In addition, as mentioned in chapter 5, the initial specific discharge capacity for $LiFe_{0.3}Mn_{0.7}PO_4/C$ is only 100 mAh g^{-1}. One probable cause for the low performance is the low electronic conductivity of olivine-structure materials. Thus, a follow-up study on the relationship between the structure and conductivity of $LiFe_{0.3}Mn_{0.7}PO_4/C$ is needed to do to understand the real causes of low performance such that an improved $LiFe_{0.3}Mn_{0.7}PO_4$ can be developed since the higher operating potential over $LiFePO_4$ leads to cells with more energy.